Univerzita Karlova v Praze
Matematicko-Fyzikální fakulta

DIZERTAČNÍ PRÁCE

Richard Polifka

Analýza dvoujetových případů v difrakčních *ep* interakcích s detekovaným protonem na experimentu H1
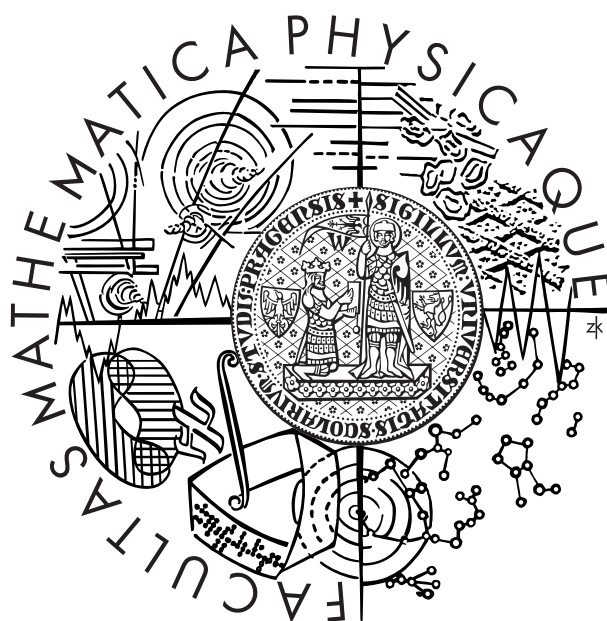
Ústav částicové a jaderné fyziky

Vedoucí dizertační práce: RNDr. Alice Valkárová, DrSc.
Studijní program: Fyzika, Jaderná a Částicová Fyzika

Charles University in Prague
Faculty of Mathematics and Physics

THESIS

Richard Polifka

Analysis of dijet events in diffractive *ep* interactions with tagged leading proton at the H1 experiment

Institute of Particle and Nuclear Physics

Supervisor: RNDr. Alice Valkárová, DrSc.
Study program: Physics, Nuclear and Particle Physics

Acknowledgements

Prohlašuji, že jsem svoji dizertační práci napsal samostatně a výhradně s použitím citovaných pramenů. Souhlasím se zapůjčováním práce.

V Praze dne   Richard Polifka

Abstrakt

Název práce: Analýza dvoujetových případů v difrakčních *ep* interakcích s detekovaným protonem na experimentu H1
Autor: Richard Polifka
Katedra (ústav): Ústav částicové a jaderné fyziky
Vedoucí dizertační práce: RNDr. Alice Valkárová, DrSc.
e-mail vedoucího: avalkar@mail.desy.de

Abstrakt: V této práci jsou měřeny inkluzivní dvoujetové koncové stavy v nepružných difrakčních případech s detekovaným rozptýleným protonem. Tento proton je měřen v dopředném detektoru Forward Proton Spectrometer. Vysoká statistika těchto případů v období HERA II s integrovanou celkovou luminositou 156.7 pb^{-1} umožňuje první měření tohoto druhu za celou dobu provozu experimentu HERA. Data pokrývají kinematickou oblast $x_{I\!P} < 0.1$, $|t| \leq 1.0 \text{ GeV}^2$ a $4 \leq Q^2 \leq 110 \text{ GeV}^2$. Naměřená dvoujetová data jsou porovnána s předpověďmi poruchové kvantové chromodynamiky ve druhém řádu rozvoje vazbové konstanty α_s. Tyto předpovědi jsou založené na difrakčních partonových distribučních funkcích získaných z předchozích měření inkluzivních difrakčních případů. Fázový prostor pro případy s difrakčními dijety byl rozšířen oproti předchozím měřením třikrát. Případy, kdy jeden z jetů směřuje do přední oblasti detektoru H1 by měly podporovat partonovou dynamiku mimo popis DGLAP evolučních rovnic, naměřená data jsou ovšem s výpočty založenými na DGLAP rovnicích v dobré shodě. Měřené diferenciální účinné průřezy jsou srovnány s Monte Carlo modely, které v sobě mají zahrnuty rozdílná schémata produkce difrakčních případu.

Klíčová slova: difrakce, QCD, dvoujetové případy, DGLAP, detekce rozptýleného protonu

Abstract

Title: Analysis of dijet events in diffractive ep interactions with tagged leading proton at the H1 experiment
Author: Richard Polifka
Department: Institute of Particle and Nuclear Physics
Supervisor: RNDr. Alice Valkárová, DrSc.
Supervisor's e-mail address: avalkar@mail.desy.de

Abstract: An inclusive dijet production in diffractive deep-inelastic scattering is measured. The diffractive selection is based on tagging of the leading proton in the Forward Proton Spectrometer. The statistics of events obtained during the HERA II running period (integrated luminosity of 156.7 pb^{-1}) enables the measurement of jet final states with leading proton for the first time. The data cover the phase space of $x_{I\!P} < 0.1$, $|t| \leq 1.0$ GeV^2 and $4 \leq Q^2 \leq 110$ GeV^2. The dijet data are compared with the next to leading order predictions of the quantum chromodynamics (QCD). The phase space of diffractive dijets is in this analysis by factor of 3 in $x_{I\!P}$ larger than in previous measurements. The QCD predictions based on the DGLAP parton evolution describe the measured data well even in a non-DGLAP enriched phase space where one on the jets goes into the region close to the direction of the outgoing proton. The measured single-differential cross sections are compared to several Monte Carlo models with different treatment of diffractive exchange implemented.

Keywords: diffraction, QCD, dijet events, DGLAP, leading proton

Contents

Chapter 1

Introduction

Quantum chromo dynamics (QCD) is a theory which describes the interactions of hadron constituents, called partons. According to Quark-Parton Model (QPM), one part of partons is identified with quarks and represents the building blocks of matter. The other part are gluons, the colour force carriers. The QCD predicts the phenomena known as asymptotic freedom and confinement [1],[2]. The asymptotic freedom describes the fact, that at distances significantly smaller than $1\ fm$ the interaction of quarks is getting weaker and thus in the interaction of the hadron the quarks can be assumed as independent, i.e. free. The confinement on the other hand describes the fact that no free quarks are observed, At the distance larger than the size of the proton, the colour force binds the quarks in colour neutral hadrons. The asymptotic freedoms allows application of perturbative QCD, i.e. analytical calculations of cross sections. Such calculations are possible only if a hard scale in the studied interaction is presented.

The cross section of the hadronic scattering is dominated by elastic scattering with small momentum transfers. These processes do not allow to apply the pQCD, since the scale involved is not sufficiently hard. These processes are often referred also as "diffractive" or "soft". One of the successful phenomenological models describing diffraction in terms of meson exchange was invented in the 1960's by Tullio Regge [12],[13]. In the diffractive processes the colliding particles remain intact after the interaction despite the fact, that a system is produced separated from the beam particles with a spacial gap. Due to the existence of the gap, the quantum numbers of the exchanged particle must be that of a vacuum. Such object is called the *Pomeron* ($I\!P$). The diffractive process have not been completely described in terms of pQCD up to present [20].

The *ep* collisions at the HERA collider at DESY provide a unique possibility for a deep study of the diffractive events. The probing of the proton with the virtual photon provides the necessary scale for the pQCD calculations. At HERA, the diffractive interaction is described as an interaction of the Pomeron

$I\!P$ emerging from proton with photon coming from the lepton vertex. In these events, two clearly separated systems are defined. The M_X system is the result of the $\gamma * I\!P$ interaction and is situated mainly in the central part of the detector. The M_Y system is associated with the outgoing proton or low mass dissociative systems located around the beam-pipe in the direction of the outgoing proton. The tagging of the outgoing proton is possible with the H1 forward detectors, the reconstruction of the diffractive variables is then very precise.

Theoretical calculations show that the diffractive deep inelastic scattering (dDIS) processes can be factorised into a "hard" and "soft" part. This so called "QCD factorisation" has been proved by [21] and it is analogous to the ordinary DIS. The hard part is represented by the matrix element calculation in pQCD, the soft part consists of universal diffractive parton distribution functions (dPDF). This model can be extended to the "resolved pomeron model" [25], [24], which assumes the "Regge factorisation", i.e. splitting the universal dPDFs into a probability of a pomeron emerging from proton and into the pomeron structure function. Several measurements at H1 and ZEUS have been undertaken and prove that the factorisation in diffractive DIS holds [19],[35].

This analysis measures the diffractive dijet cross sections with tagged outgoing proton. It is the first measurement of dijets using tagged proton data in the history of the H1 experiment. The aim of the analysis is to measure the dijet cross sections with longitudinal fraction of proton energy up to $x_{I\!P} < 0.1$ and compare it to the predictions of next-to-leading QCD calculations and Monte Carlo models. The selection based on the tagged proton allows us to investigate the hadronic final state going into the forward direction. This fact allows measurement of jets separated by gap which allows to study DGLAP parton dynamics.

Chapter 2

Theoretical Overview

2.1 Electron Proton Scattering at HERA

In the electron-proton collisions, the electron interacts via emitting a virtual photon, W or Z boson. This exchange boson, according to Quark Parton Model, interacts with one of the constituents of proton, so called partons. According to the photon[1] virtuality, two processes are distinguished: Deep Inelastic Scattering (DIS) and photoproduction (PHP). The transition is defined as the square of the proton mass, i.e. $1\ GeV^2$.

2.1.1 The Quark Parton Model

According to the Quark Parton Model (QPM) developed in the 1960's the proton consists of quarks and gluons [22], [23]. According to static QPM every hadron, i.e. composite object, consists of a certain number of valence quarks. The interaction of hadrons is described as interaction of the probe with one of the proton constituents. The other quarks are independent and do not interact. For calculations, the concept of proton structure functions has been invented. Proton structure function is a set of parton distribution functions - probabilities, that a parton with given kinematics will be found in the proton.

2.1.2 The DIS Kinematics

In order to describe the processes $ep \rightarrow e'X$ one has to define basic kinematic variables. Let's denote $k(k')$ the four-momentum of the incoming(outgoing) electron and P the four-momentum of the incoming proton. Then we can define the centre of mass energy $\sqrt{s}$, the mass, i.e. virtuality, of the photon Q^2 and the

---

[1]The exchange boson will be referred as photon
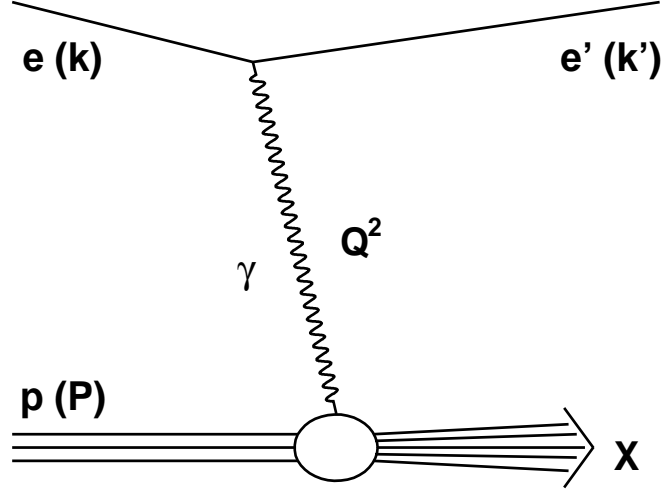
Figure 2.1: Schematic view of DIS scattering

fraction of the interacting parton momentum with respect to the proton, called x_{Bj}

$$s = (k + P)^2 \qquad (2.1)$$
$$Q^2 = -q^2 = (k' - k)^2 \qquad (2.2)$$
$$x_{bj} = \frac{Q^2}{2P \cdot q} \qquad (2.3)$$

The meaning of the variables is described in the Fig.2.1. From these variables it is possible to derive the inelasticity of the process y

$$y = \frac{q \cdot P}{k \cdot P} \approx \frac{Q^2}{x_{Bj} \cdot s} \qquad (2.4)$$

2.1.3 Cross Section in QPM

In the QPM, the cross section for the inclusive deep inelastic scattering is the incoherent sum of each individual electron parton reaction $eq \rightarrow e'q'$. Only charged particles are considered due to electromagnetic interaction. Therefore in order to calculate the ep cross section, one has to calculate the QED scattering of electron with momentum k and quark with momentum xP and integrate over

10
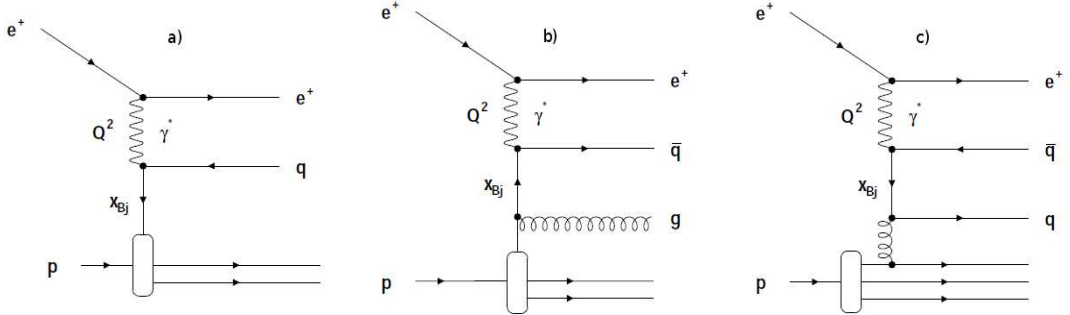
Figure 2.2: Feynman diagrams of deep inelastic scattering without QCD corrections in a), with first order in α_s correction in b) and with second order in α_s correction in c).

the probability of finding a quark with the proton momentum fraction x within the proton. If considering electron and quark mass-less (which can be done for the light quarks) fermions and protons and electrons being unpolarised, the cross section can be calculated as:

$$\frac{d\sigma(eq \to e'q')}{dQ^2} = \frac{2\pi\alpha_{em}^2 e_q^2}{Q^4}\left(1 + (1-y)^2\right),\tag{2.5}$$

where α_{em} is the electromagnetic coupling constant and e_q the charge of the quark. The variables related only to the electron vertex (see definitions in Sec. 2.1.2) are independent on the proton vertex, i.e. the definitions hold also for the eq scattering. The DIS scattering cross section is then defined as:

$$\frac{d^2\sigma}{dx_{Bj}dQ^2} = \frac{2\pi\alpha_{em}^2}{Q^4 x_{Bj}}\left(1 \pm (1-y)^2\right)F_2^{QPM}(x_{Bj}),\tag{2.6}$$

$$F_2^{QPM}(x_{Bj}) = x_{Bj}\sum_q e_q^2 f_q(x_{Bj}),\tag{2.7}$$

where f_q denotes the probability of finding a quark inside the proton with momentum fraction x_{Bj}. The $F_2(x_{Bj})$ is the structure function depending only on x_{Bj} and it sums over all quark flavours. The dependence only on x_{Bj} is called Bjørken scaling. If the squared momentum transfer at the electron vertex is significantly smaller than the square of the Z boson mass, the electroweak contribution to the matrix element can be neglected. Deviations from this cross section definition are expected for $Q^2 > m_Z^2$, which is not in the Q^2 range of this analysis and can be therefore neglected.

2.1.4 The Quantum Chromodynamics

In order to describe the dynamics of strong interaction, a non-abelian gauge theory based on $SU(3)$ group has been developed, the quantum chromodynamics (QCD). The basic fermions are quarks, which form three generations (with six flavours in total for all generations: *up*, *down*, *strange*, *charm*, *bottom* and *top*). The quarks form $SU(3)$-triplets with respect to a newly introduced quantum number, colour. The gluons are carriers of the strong colour force and they bind the quarks together in hadrons. Like in other non-abelian gauge theories, the coupling constant (denoted as α_s) depends due to quantum fluctuations on the momentum scales involved in the interaction. Unlike in the electroweak interaction, α_s is rising with decreasing momentum scales, leading to the phenomena of confinement and asymptotic freedom [1],[2]. The rising of α_s can be interpreted in terms of a colour string spanned between the two interacting partons which is becoming stronger with the distance and binds the constituents together. The confinement is responsible for the fact that only colour neutral singlets (i.e. hadrons) are observed in the experiments. For the applicability of the perturbative calculations, the phenomenon of asymptotic freedom is of vital importance. Within the infinite momentum frame, the partons are moving independently on each other, therefore the electron-proton scattering at high energies can be described as electron-quark scattering. The rest proton constituents do not interfere in the interaction itself, they form a colour neutral final state after the collision.

The success of QCD lies in the experimental measurements, which supported the theoretical predictions of this new theory. The quark parton model assumes the dependence of the structure function of the proton only on the momentum fraction x_{Bj}. The QCD introduces also a Q^2 dependence, known as Bjorken scaling violation.

There are two modifications of the naive QPM by the QCD. On one hand the Q^2 dependence of the proton structure function is imposed, on the other hand the strong interaction adds additional matrix elements to the simple QPM electron-hadron interactions. The Fig. 2.2 shows Feynman diagrams for the simple QPM model and the corrections due to QCD up to the second order in α_s. The introduction of the QCD corrections significantly influences the theoretical calculations of the cross sections. Due to the very complex structure of the QCD, the newly imposed diagrams lead to several complications which will be discussed below.

2.1.5 Renormalisation

While dealing with the QCD corrections to the QPM cross sections, divergent terms in calculations appear. In pQCD the sum over matrix elements that need

to be taken into account contains factors, that are integrals over phase space of real and virtual particles. A regularisation scheme has to be defined in order to take care of such divergent terms while maintaining the physical significance of the calculation. There are several possibilities to choose the regularisation scheme, all of them introduce a renormalisation scale μ_r. Since the dependence on the scale is unphysical, an "effective" coupling constant $\alpha_s(\mu_r)$ is defined. The fact, that the calculations are μ_r dependent is explained in only finite number of orders in $\alpha_s(\mu_r)$ that can be taken into account due to due to computational complexity. The additional requirement of non-dependence of the physical cross sections leads to renormalisation group equations which determine the α_s dependence on μ_r. The equations has not been solved analytically, however analytically accessible expansions have been made. For next-to-leading calculations used in this analysis, the formula for running α_s is given by [5]:

$$\alpha_s(\mu_r) = \frac{4\pi}{\beta_0 ln(\mu_r^2/\lambda^2)}\left(1 - \frac{2\beta_1}{\beta_0^2}\frac{ln[ln(\mu_r^2/\lambda^2)]}{ln(\mu_r^2/\lambda^2)}\right), \tag{2.8}$$

$$\beta_0 = 11 - \frac{2}{3}n_f, \tag{2.9}$$

$$\beta_1 = 51 - \frac{19}{3}n_f, \tag{2.10}$$

where λ is a free parameter and μ_r, the QCD scale, has to be determined from the experiments. The n_f stands for the number of quark flavours used in the calculations. The experimental value for α_s is typically given at the Z^0 boson mass, the current world's average is $\alpha_s\left(M_Z^2\right) = 0.1187 \pm 0.002$ [5].

2.1.6 Factorisation in DIS and Evolution Equations

A scale dependence similar to the dependence of the $\alpha_s\mu_r$ is present in the parton densities. The emission of very soft gluons and the corresponding divergences can be absorbed into the "effective" coupling constant, but other infinities may occur from the partons which are emitted collinearly, i.e. with small opening angles. These divergences are treated by factorisation, while a new scale - factorisation scale μ_f - is imposed. This scale can be interpreted as a threshold of cutoff, below which the emitted partons are treated as a part of the parton densities and above as a part of the hard scattering matrix element. This treatment leads to dependence of the parton densities on the factorisation scale μ_f. Similar to the requirement of independence of the cross section on μ_r, independence of the parton densities on μ_f lead to series of differential equations. These equations are called evolution equations and, similar to $\alpha_s(\mu_r)$, full analytical solution is incalculable at present time. The two models described below use approximate approach and can be used only in limited phase space.
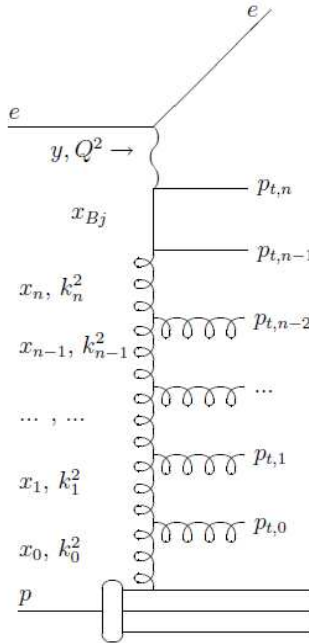
Figure 2.3: The gluon ladder associated with the DGLAP evolution equations. Strong ordering in $p_{t,i}^2$ and simple ordering in x_i is assumed.

DGLAP Evolution Equations

The DGLAP (Dokshitzer-Gribov-Lipatov-Altarelli-Parisi) are summing up terms proportional to $\log Q^2$, but neglecting terms proportional to $1/x_{Bj}$ [6],[7],[8]. The equations for quark and gluon densities are defined as follows:

$$\frac{df_q(x,Q^2)}{d\log(Q^2)} = \frac{\alpha}{2\pi} \int_x^1 \frac{dy}{y} \left(P_{qq}\left(\frac{x}{y}\right) f_q(y,Q^2) + P_{qg}\left(\frac{x}{y}\right) f_g(y,Q^2) \right), \quad (2.11)$$

$$\frac{df_g(x,Q^2)}{d\log(Q^2)} = \frac{\alpha}{2\pi} \int_x^1 \frac{dy}{y} \left(P_{gg}\left(\frac{x}{y}\right) f_q(y,Q^2) + \sum_q P_{gq}\left(\frac{x}{y}\right) f_g(y,Q^2) \right). \quad (2.12)$$

The splitting functions give the probability of a parton with relative momentum fraction $(1-z)$ being emitted from the mother parton. In leading order, they are defined as follows:

$$P_{qq}(z) = \frac{4}{3}\frac{1+z^2}{1-z}, P_{qg}(z) = \frac{1}{2}(z^2 + (1-z)^2), \quad (2.13)$$

14
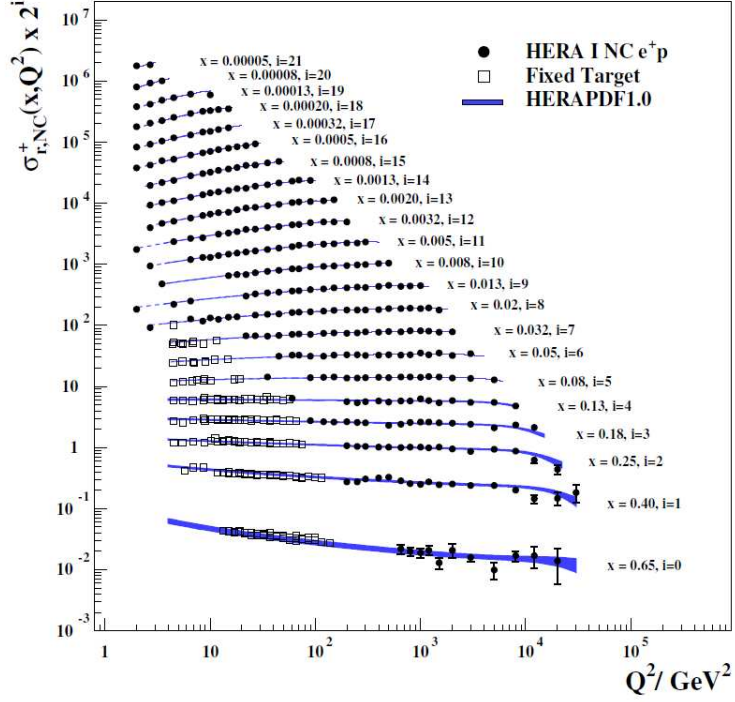
Figure 2.4: Combined neutral current e^+p reduced cross section and fixed-target data as a function of Q^2. The HERAPDF1.0 fit is superimposed, the bands represent the total uncertainty of the fit.[11]

$$P_{gg}(z) = 6\left(\frac{z}{1-z} + \frac{1-z}{z} + z(1-z)\right), P_{gq}(z) = \frac{4}{3}\frac{1+(1-z)^2}{z}. \qquad (2.14)$$

In this way, the DGLAP evolution equations can describe how a parton with momentum fraction x_{Bj} emerges from a parton with higher momentum fraction y. The parton densities at an initial starting scale Q_0^2 have to be determined from the experiment, but having these initial conditions fixed, the DGLAP evolution equations can describe the parton evolution at any scale Q^2. The easy way how to visualise the DGLAP evolution equations is in form of a ladder-diagram shown on Fig.2.3. In this evolution scheme, the strong ordering in transverse momenta and simple ordering in momentum fraction x is assumed:

$$p_{t1}^2 << p_{t2}^2 << ... << p_{tn}^2 < Q^2 \qquad (2.15)$$
$$x_1 > x_2 > ... > x_n \qquad (2.16)$$
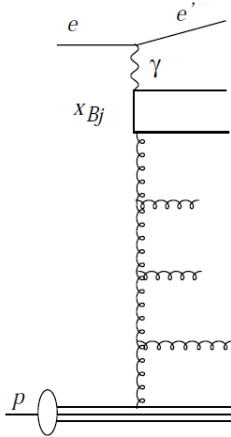
Figure 2.5: The gluon ladder associated with the BFKL evolution equations. Relaxing of the p_t ordering is schematically presented.

The fit at a starting scale Q^2 has been performed and the HERAPDF1.0 [11] fit on reduced cross sections is presented in the Fig. 2.4. The reduced neutral current cross section of $e^\pm p$ is defined as follows:

$$\sigma_{r,NC}^\pm = \frac{d^2\sigma_{NC}^{e^\pm p}}{dxdQ^2} \cdot \frac{Q^4 x}{2\pi\alpha_{em}^2(1+(1-y)^2)} \qquad (2.17)$$

The DGLAP evolution equations show a good description over a large region of the phase space.

BFKL evolution equations

The DGLAP evolution equations are applicable in a wide range of Q^2 and x. Since there is no control of the terms in $\frac{1}{x}$, the DGLAP evolution equations are limited in the low x region. The BFKL (Balitsky-Fadin-Kuraev-Lipatov) evolution equations [9],[10] impose only strong ordering in the momentum fractions, they leave the transverse momenta o the emitted partons unordered. The Fig. 2.5 shows the parton emissions in the BFKL scheme.

$$x_1 >> x_2 >> ... >> x_n \qquad (2.18)$$

The measurements in the low x phase space region can help to distinguish whether the DGLAP or BFKL evolution equations are favoured.

2.1.7 Hadronisation

The cross sections calculated for the hard scattering are calculated in terms of partons - quarks and gluons. Due to the effect of confinement which forbids existence of free colourful partons, in the detector there are only stable hadrons observed. In order to take into account this effect, hadronisation from partons to hadrons has to be taken into account. In this analysis, the Lund String Model[28] has been used for simulation of hadronisation.

2.2 Diffraction

Diffraction in the high energy particle scattering describes processes, where the colliding particles remain intact even after the interaction. Unlike in the elastic scattering processes, there is an energy flow coming from the interaction which is not associated with the outgoing particles. It is characterised by low momentum transfer, therefore these events belong to the type of soft events. This means that the usage of perturbative QCD is not possible and different phenomenological approaches have to be used. The Regge theory was successful in describing the behaviour of the total cross section and it is still widely used for describing diffractive processes.

The hard diffractive scattering allows calculating matrix elements within pQCD due to the presence of a hard scale. This is usually provided in the diffractive jet measurements.

2.2.1 Regge Phenomenology

The Regge Phenomenology was developed in 1960' [12],[13] to describe the behaviour of the total cross section of the hadron-hadron interactions as a function of central mass energy of the interaction $\sqrt{s}$. The interaction is described in terms of meson exchange, but it is not treating the mesons as individual particles. It associates mesons with identical quantum numbers except for the angular momentum into so called Regge trajectories. The cross sections for the high colliding energies can be then parametrised as

$$\frac{d\sigma}{dt} \sim F(t) \frac{s}{s_0}^{2(\alpha(t)-1)}, \tag{2.19}$$

$$\alpha(t) = \alpha(0) + \alpha' t, \tag{2.20}$$

where $\alpha(0)$ and α' are the intercept of the regge trajectory for $t = 0 \ GeV^2$ and the slope of this trajectory respectively. The trajectory is derived in the t - J plane where t is the four momentum transfer and J is the angular momentum.
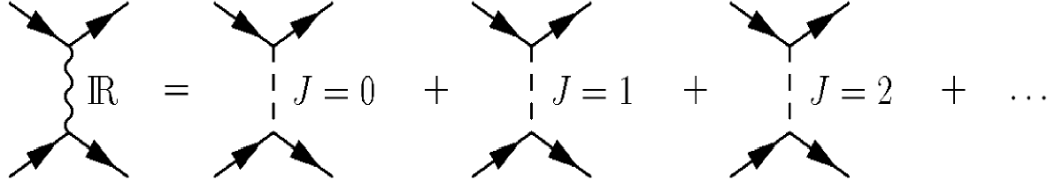
Figure 2.6: The Reggeon trajectory is equivalent tu sum over exchange of different mesons.

The Reggeon trajectory or *Reggeon* $I\!R$ is the sum of trajectories over possible meson trajectories, schematically displayed in Fig. 2.6. The Reggeon intercepts $\alpha_{I\!R}(0)$ are of the order of 0.5. From the fits to the experimental data [14] the necessity of an other trajectory with intercept > 1 emerged, since the total cross section rises with $\sqrt{s}$. The total hadron-hadron cross section as a function of $\sqrt{s}$ is presented in Fig. 2.7. The fit to the cross section is a sum over reggeon and pomeron trajectories:

$$\sigma_{tot} = X s^{\alpha_{I\!P}(0)-1} + Y s^{\alpha_{I\!R}(0)-1}. \tag{2.21}$$

The first term in the Eq. 2.21 was called Pomeron ($I\!P$) trajectory and it corresponds to an exchanged object with vacuum quantum numbers. It does not correspond to any know particle, but it succeeded in description of the diffractive processes. The current experimental value of the reggeon intercept is $\alpha_{I\!R}(0) = 0.50 \pm 0.1$ and pomeron intercept is $\alpha_{I\!P}(0) = 1.111 \pm 0.007$ [19]

2.2.2 Diffraction in DIS

The *ep* collider HERA offers a unique possibility to study diffraction. There is a possibility to investigate $\gamma^* I\!P$ processes where the photon probes the structure of the Pomeron trajectory [2]. The $\gamma^* I\!P$ interaction produces two systems clearly separated in pseudorapidity defined as

$$\eta = -\ln \tan(\frac{\theta}{2}) \tag{2.22}$$

The system localised mainly in the central detector, M_X, corresponds to the energy deposition of the $\gamma^* I\!P$ interaction, the system M_Y corresponds to the system of the outgoing proton or its low mass excitations (Fig 2.8). There are two basic experimental methods how to select diffraction. The Large Rapidity Gap

---

[2]from now on, it will be denoted only as $I\!P$
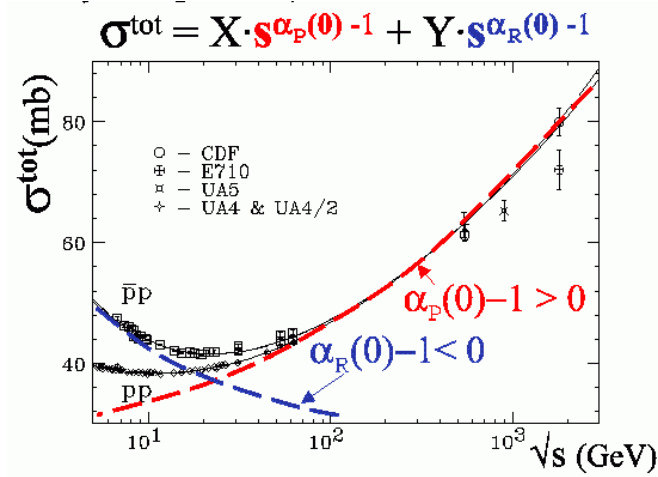
Figure 2.7: The total cross section as a function of central mass energy $\sqrt{s}$.

(LRG) method demands a cut on the energy activity in the forward region of the detector. The other method is selecting the outgoing scattered proton with a forward detectors. The LRG method is able to gather large statistics, but the signal is spoilt by proton dissociation process, which has to be considered as background. Tagging of the scattered proton suffers from limited acceptance of the forward detector, on the other hand there is no proton dissociation background present and it allows a precise reconstruction of the diffractive kinematical variables.

The $x_{I\!P}$ variable is defined as the fraction of the longitudinal proton momentum which interacts with the photon:

$$x_{I\!P} = 1 - \frac{E'_p}{E_p} \tag{2.23}$$

The variable t is defined as the square of the four momentum transferred at the proton vertex:

$$t = (p' - p)^2 \tag{2.24}$$

In order to describe the diffractive parton densities, one has to define the longitudinal momentum fraction of the quark struck from the $I\!P$, which goes into the interaction:

$$\beta = \frac{x_{Bj}}{x_{I\!P}}. \tag{2.25}$$

19
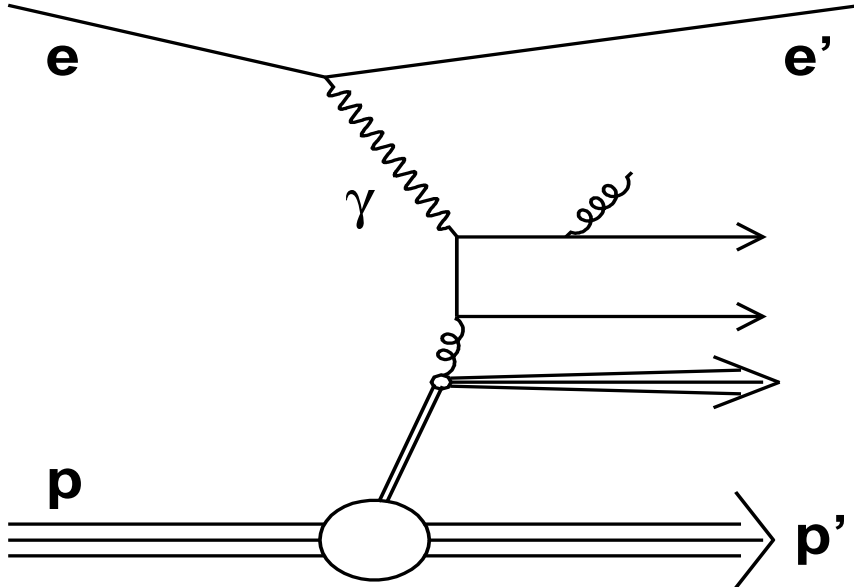
Figure 2.8: Diffractive Boson-Gluon Fusion process.

2.2.3 Factorisation in Diffractive DIS

Similarly to the inelastic ep interaction while studying the structure of the proton, the diffractive processes can be investigated following the same logic. The inclusive DIS is described in terms of universal parton densities of the proton and hard parton-parton scattering matrix elements [22], [23]. For the diffractive processes it has been proved, that the factorisation holds and the calculation can be split up into universal diffractive parton densities f_i^D and hard matrix elements [21]. This factorisation is called "QCD Factorisation". The cross section is then written as a convolution of the parton densities and the matrix elements:

$$d\sigma^{ep\to e'XY}(Q^2, |t|, M_Y, \beta, x_{I\!\!P}) = \sum_i f_i^D(Q^2, |t|, M_Y, \beta, x_{I\!\!P}) \otimes d\hat{\sigma}^{ei}(Q^2, x_{Bj} = x_{I\!\!P} \cdot \beta),$$

(2.26)

where the sum runs over all quark flavours i. The partonic cross sections $d\hat{\sigma}^{ei}$ are calculable in pQCD and like in the non-diffractive DIS depend only on x_{Bj} and Q^2. The diffractive parton densities f_i^D are universal, i.e. independent on specific process. This independence offers the possibility to extract the diffractive parton densities from inclusive measurements and predict cross sections for other processes like for dijets in this analysis.

For inclusive diffractive DIS, the diffractive structure function $F_2^{D(5)}$ similar to Eq. 2.6 for the non-diffractive case can be defined

$$\frac{d\sigma^5_{ep \to e'XY}}{dx_{I\!\!P} d\beta dQ^2 dM_Y d|t|} = \frac{4\pi\alpha^2_{em}}{\beta^2 Q^4} \left(1 - y + \frac{y^2}{2(1 + R^{D(5)})}\right) F_2^{D(5)}. \qquad (2.27)$$

Similarly to Eq. 2.6, the ratio of longitudinal and transverse photon cross section $R^{D(5)}$ is neglected in further considerations. In this analysis, the system Y is defined as $M_Y = M_p$ and the measurement of the dependence of the cross section on the squared momentum transfer $|t|$ is possible. After the integration we get

$$\frac{d\sigma^3_{ep \to e'Xp'}}{dx_{I\!\!P} d\beta dQ^2 d|t|} = \frac{4\pi\alpha^2_{em}}{\beta^2 Q^4} \left(1 - y + \frac{y^2}{2}\right) F_2^{D(4)}(x_{I\!\!P}, \beta, Q^2, |t|). \qquad (2.28)$$

2.2.4 Resolved Pomeron Model

Even though the pomeron is not well defined in terms of hadrons, the Resolved Pomeron Model [24],[25] interprets the diffractive structure function $F_2^{D(4)}$ as a sum of probabilities of finding a parton in the pomeron convoluted with the probability of finding a pomeron in the proton:

$$F_2^{D(4)}(x_{I\!\!P}, |t|, \beta, Q^2) = f_{I\!\!P/p}(x_{I\!\!P}, |t|) \otimes F_2^{I\!\!P}(\beta, Q^2) + f_{I\!\!R/p}(x_{I\!\!P}, |t|) \otimes F_2^{I\!\!R}(\beta, Q^2), \qquad (2.29)$$

where the $f_{I\!\!P,I\!\!R/p}$ are the probabilities to find pomeron (reggeon) in the proton, called the pomeron(reggeon) flux and defined as

$$f_{I\!\!P,I\!\!R/p}(x_{I\!\!P}, t) = A_{I\!\!P,I\!\!R} \cdot \frac{e^{B_{I\!\!P,I\!\!R} t}}{x_{I\!\!P}^{2\alpha_{I\!\!P,I\!\!R}(t)-1}} \qquad (2.30)$$

and the probabilities $F_2^{I\!\!P,I\!\!R}$ to find a parton with a momentum fraction β in the pomeron (reggeon), i.e. the "structure functions of the pomeron (reggeon)" as:

$$F_2^{I\!\!P,I\!\!R}(\beta, Q^2) = \sum_i e_i^2 \beta f_i^{I\!\!P,I\!\!R}(\beta, Q^2) \qquad (2.31)$$

In the phase space of high $x_{I\!\!P}$ of this measurement the reggeon contribution plays a non-negligible role and therefore has to be taken into considerations.
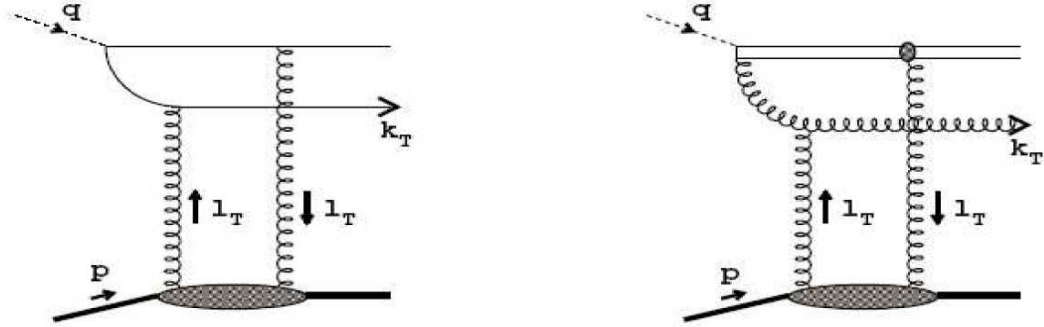
Figure 2.9: Schemes of the two gluon exchange process.

2.2.5 Direct Pomeron Model

The simple way how to create a colour neutral object that can mimic the pomeron exchange in terms of pQCD is a two gluon exchange model by J. Bartels [26]. The idea of the gluon-bound state is presented in the Fig. 2.9. This model is suitable for search for the exclusive dijet production, since there is no pomeron remnant. The whole momentum fraction carried by the exchanged gluons is transferred into the quark-antiquark pair emerging from the photon.

2.2.6 Soft Colour Interaction

The regions of the phase space, where the perturbative QCD cannot be applied can be investigated with the soft colour exchange models. The basic idea behind this model is variation of colour string-field topologies which can give a unified description of final state.

The Soft Colour Interaction model [27] assumes exchange of colour-anticolour charges. This exchange corresponds to non-perturbative gluons between partons and remnants which emerge from a hard scattering. The concept works with the idea of partons interacting softly with the colour medium of the proton as they propagate through it, which should be a natural part of the process in which "bare" perturbative partons are "dressed" into non-perturbative ones and the confining colour flux tube between them is formed. The Soft Colour Interaction model is schematically presented in Fig. 2.10.

A modification to this model uses a Generalised Area Law (GAL) [59]. In this model configurations where a colour string spans a large area in energy-momentum space are exponentially suppressed and therefore the probability P
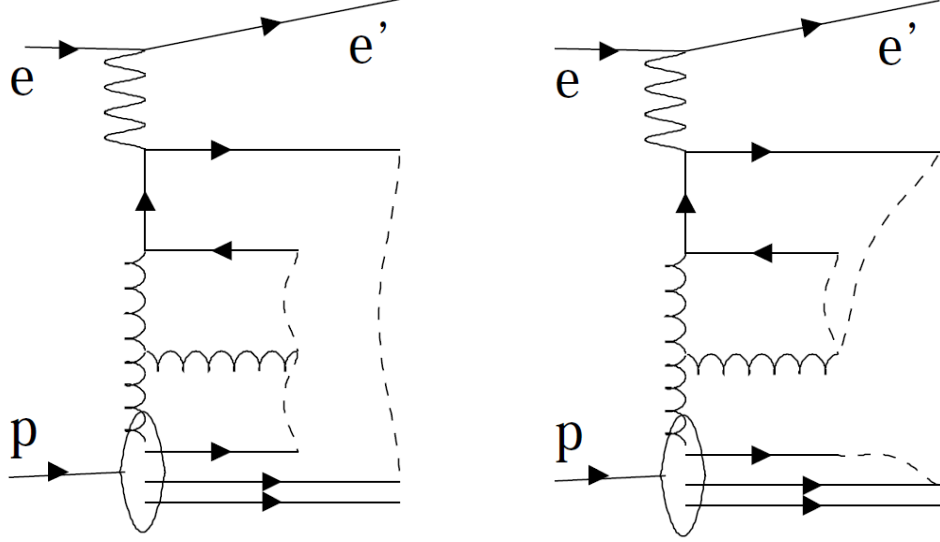
Figure 2.10: Gluon-induced deep inelastic scattering event with examples of colour string connection (dashed lines) of partons in conventional Lund model [28] based on the colour order in pQCD (left), and after colour rearrangement through SCI mechanisms (right).

for a string rearrangement is given by:

$$P = R_0(1 - \exp(-b\Delta A)) \qquad (2.32)$$

where R_0 and b are the two parameters of the model and δA is the difference between the areas spanned by the string before and after rearrangement.

2.2.7 Jets in Diffractive DIS

The major contribution to inclusive cross section measurement of diffractive DIS comes from scattering of quarks from the pomeron. This leads to an exact extraction of the quark densities, like in [19]. The gluon density can be measured indirectly by estimating the Q^2 dependence of the quark density and for large momentum fractions β with considerable uncertainty. Other final states are sensitive to gluons directly. The dijet system, i.e. a system X with at least two hard jets, is produced via boson gluon fusion, where gluon emerges from the pomeron and interacts with the hard quark-antiquark pair which was created by the fluctuating virtual photon (see Fig. 2.8). Since the gluon interacts with "hard" quark-antiquark pair, creating the dijet system M_{12}, a sufficiently large

"hard" scale is present in the interaction and the comparison to pertubative QCD calculation can be performed.

2.2.8 Diffractive Parton Distribution Functions

The fit most succesful describing the H1 experimental data is labelled "H1 2006 Fit B" [19] and it is based on the resolved pomeron model (see Sec. 2.2.4). The data in the sample used in the fit cover the region $Q^2 \geq 8.5\ GeV^2$, $\beta \leq 0.8$ and $M_X > 2.\ GeV$. The diffractive parton distribution function in the fit is defined as

$$f_i^D(\beta, Q^2, x_{I\!P}, t) = f_{I\!P/p}(x_{I\!P}, t)f_i(\beta, Q^2) + n_{I\!R}f_{I\!R/p}(x_{I\!P}, t)f_i^{I\!R}(\beta, Q^2). \qquad (2.33)$$

where $f_{I\!P,I\!R/p}$ is the possibility to find a pomeron (reggeon) in proton as defined in Sec. 2.2.4, the $n_{I\!R}$ is the reggon normalisation parameter used as a free parameter, the $f_i^{I\!R}$ is the reggon distribution function (the $f_i^{I\!R}$ parametrisation and the values are taken from the pion structure function [45]), the $f_i(\beta, Q^2)$ is the pomeron distribution function. The DPDF are modelled in terms of a light flavour singlet distribution $\Sigma(z)$, consisting of u, d and s quarks and anti-quarks with $u = d = s = \bar{u} = \bar{d} = \bar{s}$, and a gluon distribution $g(z)$. Here, z is the longitudinal momentum fraction of the parton entering the hard sub-process with respect to the diffractive exchange, such that $z = \beta$ for the lowest order quark-parton model process, whereas $0 < \beta < z$ for higher order processes. The quark singlet and gluon distributions are parametrised at $Q_0^2 = 2.5\ GeV^2$ using a similar approach to that commonly applied to hadronic parton densities [46], such that the most general form is

$$zf_i(z, Q_0^2) = A_i z^{B_i}(1 - z)^{C_i}, \qquad (2.34)$$

where i stands either for the singlet or gluon distribution.

The detailed description of the fit procedure can be found in [19].

The recent diffractive fit which includes also jet data [47] is labelled as "H1 2007 Jets" and it is based on the large rapidity inclusive diffractive DIS measurement and on the large rapidity gap measurement of dijets in diffractive DIS. The same parametrisation of the parton densities as in the "H1 2006 Fit B" is used. The scale is chosen to be $\mu_f^2 = Q^2 + p_{T,jet1}^{*2}$ with the starting value $\mu_{f,0}^2 = 2.5\ GeV^2$. The data are measured in the range $29\ GeV^2 < Q^2 + p_{T,jet1}^{*2} < 200\ GeV^2$ and fitted for $0.05 < z_{I\!P} < 0.9$. The fit "H1 2007 Jets" gives a slightly smaller predictions of the cross sections of the dijet data in comparison to the "H1 2006 Fit B" (see Fig. 2.11). The detailed description of the fit procedure can be found in [47]. The results for the fit parameters (Eq. 2.34) are given in the Table 2.1.

24
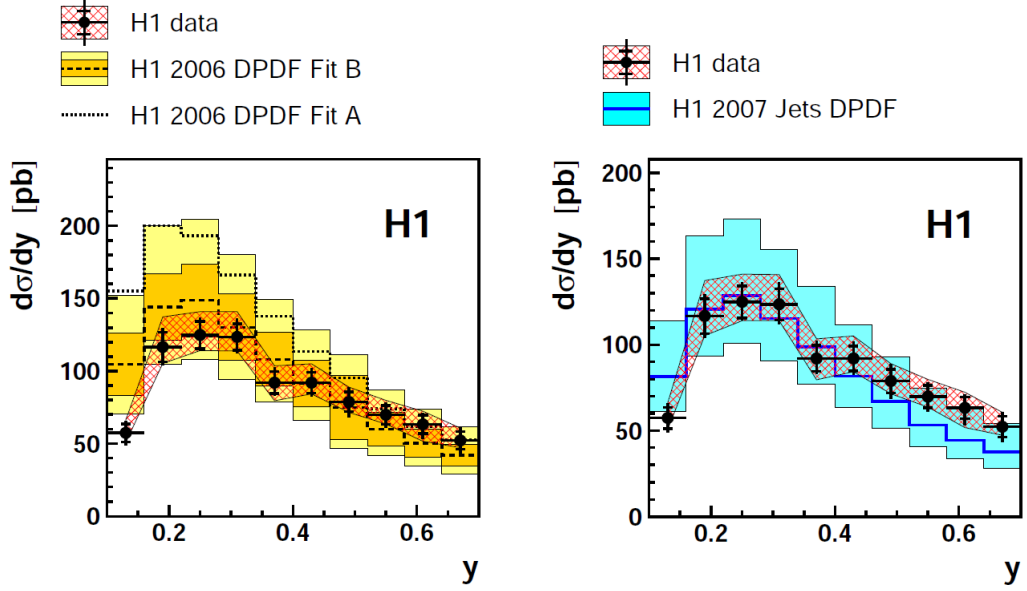
Figure 2.11: Differential cross section in y measured in LRG diffractive dijet analysis [47] compared to the H1 2006 Fit B (left) and H1 2007 Jets (right).

Fit Parameter	H1 2006 B	H1 2007 Jets
$\alpha_{I\!P}(0)$	1.111 ± 0.007	1.104 ± 0.007
$n_{I\!R}$	$(1.4 \pm 0.4) \cdot 10^{-3}$	$(1.3 \pm 0.4) \cdot 10^{-3}$
A_q	0.70 ± 0.11	0.13 ± 0.02
B_q	1.50 ± 0.12	1.50 ± 0.12
C_q	0.45 ± 0.09	0.51 ± 0.08
A_g	0.37 ± 0.02	0.88 ± 0.17
B_g	$(0) fixed$	0.33 ± 0.10
C_g	$(0) fixed$	0.91 ± 0.18

Table 2.1: Parameters of the inclusive DIS diffractive fit "H12006 Fit B" and inclusive + dijet DIS diffractive fit "H1 2007 Jets".

2.3 Analysis Motivation

In [47] the dijets in diffractive DIS have been measured and the DPDF H1 2007 Jets have been estimated. The diffractive events have been selected with the LRG method (see Sec. 2.2.2). The current analysis selection is done with measuring the scattered proton. Such selection allows to reconstruct the diffractive kinematics very precisely and independently on the central detector. Therefore it can extend the phase space with respect to previous measurements done with the help of the LRG method and also test the DPDFs obtained with this method. Measuring the t-dependence of the dijet cross section obtained with tagged proton data allows to test the universality of the $I\!P$ flux Ansatz in the DPDFs estimated with the data selected with the LRG method.

Measurement of the jets in the final state can distinguish between several models of diffractive exchange described in the sections above. Observable, which makes the differentiation possible is $z_{I\!P}$:

$$z_{I\!P} = \frac{M_{12}^2 + Q^2}{M_X^2 + Q^2} = \frac{M_{12}^2 + Q^2}{x_{I\!P} \cdot y \cdot s} = \beta \cdot \left(1 + \frac{M_{12}^2}{Q^2}\right), \qquad (2.35)$$

with M_{12} being the invariant mass of the dijet system and M_X mass off the whole system X. From the definition the meaning of the observable is obvious, it represents the fraction of the mass of the system X contained in the dijet system itself. In order to obtain best reconstruction resolution the definition using the scattered proton kinematics is used in this analysis.

The analysis of diffractive events with tagged scattered proton opens an unique opportunity to investigate the phase space in the forward region. This allows us to measure the dijet system with large rapidity separation. Such a configuration, where one of the jets is going close to the direction of the outgoing proton, allows the search for the BFKL-type of parton dynamics. Since the BFKL evolution equations (see Sec. 2.1.6) do not require the emitted gluons to be ordered in transverse momentum p_T, a high p_T jet can be formed by a parton radiated close to the beginning of the gluon ladder. Studying jets with tagged outgoing proton offers therefore a possibility to search for different types of parton dynamics.

Chapter 3

HERA and the H1 Detector

In order to investigate the structure of matter, an extraordinary facility is necessary. This facility is an accelerator of elementary particles and it is able to give us a picture of matter constituents of the size of $\sim 10^{-15}\ m$. Data presented in this analysis have been collected with the H1 detector, which was part of the HERA[1] accelerator complex located in DESY[2] in Hamburg, Germany. The HERA accelerator is a lepton[3]-proton collider, which makes the discovering of the structure of the proton possible. HERA was operational between years 1994 and 2007.

3.1 The HERA Accelerator

HERA is a circular accelerator with a stable orbit of protons and leptons with a circumference of 6.3 km. The time of operations was divided into two parts, HERA-I (1994-2000) followed by an upgrade and the HERA-II period (2004-2007). In the HERA-I period, HERA collided electron with beam energy of 27.6 GeV and protons with 820 GeV, since upgrade in 1998 the proton beam energy has been increased to 920 GeV which corresponds to total centre-of-mass energy of $\sim 319\ GeV$. A major HERA-II upgrade of the accelerator and detectors took place in the year 2001-3. In the last year of operation, the proton beam energy has been lowered to 460 GeV and 575 GeV in order to make possible an unique measurement of longitudinal structure function of the proton, F_L.

The acceleration of the colliding particles consists of several stages and is presented in the Fig. 3.1 a). The electrons are produced and preaccelerated in the LINAC-II facility to the energy of 500 MeV. The next stage is the DESY-II ring which accelerates the electrons up to 7.5 GeV, then the injection to the PETRA facility follows. Here the electrons are filled into up to 60 bunches and

---

[1]Hadron Elektron Ring Anlage
[2]Deutsches Elektronen Synchrotron
[3]electron or positron, from now on, the term electron will be used for both types
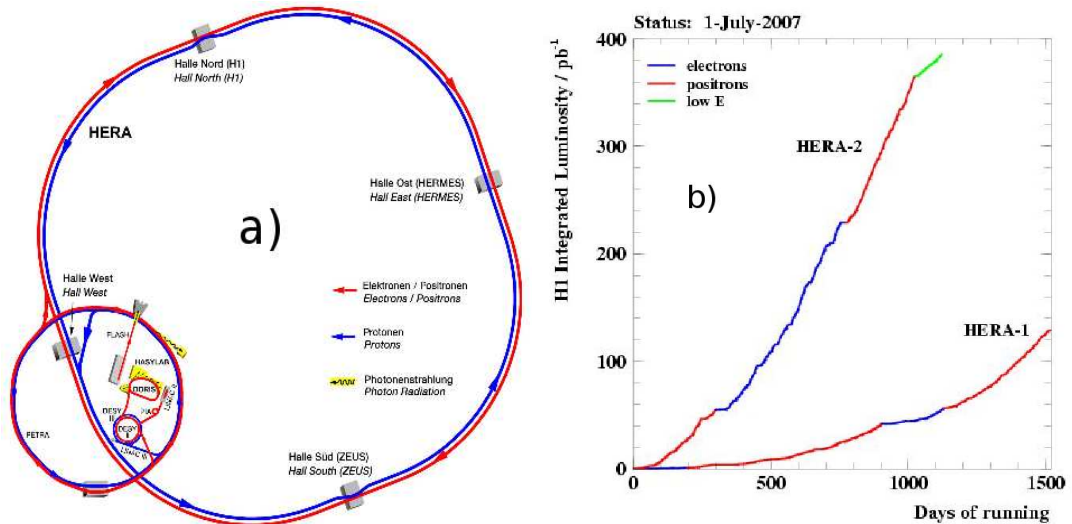
Figure 3.1: The schematic view of the HERA accelerator (left). The integrated luminosity collected during the HERA operating time (right).

accelerated to 12 GeV. Four such PETRA fillings are then injected into the main HERA system and accelerated up to the colliding energy.

Free protons are produced from the negatively charged atoms of hydrogen. The LINAC III accelerated the H^- atoms to 50!MeV and then the protons are separated by a stripping foil which absorbs the electrons. In the DESY-III ring the protons are accelerated up to 7.5 GeV and injected into PETRA. Here up to 70 bunches are filled and accelerated up to 40 GeV, then the injection to the HERA system follows. Each of the proton beams consists of up to 220 bunches with $10^{10} - 10^{11}$ protons in each bunch.

The crossing rate f is 10.4 MHz and corresponds to the 96 ns distance in time between two collisions. The performance of an accelerator is given by luminosity $\mathcal{L}$, which is defined by the beam properties as follows:

$$\mathcal{L} = \frac{fN_eN_p}{4\pi\sigma_x\sigma_y}\text{cm}^{-2}\text{s}^{-1}, \tag{3.1}$$

where N_e and N_p are numbers of particles in each beam and σ_i is the collimation of the beams in the transverse directions. The number of expected events for each process is then given by the time-integrated luminosity L and the probability of the particular process (cross section σ):

$$N = \sigma L. \tag{3.2}$$

The total integrated luminosity collected during the operational time of both periods was $\sim 530 \ fb^{-1}$ and is presented in the Fig. 3.1 b).

The HERA-II luminosity upgrade increased the luminosity peak of 1.8 10^{31} $cm^{-2}s^{-1}$ in the HERA-I to 4.8 $10^{31}cm^{-2}s^{-1}$ in the HERA-II phase. This was achieved mainly by installation of new superconducting focusing magnets close to the interaction points in order to decrease the σ_i from Eq. 3.1. This upgrade lead to changes in the designs of the multi-purpose 4π H1 and ZEUS detectors, which are installed at the interaction points in the North Hall (H1) and South Hall (ZEUS) (see Fig. 3.1 a)).

3.2 The H1 Detector

Data analysed in this measurement were collected with the H1 detector. The description of the main components necessary for the analysis follows.

The H1 detector is a complex device for detecting products of the lepton-proton collisions in HERA. The detection of the particles is based on measurement of momentum and deposited energy. The size of the detector is 12m x 10m x 15m and weight of 2800 tons. The coordinate system of the H1 detector defines the positive z-axis in the direction of the outgoing proton[4], the $x - y$ plane is defined in the way that the x-axis is pointing towards the centre of the HERA ring. Due to different proton and electron beam energies the detector design has to be asymmetric to ensure the best possible measurement of the interaction products which are boosted into the forward direction. The schematic view of the H1 detector is in the Fig. 3.2, a more detailed description of H1 detector can be found e.g. in [36] and [37].

3.2.1 Tracking System

The purpose of the tracking system is to measure the momentum and tracks of the charged particles emerging from the interaction point. This is possible due to placing the tracking systems into a solenoidal magnetic field of 1.15 T produced by the superconducting magnet just outside the calorimetry of the H1 detector.

The tracking system comprises the Central Track Detector (CTD), Forward Track Detector (FTD) and the Backward Drift Chamber (BDC) as shown in Fig. 3.3. The sub-detectors are concentrically placed around the interaction point. The H1 tracking system covers almost whole angular range $5° < \theta < 178°$ and the whole azimuthal range.

The most important parts of the tracking system are the drift chambers - CJC1 and CJC2, the inner and the outer central jet chamber. The are placed
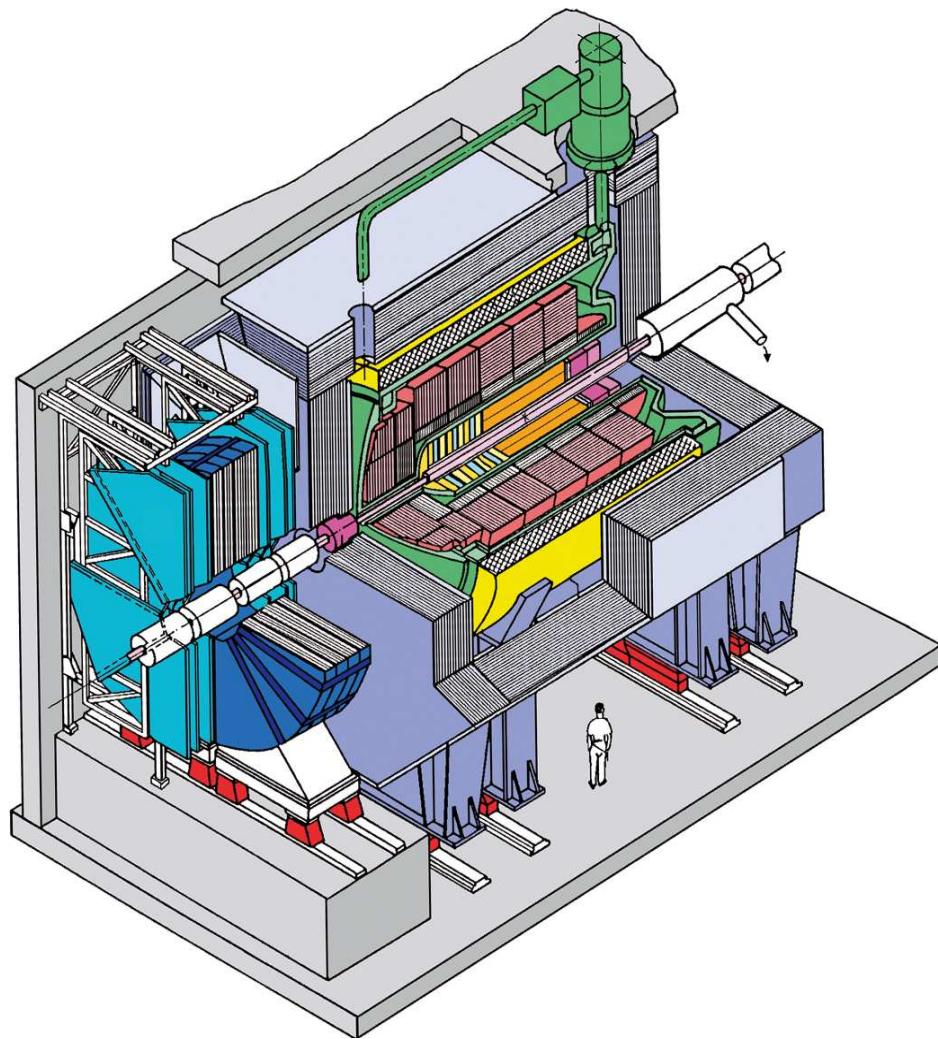
---

[4]referred to as forward direction

Figure 3.2: The schematic view of H1 detector.

into a 1.15T magnetic field which runs parallel to the z-axis. The particles follow therefore a helix trajectory through the CJC. There are 720 sensor wires running parallel to the z-axis in the CJC1 and 1920 in the CJC2. There are 30 azimuthal cells with 24 radial layers each in CJC1 and 60 azimuthal with 32 radial hit layers in CJC2. The resolution in the $r\phi$ plane is $\sim 170\mu m$ and $2-3cm$ in the z-position.

The Central Silicon Tracker (CST) is the innermost subetector of the H1 Tracking System and it surrounds directly the interaction point. The thin silicon pads are positioned around the primary vertex area in order to ensure best reconstruction of the tracks close to the event vertex. The purpose of the CST is to measure secondary vertices and therefore impact in the measurement of jets is negligible. There are 2 layers of the silicon pads in the CST with resolution of 12 μm and 22 μm respectively.

The Central Inner Proportional Chamber (CIP) is a multi-wire proportional chamber placed between the Central Silicon Tracker (CST) and CJC1. The CIP consists of 5 separate sub-chambers. Since its fast time response of $\sim 10\ ns$ the CIP is used for triggering of the events. The Central Outer Z Chamber (COZ) is situated between CJC1 and CJC2 and with the spacial resolution of 350 μm provides a precise tracking measurement.

Charged particles going into the backward direction of $152° < \theta < 177°$ are detected in the Backward Drift Chamber. The position measurement of electron candidates in the BDC can improve the measurement of the polar angle and is complementary to the measurement of the backward calorimeter. The spacial resolution of the BDC perpendicular to the beam line is $\sigma \approx 340\ \mu m$, which corresponds to a polar angle resolution of $\sigma_\theta \approx 0.5\ mrad$.

The readout channels of the CTD is are placed between CTD and FTD. The thickness of the instrumentation corresponds roughly to two radiation lengths of material. The effect of this is large multiplicity of tracks in the forward tracking detectors due to secondary interactions and the corresponding problems in track reconstruction and interpretation. For this reason the forward tracking system is not used in this analysis.

3.2.2   Calorimetry System

For the measurement of jets in deep inelastic scattering the proper reconstruction of the jets as well as the scattered electron is essential. The hadronic final state is detected with the Liquid Argon calorimeter (LAr), which covers the polar angle range $4 \leq \theta \leq 153$, the scattered electron is reconstructed in the Spaghetti Calorimeter (SpaCal) in the range of $153 \leq \theta \leq 174$. The SpaCal sub-detector is an important part of the trigger system.

The LAr calorimeter consists of eight wheels placed concentric along the z-
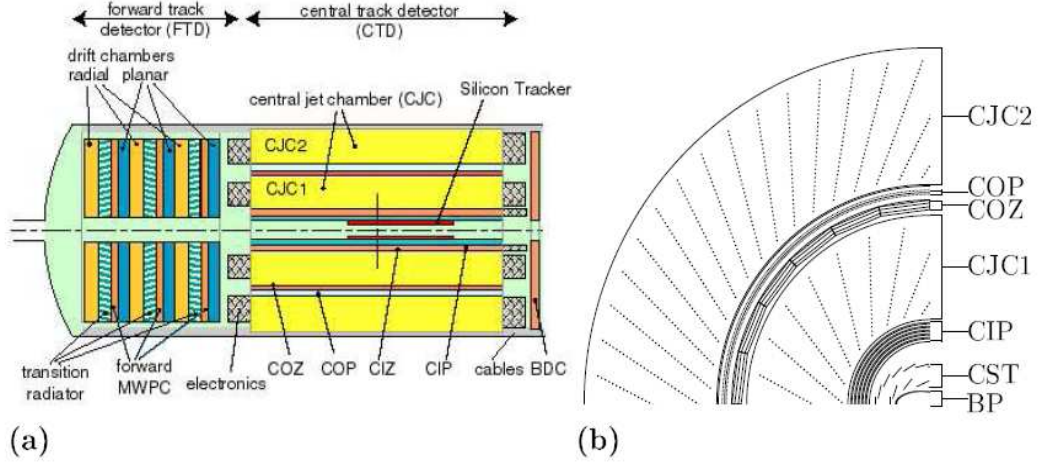
Figure 3.3: The side view of the H1 tracking system (a). The $r\phi$ view of the Central Track Detector.

axis. All wheels are housed in a single cryostat system. Each wheel is divided into 8 parts which ensures the ϕ segmentation. Each wheel has an electromagnetic and hadronic part. The good spatial resolution of the LAr calorimeter is due to the $\sim$ 45000 cells, which are the smallest constituents. The dead material regions in the detector are called cracks. The sensitive region of the detector is made of layers of absorber and sampling material. In the electromagnetic part the absorber is made of lead, the hadronic part absorber is made of stainless steel. The sampling material is same for both parts and it is the liquid argon. The charged particles produced by the interaction ionise atoms of the sampling material which produce a response in the calorimeter. The signal integrated over all layers of the detector is proportional to the energy deposited in each event. The electromagnetic part has a radial length of 22 and 30 radiation lengths in the central and forward region respectively. The hadronic part is from 5 to 8 interaction lengths thick. LAr calorimeter is non-compensating, the response to the hadronic showers is lower by approximately 30% than to electromagnetic showers due to nuclear excitations and energy lost in the cracks. This fact is corrected in the software reconstruction[48].

The resolution of the electromagnetic and hadronic parts of LAr is given by:

$$\frac{\sigma_{em}(E)}{E} = \frac{12\%}{\sqrt{E[GeV]}} \oplus 1\% \tag{3.3}$$

32
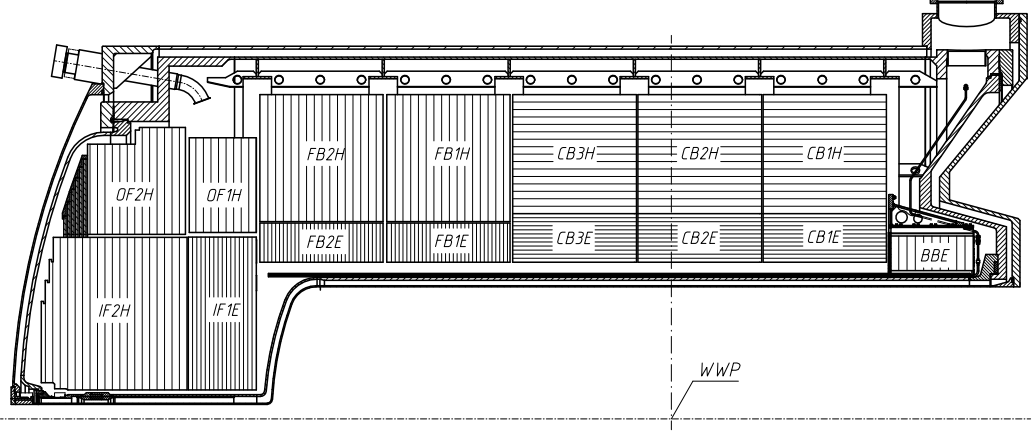
Figure 3.4: The side view of the Liquid Argon calorimeter.

$$\frac{\sigma_{had}(E)}{E} = \frac{50\%}{\sqrt{E[GeV]}} \oplus 2\%. \qquad (3.4)$$

More about the LAr calorimeter can be found in [49].

The "spaghetti" calorimeter SpaCal is placed in the backward region and is designed to detect scattered electrons. The calorimeter is divided like the LAr calorimeter into electromagnetic and hadronic part. The absorber material is lead, the signal is collected by scintillating fibres aligned parallel to the z-axis. Molecules excited by charged showers emit photons which are collected in the photomultiplier tubes (PMT) positioned on the backside of the SpaCal (backside from the point of view of the incoming shower, see Fig. 3.5). The PMT turn the photons into electrical signal which is read out and determines the energy of the incoming particles. Both sections have active material equivalent to one nuclear interaction length which corresponds to 27.8 radiation lengths for the electromagnetic and 29.4 radiation lengths for the hadronic part. The energy resolution is following:

$$\frac{\sigma_{em}(E)}{E} = \frac{7\%}{\sqrt{E[GeV]}} \oplus 1\% \qquad (3.5)$$

$$\frac{\sigma_{had}(E)}{E} = \frac{56\%}{\sqrt{E[GeV]}} \oplus 7\%. \qquad (3.6)$$
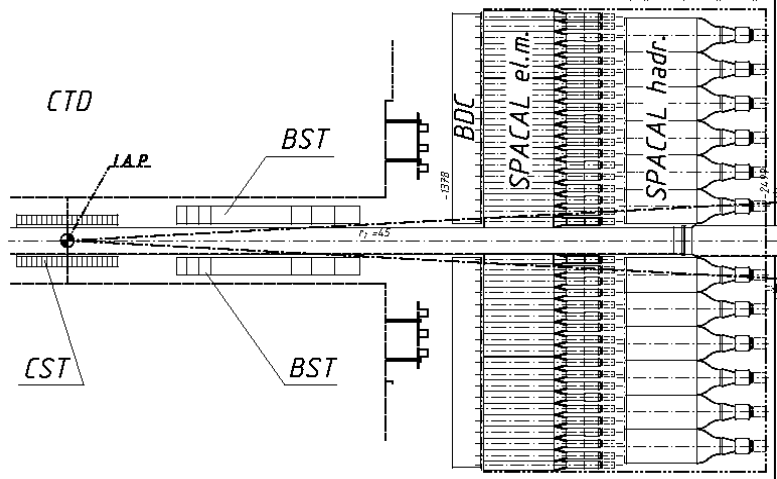
Figure 3.5: The side view of the positioning of the SpaCal calorimeter inside the H1 detector.

3.2.3 Luminosity System

The H1 luminosity system is designed to measure the luminosity delivered by HERA to the H1 detector. It is of crucial importance for measuring of cross sections of different processes. For the luminosity estimation delivered to the H1 detector the Bethe-Heitler process $ep \rightarrow ep\gamma$ with its cross section uncertainty 0.5% is measured. This process is very well known and calculable in the quantum electrodynamics. For the estimation, the electron tagger (ET), photon detector (PD) and the Cherenkov counter (VC) are used. The ET and PD are situated close to the beam and distant from the main detector since the scattering angles of the electron and photon are very small ($0 - 5$ $mrad$ for the electron and $0 - 0.45$ $mrad$ for the photon). The VC is used for veto condition. The ET is placed at the distance of $z = -33.4$ m and the PD at $z = -102.9$ m (See Fig. 3.6). The main source for the background is the bremsstrahlung from beam electrons interacting with gas molecules in the beam pipe. Dedicated, so called pilot bunches, are present in the electron beam and serve for the estimation of the beam-gas interaction rate. The number of events with statistical subtraction of the background effects N' is used for luminosity L estimation:

$$L = \frac{N'}{\sigma_{Bethe-Heitler}^{visible}} \qquad (3.7)$$

where $\sigma_{Bethe-Heitler}^{visible}$ is cross section corrected for the trigger efficiency and acceptance of the sub-detectors. The precision of the luminosity measurement

Figure 3.6: The H1 luminosity system.

for the HERA-II period is about 3.5%.

3.2.4   Trigger System

Since the beam bunches collide every 96 ns, it is not possible to store all the gathered information. A decision system has been developed in order to separate the events which are interesting from the physics point of view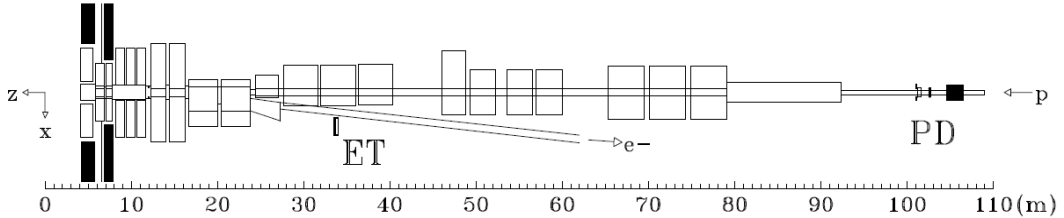. The input rate of events is at 10.4 MHz, but the tape-writing has a maximum at a rate of 10 Hz. The readout of the detector involves also dead-time, which is time necessary for the detector to recover from data taking of an event. Therefore it is essentially to store only interesting *ep* events. The trigger system is divided into four levels (L1-L4) which are called a "pipeline". The increasing level of trigger corresponds to more complex algorithms, after passing through the physics L4 trigger the event is written on the DST tape.

The central trigger control (CTC) gathers the L1 information from many sub-detectors in the form of L1 trigger elements (TE). There are 256 TE in total, the 128 $sub-triggers$ used in the analyses are logical combinations of the trigger elements. The sub-triggers contain in general conditions from all level triggers. The CTC analyses each of the STs and registers and L1KEEP signal "true" or "false" depending on the outcome. Each sub-detector has to store its data in a buffer every bunch crossing, since the CTC must register the L1KEEP signal. The length of the buffer limits the length of processing time for an event to 2.3 μs. If L1KEEP = "true", the readout and dead time begins. The L1 trigger reduces the event rate from 10.4 MHz to 1 kHz. Some sub-triggers can have rather high keep-rates and may prevail the other sub-trigger rates dedicated to less proba-ble processes, though not less interesting. That is why so called prescale factors (prescales) need to be applied to some sub-triggers in order not to occupy the bandwidth. Prescale of 2 for a particular sub-trigger means that only half of the events will be set the L1 keep" signal.

The information gathered from the sub-detectors for the L2 trigger is more detailed. The rough tracks are reconstructed by the tracker, calorimeter TEs are produced by LAr and SpaCal. The decision is based on pre-programmed topologies, the neural networks are used to produce the L2 TEs. The decision time is $\sim 20~\mu s$, if the even is to be stored at the L2 level, roughly 27000 channels of the H1 detector have to be read out. At the end of the L2 phase, the event rate is reduced to 200 Hz.

The L3 trigger level has been active since 2006. It uses the Fast Track Trigger and other sub-detector components to search for exclusive final states and it verifies L1 and L2 decisions. It decides within $100~\mu s$ and reduces the event rate to 50 Hz.

The final or the physics trigger performs the full classification of the event. Non-ep events apart from 1% used for monitoring purposes are rejected. Once all the necessary information from the sub-detectors is gathered, the dead-time ends and the pipelines are restarted. The full events are written with rate 5-10 Hz to the POTs (Production Output Tapes) which contain raw and reconstructed information and DSTs (Data Summary Tapes) with reconstructed information only.

3.2.5 Data Formats

The DSTs are the basic format with which all the analyses start. Since the access to these DSTs requires reading in and out from the tapes, other data formats stored directly on hard drives have been developed. The information on the DSTs is stored in so called banks - data objects with four-letter labels filled with data logically gathered together, for example the bank "DTRA" contains information about reconstructed tracks, etc. The Object Data Store (ODS) format is a copy of the DSTs with structure added in order to be easily processed by the H1 Object Oriented Software (H1OO) [38]. The micro ODS (μODS) data format corresponds to a H1OO structure which enables an easy access to physics objects, the H1 Analysis Tag (HAT) format stores the basic kinematic variables for each event. This analysis usually performed on the μODS and HAT level within the H1OO framework.

Chapter 4

Detection of Diffraction at HERA

In this chapter two basic approaches to selection of diffractive processes in the H1 collaboration are presented, the Large Rapidity Gap (LRG) method and the direct leading proton tagging method with the description of the Forward Proton Spectrometer (FPS) and the relevant triggers.

4.1 Large Rapidity Gap

Large Rapidity Gap (LRG) selection of diffractive events is based on the fact, that there is no colour string spanned between the system X and the outgoing proton in the interaction $ep \rightarrow e'Xp'$. This fact results in suppression of the activity in the forward parts of the detector. The variable η_{MAX} is defined as the most forward cluster in the calorimeter with energy deposit about the noise level (400 MeV or 800 MeV).

The Fig. 4.1 presents the first H1 measurement [39] representing the necessity of taking into account the diffractive processes in DIS. The DIS Monte Carlo `LEPTO` is not able to describe the η_{MAX} distribution in the region of low η_{MAX}. The events with large gap in rapidity between the most forward particle of the system X and the outgoing proton are mostly diffractive events. This observation results to a selection criteria for the diffractive events: η_{MAX} cut in combination with the forward muon (FMD), proton remnant tagger (PRT) and Forward Tagging System (FTS) used as veto-detectors.

Due to the limited acceptance of the forward detectors, which are part of the H1 main detector, the proton or its low mass excitations escape through the beam-pipe. Therefore the admixture of proton dissociation is present in the measurement preformed with the LRG method. The mass of the system Y which escapes the detection by the forward detectors is $M_Y < 1.6\ GeV$.

The advantage of the LRG method is in its high statistics.
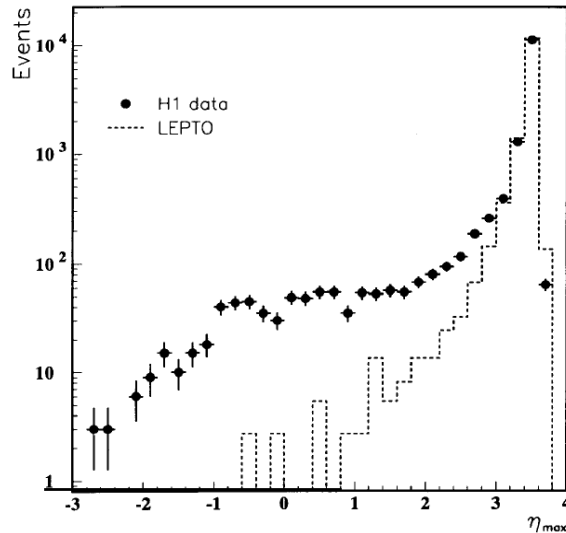
Figure 4.1: The η_{MAX} distribution for neutral current DIS events at HERA.

4.2 Tagging of Leading Proton

The second commonly used method for selecting diffractive events is based on detection of the outgoing scattered proton. The leading proton is scattered under very small angles ($< 15 \ mrad$), the instrumentation dedicated to measure its kinematic properties cannot be part of the main H1 detector. The tagging of the leading proton uses the technology of 'roman pots' (RP). This technology allows to insert detectors into the beam-pipe while preserving vacuum in it. The acceptance of the detectors is limited, since they cannot approach the beam to an arbitrary close distance. On the other hand, the measurements which use tagged protons are free of proton dissociation. Two independent proton taggers were installed at H1, the Forward Proton Spectrometer (FPS) and the Very Forward Proton Spectrometer (VFPS).

This analysis was performed using the data collected with the FPS detector.

4.3 Forward Proton Spectrometer

4.3.1 Detector Design

The magnetic optical system of HERA bending up to the distance of $z < 120 \ m$ is characteristic by presence of dipoles and quadrupole magnets only. The move-

Figure 4.2: The position of the FPS horizontal (H) and vertical (V) stations. The positive z-axis goes in the direction of the outgoing proton.

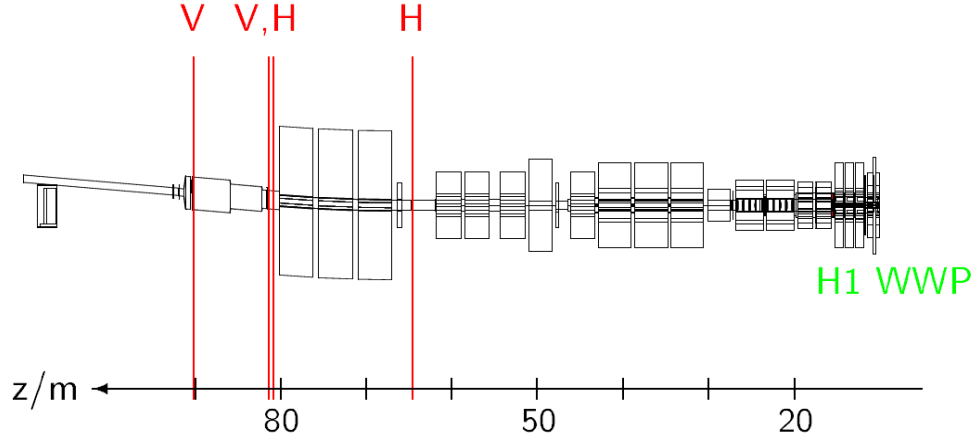ment of the protons is therefore in the first approximation considered as independent in the x and y axis. This allows an independent measurement of the x and y component of the scattered proton momentum. The magnetic optical system between the FPS and the H1 detector is used as spectrometer. The FPS detector consists of two sub-detectors which differ in kinematical acceptance. The horizontal stations are placed in the position $z = +63\ m$ and $z = +80\ m$ and cover the energy range $820\ GeV\ <\ E'_p\ <\ 920\ GeV$. The vertical stations are positioned at $z = +81\ m$ and $z = +90\ m$ and are able to measure in the energy range $550\ GeV\ <\ E'_p\ <\ 820\ GeV$. For the analysis only the horizontal stations have been used. The schematic picture of the FPS stations is presented in the Fig 4.2.

The description of the vertical stations is identical to the horizontal ones. Each station has two spectrometers with two identical sub-detectors separated by 60 mm. The sub-detectors are about 6 cm distant along the beam axis and are bound together and fastened to the same detector carrier. During the operating period, when the beam conditions reached a stable level, the carrier moved the sub-detectors towards the beam up to the distance of 2 - 3 cm. In case of emergency, the sub-detectors were moved into the parking position automatically. The distance between the sub-detector is sufficient to reconstruct not only the x and y coordinate of the momentum of the incoming proton but the polar angle as well. Tracks reconstructed with one subetector are called *local* tracks, the combination of both sets of local tracks gives a *global* track.
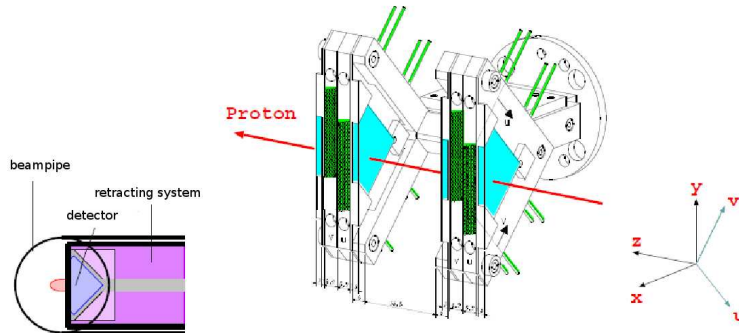
Figure 4.3: Position (left) and detailed description (middle) of the horizontal station of the FPS detector. The scintillating fibres are coloured light green, the trigger tiles cyan. The coordinate system with the positive z-axis pointing into the direction of the outgoing proton, the $x - y$ and $U - V$ coordinates (right).

Each sub-detector consists of two planes inclined by ± 45 with respect to the vertical pot axis. The local coordinate system of the FPS has projections in $U - V$ directions with the 45 degrees rotation described above (see Fig. 4.3). Each coordinate plane consists of five layers of 48 fibers in the horizontal stations and 20 fibers in the vertical stations, respectively. Each fiber has a diameter of 1 mm and is positioned parallel within the layers with a pitch of 1.05 mm in order to improve the reconstruction of the polar angle of the track. The trigger tiles are placed at the beginning and end of each sub-detector with respect to the movement of the scattered proton. The signal from these scintillator tiles is the basic condition for the FPS sub-trigger s112 which described in Sec. 4.5. The fibers belonging to a read out plane are attached to a 124 pixel position sensitive photo multiplier (PSPM). The large number of channels of this device allows to couple each fiber separately to one PSPM channel. For a leading proton which passes through both FPS stations, the average overall track reconstruction efficiency is 48%.

A more detailed description of the FPS detector can be found in [15] .

4.3.2   FPS Calibration

The algorithm for momentum reconstruction [15] is based on the fact that there exists a one-to-one correspondence between the coordinates and slopes of trajectories at $z = +85$ m and energy and emission angle at the origin for the particles

40
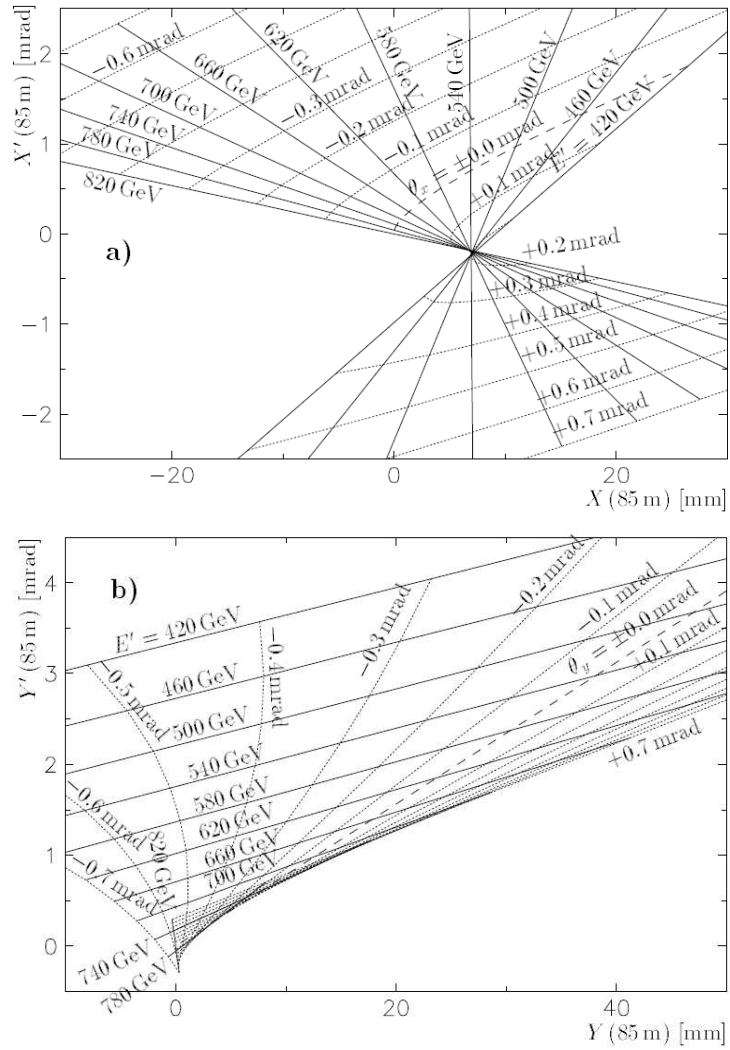
Figure 4.4: Dispersion at 85 m, displacements with respect to the nominal orbit (X,Y) versus the slopes (X',Y') in the horizontal (a) and vertical (b) plane for protons of different energies and emission angles.
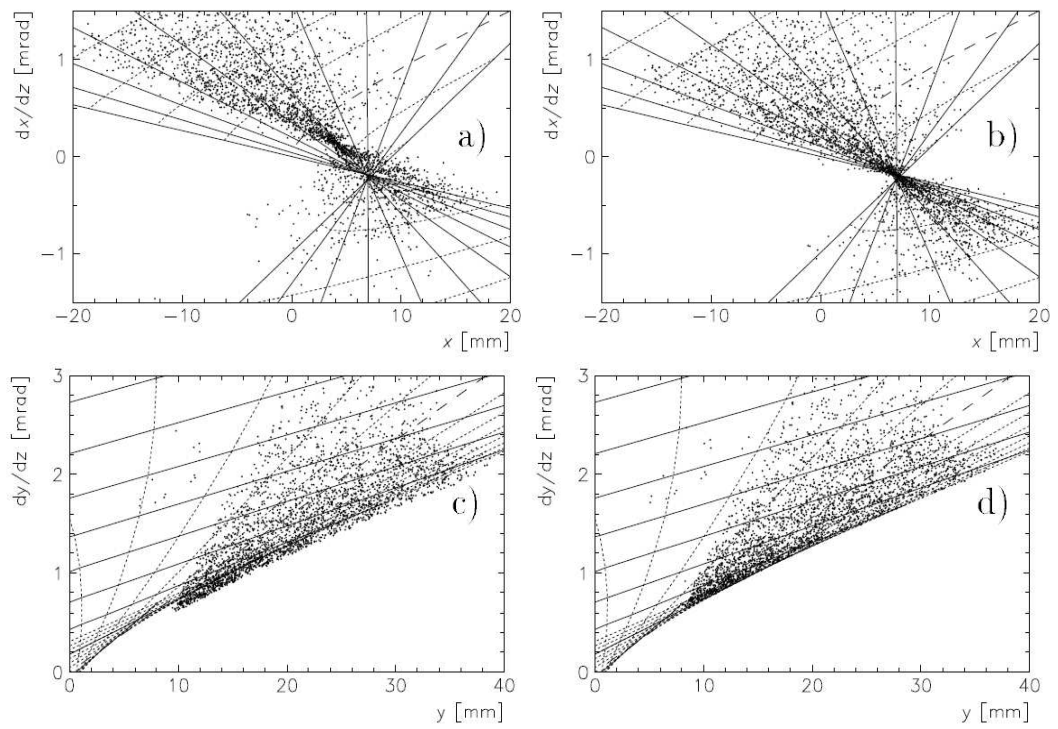
Figure 4.5: calibration of the beam positions and slopes in two coordinates. a)X vs X' assuming the nominal positions, b) X vs X' after fitting the horizontal beam position and slope, c)Y vs Y' assuming the nominal positions, d) Y vs Y' after X and Y calibration.

originating from the interaction point. In Fig. 4.4, the displacement with respect to the nominal orbit for both coordinates (X for horizontal and Y for vertical) versus the slope measured at $z = +85\,m$ for trajectories starting at the interaction point is plotted.

The fact that all trajectories meet in one point in (X,X') plane and that there are forbidden regions in this plane for particles originating from the interaction point is used for the calibration. Taking advantage of the dispersion in two planes enables two independent measurements of longitudinal particle momenta, which have to agree within the errors for genuine protons from ep interactions. This constraint is used in rejecting background tracks and improving on the momentum resolution. The Fig. 4.4 shows also that there are areas with densely packed trajectories which lead to a correspondingly bad momentum resolution.

All coordinates and slopes have to be measured with respect to the circulating beam in order to reconstruct longitudinal momenta. The absolute position of the HERA beam position monitors with respect to the H1 coordinate system is not known to better than $1\,mm$. Therefore a calibration method has been invented which uses only data measured by the Roman Pots. Starting from the nominal positions of the detector elements known from construction and from a survey in the HERA tunnel with respect to reference magnets of the proton machine, proton momenta and emission angles are reconstructed by applying the known beam optics transfer matrices of the spectrometer. The first order values are then corrected for the actual beam position. The results of the position and slope measurements before and after adjusting are shown in the Fig. 4.5. The vertical position and slope fulfil an additional constraint that the energy difference as reconstructed in the horizontal and vertical measurement has to be minimal.

With this procedure, run dependent calibration constants are calculated. The look up tables which relate measured trajectory positions and slopes at $z = +85\,m$ to energies and emission angles at the interaction point are established.

In addition, the diffractive photoproduction of ρ-mesons [16], where the final state is completely measured in the central detector and the FPS, offers an independent method to check the energy scale.

4.3.3 Detector Acceptance

The proton variables are reconstructed with the FPS information, the kinematics at the interaction point is then obtained with knowledge of the magnetic optical system properties as described above. The kinematical acceptance of the FPS detector during the HERA-II running period is [18]:
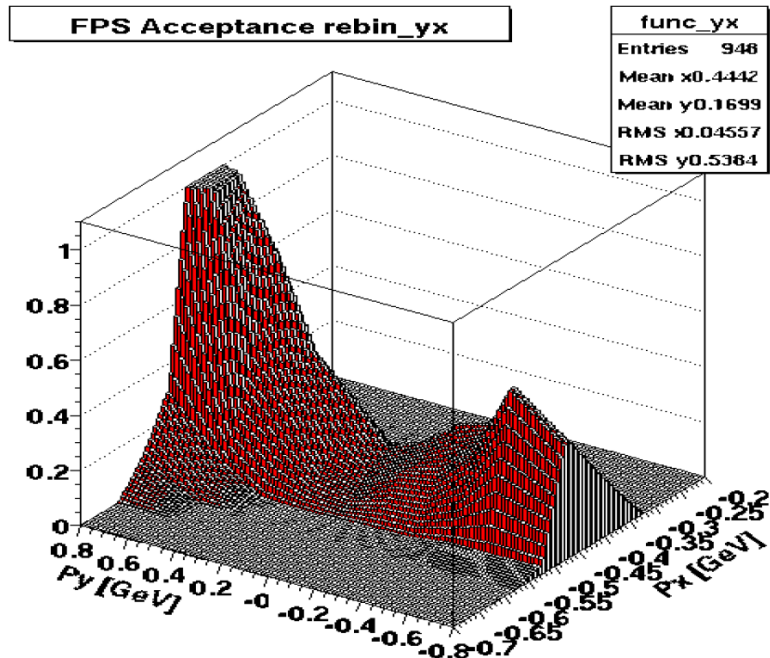
$$820\ GeV < E'_p < 920\ GeV \tag{4.1}$$

Figure 4.6: The FPS acceptance as a two dimensional function of p'_X and p'_Y.

$$-0.63 \ GeV < p'_X < -0.27 \ GeV \qquad (4.2)$$
$$-0.8 \ GeV < p'_Y < 0.8 \ GeV \qquad (4.3)$$

The acceptance defined as probability of reconstructing the proton with given kinematical quantities E'_p, p'_X, p'_Y at the interaction point within the same E'_p, p'_X, p'_Y bin in FPS is presented in the Fig 4.6. The simulation using the description of the HERA optics between the H1 main detector and FPS has been performed for four running periods in years 2005-2007. In a very narrow peak at $p'_X \sim -0.45 \ GeV$ and for highest values of p'_Y the acceptance reaches 100%. Fig. 4.7 presents the acceptance as a one dimensional function of the proton kinematical variables for different running periods. The maximal values lie between 35% and 45%, exceptionally at 70% for the p'_Y distribution. The highest acceptance was achieved in the running period $06e^-$.

The FPS acceptance as a function of E'_p, p'_X, p'_Y has been implemented in the object-oriented computing environment H1OO. It is used as an event-weight for the events simulated in Monte Carlo in order to obtain realistic spectra of the kinematic variables as measured by the FPS detector.

Further details of the analysis of the FPS resolution and scale uncertainties
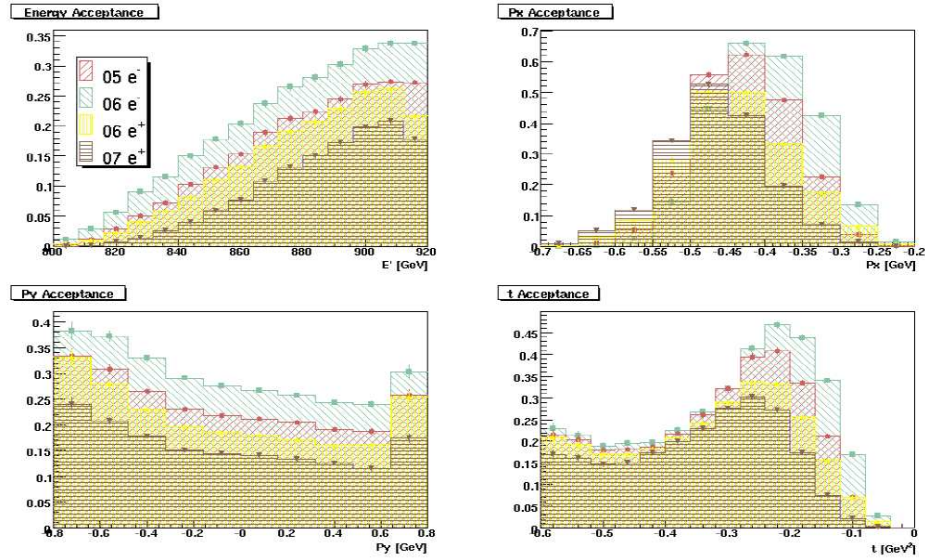
44

Figure 4.7: The FPS acceptance as one dimensional function of E'_p, p'_X, p'_Y and square of the four momenta transferred at the proton vertex t. Four colours correspond to four different running periods in years 2005 and 2006 with electrons and 2006 and 2007 with positrons.

can be found in [17].

4.4 Track Reconstruction Efficiency

The signals of all PSPM channels are classified into hit, noise, or cross talk signals before the track reconstruction. A filter algorithm is applied in order to reduce the influence of cross talk on the track reconstruction. A signal is accepted as a hit with an amplitude above an amplitude threshold of a PSPM channel.

First step of the track reconstruction is clustering of the fiber hits in the coordinate detector. Hits in at least two layers are requested for each cluster. Each FPS station consists of two identical sub-detectors, each cluster in the first detector is combined with each cluster in the second detector to obtain a track projection. Forward going protons are selected according to slopes of the projections. A spatial track is a combination of two projections, each having at least 5 out of 10 layers. At this point the track points have to be corrected for the detector positions, then global tracks are formed by spatial tracks inside the sensitive detector area for each of the FPS horizontal and vertical stations. The slopes of the global tracks are measured with an accuracy of a few μrad due to the large
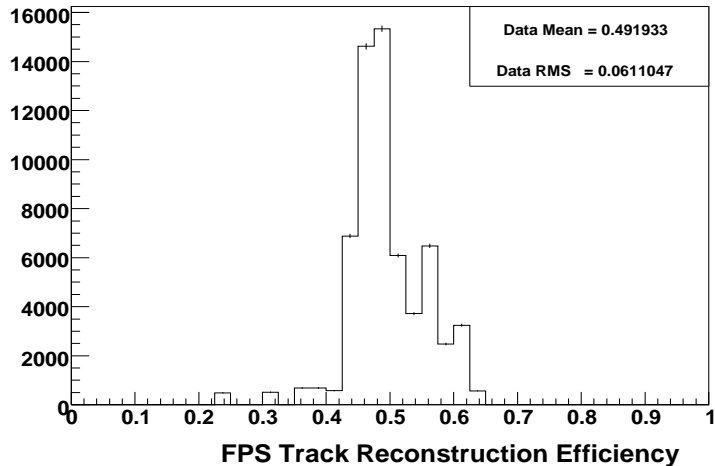
Figure 4.8: The FPS track reconstruction efficiency in the electron running period of the year 2006.

distance between two FPS stations.

The layer efficiencies vary in the horizontal FPS stations between 30% and 70% with an average value of $\sim 50\%$. As an illustration, the track reconstruction efficiency for the electron running period of the year 2006 is presented in Fig. 4.8.

Further details of the estimation of the FPS track reconstruction efficiency can be found in [15].

4.5 FPS Sub-trigger

The sub-trigger used for triggering the diffractive deep inelastic scattering events was split into two independent parts for the whole HERA II period:

$$s112 = FPS \ \&\& \ SPACAL \tag{4.4}$$

The SpaCal part is defined as

$$SPACAL = SPCLe\_IET > 1 \ || \ SPCLe\_IET\_Cen\_2 \tag{4.5}$$

and it sub-trigger requires a very soft condition on the signal in the electro-magnetic part of the SpaCal calorimeter. The efficiency is close to 100% and is presented in the Fig 4.9. Regions of the SpaCal calorimeter with low reconstruc-

tion efficiency have been excluded by additional box cuts applied in the data and the Monte Carlo selection as well (see Fig. 4.9 d)).

$$FPS = FPS\_HOR \ || \ FPS\_VER, \qquad (4.6)$$

the horizontal part consists of two trigger elements TE164 and TE165, which correspond to the 63 m and 80 m horizontal FPS stations. These two TEs are combined with a logical AND. Same strategy is valid for the vertical stations.

Each of the trigger elements requires signal from three out of four trigger tiles, every tile signal is formed by an OR condition from two photomultipliers. For efficiency studies events accepted by sub-triggers independent on FPS trigger elements were used. To exclude beam halo fake events, the proton had to be reconstructed by the FPS fiber detector which is independent on the trigger tiles. With 90% efficiency of one PMT, the theoretical efficiency of the combination of the probabilities is 99.94%. In the study [18], the efficiency of this part of the sub-trigger was estimated to be constant and above 99%. Run-ranges, where the trigger elements were not working correctly were excluded from the run selection.

The total efficiency of the sub-trigger s112 is constant and above 98 %.

When taking data with an active sub-trigger, its prescale has to be taken into account (see Sec. 3.2.4). The prescale of the sub-trigger s112 has been applied on the measured data as event-weight. The averaged value over the running period is 1.05, the particular values did not exceed the value of 4.
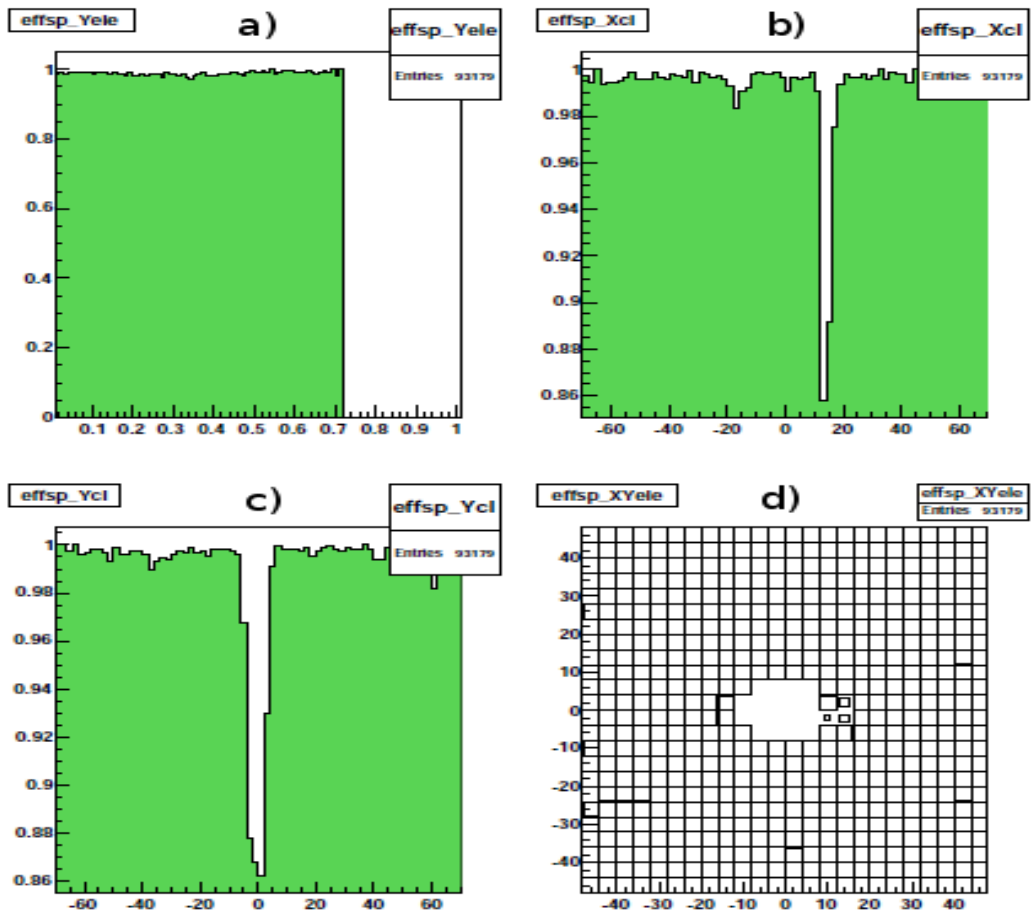
Figure 4.9: The SpaCal part of the s112 sub-trigger efficiency as a function of y (a), the efficiency in terms of SpaCal scattered electron cluster X (b)(resp Y (c)) position, d) the two dimensional $X - Y$ plane of the SpaCal calorimeter.

Chapter 5

Monte Carlo Models and QCD Predictions

Monte Carlo (MC) generators became an important part of any high energy physics analysis. MC generators are used to generate physics events by using of relevant matrix elements, usually at leading order of α_s. Phenomenological models implementing fragmentation of partons into observable colour singlet hadrons (hadronisation) are part of the generators as well. Therefore, the MC generators can be easily used not only to predict generator or parton level cross sections, but also as input for detector simulations. Once a good detector simulation is provided, the MC can be used for estimation of corrections from detector level to the level of stable hadrons.

The measured cross sections are compared to the next-to-leading (NLO) QCD calculations. The NLO predictions are calculated at the level of partons, hadronisation corrections δ_{had} need to be applied in order to obtain the level of stable hadrons. Since the MC contains full information about all levels of simulation, it is used for extraction of δ_{had} as well.

In this analysis, Monte Carlo models were used for obtaining the correction factors from detector to hadron level, hadronisation corrections and for comparison of unfolded data with generator level cross section predictions.

5.1   Monte Carlo Models

This section will briefly describe the MC models used in this analysis.

The general sketch of space-time picture of a deep inelastic ep collision as implemented in standard MC generators is presented in Fig. 5.1. Parton emerging from proton undergoes initial state QCD radiation, then the hard process calculable in perturbative QCD follows. The final state QCD radiation takes place
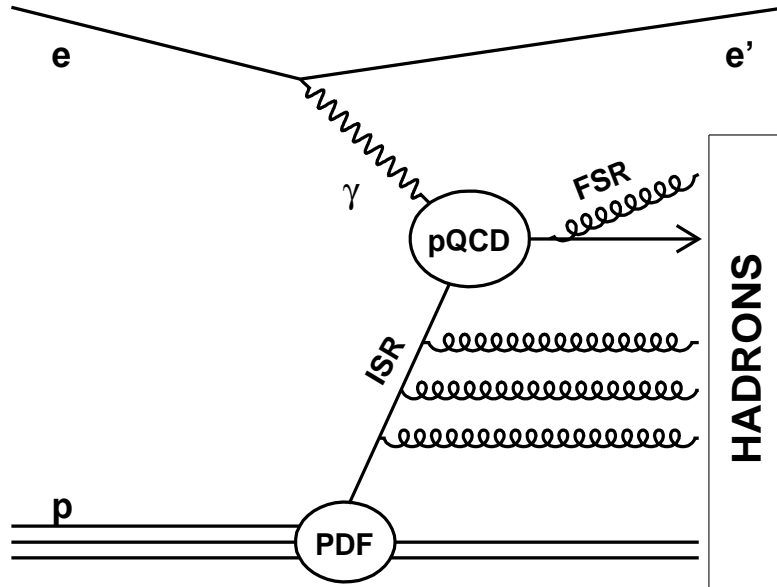
Figure 5.1: Space-time picture of DIS.

after the hard interaction, all produced partons hadronise then to the observable colour singlet hadrons.

5.1.1 `RAPGAP` Monte Carlo

In this analysis the signal events are generated with the `RAPGAP 3.1` Monte Carlo generator [50] using the H1 2006 Fit B DPDF [19] for $I\!P$ and $I\!R$ exchange with an intact (elastic) leading proton. The generated processes include (see Fig. 5.2): leading-order quark-parton model (QPM), boson-gluon fusion (BGF) and QCD Compton (QCD-C) with light quark flavours (u,d,s) and charm quark. The generation of files of events with the light quarks and the charm is done separately. Higher order QCD effects are mimicked by using running strong coupling constant α_s and by initial and final state QCD radiation. The hadronisation is performed by Lund string fragmentation model [28] as implemented in Jetset [51]. The signal samples are generated at $\sqrt{s} \sim 319 \; GeV$ with following kinematical constraints:

$$
\begin{aligned}
2 \; GeV^2 \quad &< \quad Q^2 < 1000 \; GeV^2 & (5.1) \\
0.001 \quad &< \quad y < 0.9 & (5.2) \\
x_{I\!P} \quad &< \quad 0.15 & (5.3)
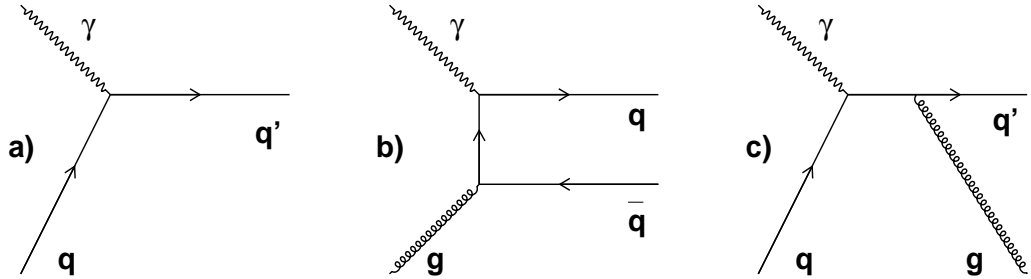\end{aligned}
$$

50

Figure 5.2: Sub-processes generated with `RAPGAP`: a) QPM, b) BGF, c) QCDC

$$(5.4)$$

During the generation, the different sub-processes are combined into one file by taking into account corresponding cross sections (see following table).

sub-process	$\sigma(I\!\!P)$	$\sigma(I\!\!R)$	$\sigma(I\!\!P)$
QPM	58964 pb	22237 pb	0 pb
BGF uds	1538 pb	285 pb	0 pb
BGF charm	0 pb	0 pb	6039 pb
QCDC	544 pb	252 pb	0 pb

The first column corresponds to sample called "$I\!\!P$ uds", the second to "$I\!\!R$ uds" and the last to "$I\!\!P$ $charm$". It combines the elastic pomeron (reggeon) exchange with the mixture of sub-processes as described above. In addition, QED radiation of the interacting lepton have been switch on in order to reproduce the real detector level data. The final estimated cross sections are corrected for the QED radiation effects. This is done with the help of the ratio of cross sections at the hadron level of radiative and non-radiative `RAPGAP`. The non-radiative sample is generated with the same parameters as the radiative one except for switching off the QED radiation effects.

The combination of the three Monte Carlo samples with QED radiation has been used for the estimation of the detector level corrections, the analogous samples without the QED effects were generated in order to estimate the QED radiative corrections.

The resolved pomeron model `RAPGAP` Monte Carlo was used for unfolding of the data from the detector to hadron level, it was therefore generated and simulated with the GEANT3 program [56] in all running periods.

51

The signal Monte Carlo is generated with QCD parton showering based on the leading log DGLAP splitting functions in leading order of the strong coupling constant α_s (LLPS). For estimation of hadronisation corrections, a `RAPGAP` MC sample has been generated with QCD parton showers modelled with the colour dipole model (CDM) as implemented in `ARIADNE` [52].

For the comparison of the measured data to the direct pomeron model [53] (see Sec. 2.2.5 for more details), the `RAPGAP` Monte Carlo generator can be used. Two processes with $q\bar{q}$ and $q\bar{q}g$ in the final state have been generated and combined taking into account corresponding cross sections $\sigma(q\bar{q}) = 192\ nb$ and $\sigma(q\bar{q}g) = 2616\ nb$. The used structure function of proton was CTEQ 6 LO fit with NLO α_s [54] and of photon SaS-G 2D (ver.2) LO [55].

The direct pomeron model (denoted as $q\bar{q}$ and $q\bar{q}g$) was used only for the comparison of theoretical predictions of direct pomeron model to the data.

model	process	number of events	luminosity
resolved	$I\!\!P$ uds	$6 \cdot 10^6$	$274.7\ pb^{-1}$
pomeron	$I\!\!R$ uds	$2 \cdot 10^6$	$368.3\ pb^{-1}$
	$I\!\!P$ charm	$3 \cdot 10^6$	$834.2\ pb^{-1}$
direct	$q\bar{q}$	$1 \cdot 10^6$	$5208.4\ pb^{-1}$
pomeron	$q\bar{q}g$	$1 \cdot 10^6$	$382.22\ pb^{-1}$

For the study of background in the acceptance range of the Forward Proton Spectrometer the `RAPGAP` program is used in the inclusive non-diffractive mode and in the mode which is represented by the process of proton dissociation combined with the elastic pomeron and reggeon exchange.

process	number of events	luminosity
Non-Diffractive	$8 \cdot 10^6$	$40\ pb^{-1}$
Proton Dissociation $I\!\!P$ uds	$2 \cdot 10^5$	$17\ pb^{-1}$
Proton Dissociation $I\!\!R$ uds	$2 \cdot 10^5$	$4.5\ pb^{-1}$
Proton Dissociation $I\!\!P$ charm	$2 \cdot 10^5$	$31\ pb^{-1}$

5.1.2 `LEPTO` + `SCI` Monte Carlo

In order to compare our results with the Soft Colour Interaction model (see Sec. 2.2.6), the Monte Carlo generator `LEPTO` [57] has been used. It is a general and flexible MC for simulation of complete lepton-nucleon scattering events. It is based on the leading order electroweak cross sections for the underlying parton level scattering processes, but with main emphasis on the hadronic part of the event. The hadronisation process is performed with the Lund string hadronisation model [28].

In order to describe the total cross section of the diffractive dijet measurement, the probability of having `SCI` parameter has been set to $P = 0.3$. The long colour strings have been suppressed according to the generalised area law (See Sec. 2.2.6). This MC sample will be denoted as "`SCI`". The generated `SCI + GAL` MC has been used only for comparison of theoretical predictions to the data.

process	number of events	luminosity
`SCI + GAL`	$1 \cdot 10^7$	$52.88\ pb^{-1}$

5.2   Next-to-leading Order Predictions

The renormalisation scale in the diffractive dijet events tends to be rather low ($\sim 25\ GeV^2$ for p_T^2 as a scale). As a result the corresponding value of α_s is so large, that higher order $\mathcal{O}(\alpha_s^2)$ contributions cannot be neglected. In fact it turns out, that for diffractive dijet production in DIS, the second order contributions are larger than the leading order contributions.

The diffractive dijet cross sections have been calculated at the next-to-leading order level with the factorisation and renormalisation scale set to $\mu_r^2 = \mu_f^2 = Q^2+ < p_T^* >^2$, where $< p_T^* >$ is the mean transverse momentum of the two hard partons in the process in the $\gamma^* p$ rest frame. Due to the finite order of the calculation, the computed cross sections are dependent on the chosen scale. Therefore the theoretical uncertainties caused by choice of the scale are usually estimated by means of varying the scale by $\mu_{up}^2 = 4\mu^2$ and $\mu_{down}^2 = \mu^2/4$.

5.3   `nlojet++`

`Nlojet++` 4.1.0 [60] is a program for calculating leading and next-to-leading order cross sections in non-diffractive DIS. It is written in the C++ language by Zoltan Nagy. The Catani-Seymour subtraction [61] is used to calculate the matrix elements. The program calculates cross section for e^+e^-, ep and pp interactions. The core program remains untouched by the user, while calling a user-defined function has to be attached:

```
nlojet++ --calculate -c full -u user_routine.cc,
```

where the option c specifies the order of the calculation: LO, NLO, NLO+LO.

5.3.1   Adjustment of `nlojet++` for Diffraction

In the user defined routine *dijets.cc*, all specific settings and the jet selection is done. In order to implement the diffractive DIS scattering, the theoretical

assumption of QCD and Regge factorisation is applied. The interaction is changed from ep scattering to $e\mathbb{P}$ scattering by scaling the initial proton four vector by the factor $x_{\mathbb{P}}$. The diffractive Ansatz in form of Eqn. 2.30 is used for every $x_{\mathbb{P}}$ bin. Since the cross section is rising with $x_{\mathbb{P}}$, in order to achieve a true description, $x_{\mathbb{P}}$ slicing has to be introduced. The cross section is calculated in small intervals $dx_{\mathbb{P}}$ with central value $x_{\mathbb{P}}$ and then summed over all the slices. The diffractive PDF fits "H1 2006 Fit B" and "H1 2007 Jets" are used in the calculations with fixed flavour number scheme (FFNS) with $n_f = 4$ and the value of $\lambda_{QCD}^{(3)} = 0.3395$, which corresponds to the world averaged values of α_s at the mass of the Z boson, $\alpha_s^{(5)}(M_Z^2) = 0.118$. For the comparison with the theory, both pomeron and reggeon contributions should be taken into account.

In order to use consistent k_T jet finding algorithm in the NLO QCD calculations as well as in the measurement of the data, $FastJet$ [65] algorithm has been implemented into `nlojet++`.

Chapter 6

Event Selection

In this chapter, the selection criteria applied on data and the Monte Carlo sample on the detector level, the reconstruction methods of the kinematical variables and the calibrations are described. The data have been selected within the years 2005 - 2007. The samples have been divided into five sub-periods according to stable FPS running conditions. Following table shows the sub-periods, its label and corresponding run-range:

period	label	run range
electron1 2005	05e1	403117-419022
electron2 2005	05e2	427446-436893
electron 2006	06e	444094-468529
positron 2006	06p	468632-492365
positron 2007	07p	493274-500611

At the end of the chapter, the control plots will be presented.

6.1   Selection of Good Runs

The list of selected runs from years 2005 - 2007 has been created with following conditions:

- All the sub-detectors described in chapters 3.2 and 4.3 have to operate under appropriate high voltage (HV) and work properly

- The information from all the sub-detectors has to be stored properly

- The level of noise on the sub-detectors must be under control

- Sub-trigger s112 is active (for definition, see Sec. 4.5)

run period	L_{int} $[pb^{-1}]$
05e1	25.99
05e2	23.79
06e	27.46
06p	52.70
07p	26.72

Table 6.1: Luminosities in five run periods as collected with the s112 sub-trigger.

The integrated luminosity selected in the five sub-periods of the FPS data taking period is presented in Table 6.1.

The total luminosity used in this analysis was $L_{2005-07} = 156.7$ pb^{-1}.

6.2   Reconstruction of kinematic Variables

The method of reconstruction of kinematic variables has to be chosen in the best possible way, because it is essential for the good reconstruction of DIS events. The two reconstruction methods and their combination are presented in the following sections.

Electron Method

The Electron method uses for the reconstruction of kinematic variables y and Q^2 from the scattered electron four vector only, i.e. it uses the information from the SpaCal calorimeter. The y and Q^2 are defined by:

$$y_{el} = 1 - \frac{E'_e}{E_e}(1 - \cos\theta_{el}) \tag{6.1}$$

$$Q^2_{el} = \frac{E'^2_e \sin^2\theta_{el}}{1 - y_{el}}, \tag{6.2}$$

where E_e is the electron beam energy of 27.5 GeV, the E'_e and θ_{el} are the scattered electron energy and the scattering angle.

Double Angle Method

The Double Angle method uses the combined information from the scattered electron and the hadronic final state. It uses the angle of the scattered electron and angle of the mass-less mathematical object defined in Figure 6.1.

With the help of the scattered electron and hadron variables, on can define the double angle quantities in the following way:
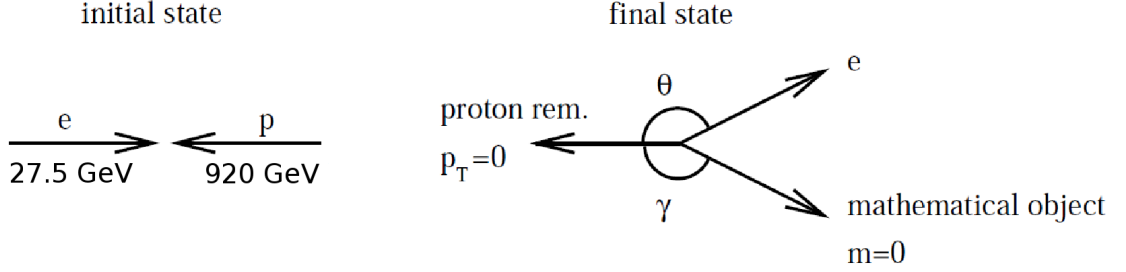
initial state
final state

Figure 6.1:

$$\cos\gamma = \frac{p_{Th}^2 - (E_h - p_{zh})^2}{p_{Th}^2 + (E_h - p_{zh})^2} \tag{6.3}$$

$$y_{da} = \frac{E_h - p_{zh}}{2E_e} \tag{6.4}$$

$$Q_{da}^2 = 4E^2 \left[\frac{\sin\gamma(1 + \cos\theta_{el})}{\sin\gamma + \sin\theta_{el} - \sin(\theta_{el} + \gamma)}\right] \tag{6.5}$$

y-Averaged Method

The y-Averaged method combines the information from both reconstruction methods described above. The y-Averaged method variables are defined as:

$$y_{av} = y_{el}^2 + y_{da}(1 - y_{da}) \tag{6.6}$$

$$Q_{av}^2 = 4E_e^2 \frac{1 - y_{av}}{\tan^2 \frac{\theta_{el}}{2}} \tag{6.7}$$

Comparison of Methods

The comparison of resolution of the variable y obtained with all three methods described above is presented in Fig. 6.2. In order to exhibit the different resolution of the reconstruction methods, the plots are binned in three ranges in y. It is seen that in the low y region ($y < 0.2$), the width of the fitted distribution clearly favours the y-averaged method. In the medium ($0.2 < y < 0.45$) and high ($0.45 < y < 0.7$) y region the electron method is slightly favoured. Due to the better resolution in low y and due to the fact, that the cross sections calculated with
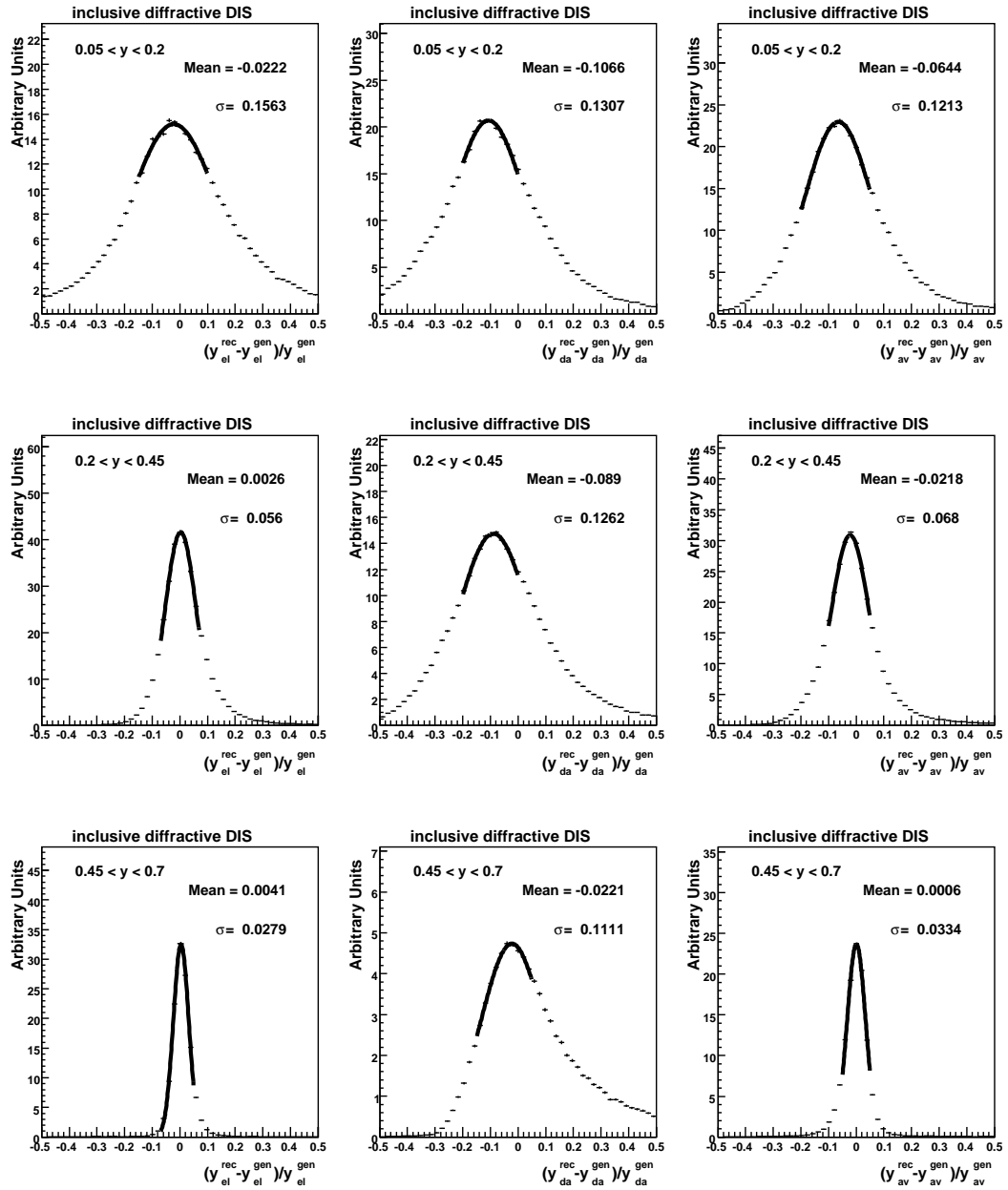
Figure 6.2: Comparison of y resolution for electron (left), double angle (middle) and y-Averaged (right) methods in three y bins.

kinematics reconstructed with the y-Averaged method are less sensitive to the QED radiative corrections, the y-Averaged method has been chosen as the most suitable for this analysis. From now on, the kinematic variables reconstructed with this method will be referred as y and Q^2.

6.3 Hadronic Calibration

For a measurement of jets with low transverse momenta, a precise calibration of the hadronic final state contained in the LAr calorimeter is of highest importance. Once the scattered electron is calibrated, it can be used as a reference for the calibration of the HFS. In this analysis, the Iterative Calibration by David Salek [63] as implemented in the $H1OO$ environment has been used.

The Iterative Calibration uses the transverse momentum balance between the scattered electron and the hadronic final state to improve the Monte Carlo description of the data in order to reduce the systematic error on the estimation of the hadronic final state energy in the absolute scale. For the estimation of the HFS energy scale uncertainty in the region of phase space of this analysis, a test of the Iterative calibration had to be performed. Due to the low statistics of the diffractive DIS jet sample, a special non-diffractive dedicated samples of data and `RAPGAP` Monte Carlo hve been used.

The selection of events in the sample dedicated to the testing of the calibration was defined as:

- Properly reconstructed vertex with z-coordinate within $\pm 35~cm$

- $10~GeV^2 < Q_e^2 < 100~GeV^2$

- $E'_e > 15~GeV$

- $156° < \theta_e < 175°$

- $0.01 < y < 0.7$

- Scattered Electron reconstructed in the SpaCal calorimeter

- $18~cm <$ radial distance of the cluster from the beam $< 75~cm$

- Electron Cluster Radius $< 4.5~cm$

- Fiducial Cuts to improve the Scattered Electron reconstruction

- $52~GeV < E - Pz > 70~GeV$

- $\#jets = 1$

- $p_{T,j} > 3\ GeV$

- $7° < \theta_j < 150°$

- Missing Transverse Energy $< 16\ GeV$

The p_T balance is defined as a ratio of the transverse momentum of the scattered electron to the transverse momentum of the hadronic final state. This ratio is close to unity for a compensated calorimeter. The p_T balance as a function of transverse momentum of the scattered electron and of the polar angle of the jet was studied. The mean value of the p_T balance distribution has been fitted with a gaussian function in each bin in $p_{T,e}$ and θ_j and then these mean values have been displayed as a function of $p_{T,e}$ and θ_j. In order to estimate the HFS energy uncertainty the double ratio

$$DR = \frac{< \frac{p_{T,had}}{p_{T,ele}} >_{data}}{< \frac{p_{T,had}}{p_{T,ele}} >_{MC}} \tag{6.8}$$

has been calculated. In the Figs. 6.3 and 6.4, the absolute mean values and the double ratios for the dedicated data and Monte Carlo `RAPGAP` samples are presented as a function of $p_{T,e}$ and θ_j. The errors were obtained from the uncertainties of the fit. The double ratio values lie within the 2% level for both electron transverse momentum and polar angle of the jet. Therefore we conclude, that the uncertainties of the HFS energy scale measurement are 2%.

6.4 Inclusive DIS Selection

In this section, the selection criteria for the inclusive diffractive DIS analysis will be described. The selection of good runs and the luminosity estimation has been described in Section 6.1 and it is considered as a part of the basic selection.

The requirement for the well reconstructed primary vertex is motivated by proper reconstruction of the tracks and it can be fulfilled with two conditions: 1) reconstructed vertex is labelled as "primary" by the vertex finder implemented in H1OO, 2) position of the vertex in the z-direction fulfils the criteria:

$$-35\ cm < Zvtx < 35\ cm \tag{6.9}$$

This cut reduces the background coming from beam-gas interactions significantly.
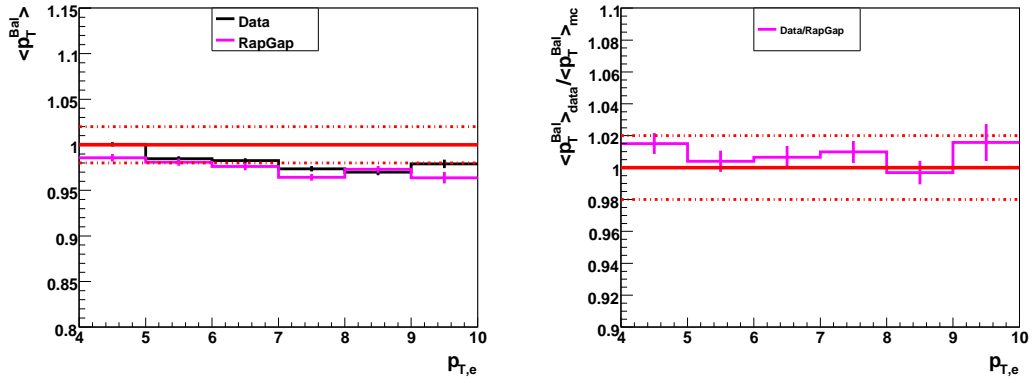
Figure 6.3: Mean p_T balance as a function of scattered electron transverse energy for data and `RAPGAP` MC (left), the double ratio, i.e. the ratio of mean p_T balance of data to Monte Carlo (right).
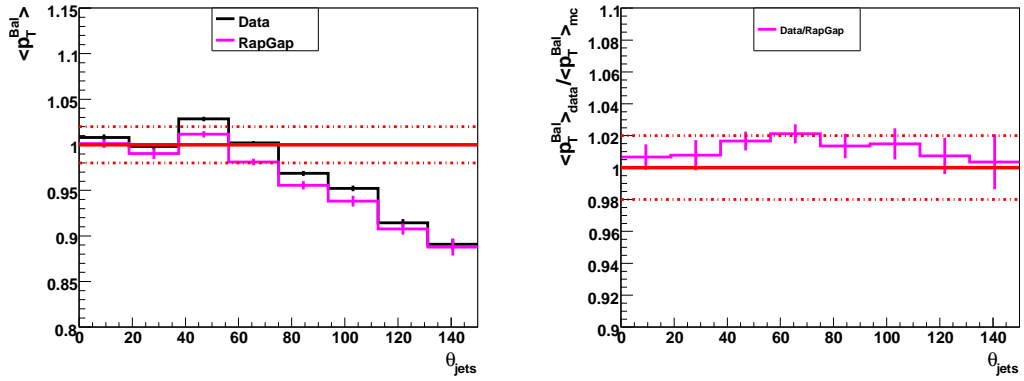

Figure 6.4: Mean p_T balance as a function of jet polar angle for data and `RAPGAP` MC (left), the double ratio, i.e. the ratio of mean p_T balance of data to Monte Carlo (right).

6.4.1 Scattered Electron

In order to ensure a correct scattered electron reconstruction, several cuts on the signal from the SpaCal calorimeter have to be applied. The electromagnetic shower in the calorimeter differs from a hadronic one by shape and size. In order to ensure the reconstruction of an electron shower, a cut on the cluster radius is applied:

$$r_{clus} < 4 \ cm. \tag{6.10}$$

The position of electron should be well contained in the range of SpaCal acceptance, therefore cuts on the radial distance of the scattered electron cluster from the beam:

$$13 \ cm < r_{SpaCal} < 75. \ cm \tag{6.11}$$

and on the squared four momentum transfer at the electron vertex

$$4 \ GeV^2 < Q^2 < 110 \ GeV^2 \tag{6.12}$$

are applied. In order to reduce the photoproduction (γp) background, the lower limit on the electron energy has been set to

$$E'_e > 10 \ GeV \tag{6.13}$$

and the inelasticity of the scattered electron has to lie within the range of

$$0.05 < y < 0.7. \tag{6.14}$$

The $E - Pz = E'_{ele} - p_{z,ele} + E_{HFS} - p_{z,HFS}$ variable commonly used for suppression of γp in DIS is restricted to

$$35 \ GeV < E - Pz < 70 \ GeV. \tag{6.15}$$

Additional cut to ensure consistency between the electron (e) and double angle (da) reconstruction method, y has to be in the range:

$$-0.3 < y_e - y_{da} < 0.3. \tag{6.16}$$

As described in Section 4.5, additional box cuts on in the $X - Y$ plane of the SpaCal detector have been applied in order to achieve almost 100% constant efficiency of the s112 sub-trigger. The Fig. 6.5 shows the distribution of the azimuthal angle ϕ of the scattered electron before and after applying the box cuts. After excluding the inefficient cells the description of the measured spectra by `RAPGAP` Monte Carlo becomes better.
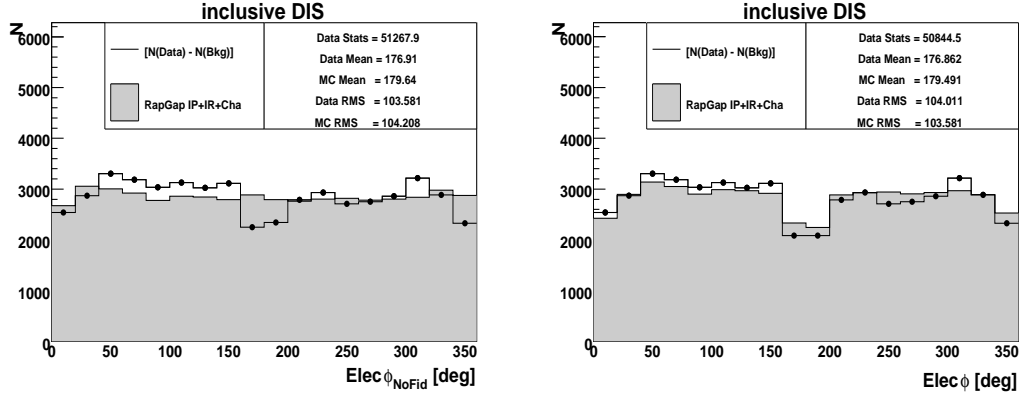
Figure 6.5: Distribution of the ϕ angle of the scattered electron measured in the SpaCal calorimeter before the exclusion of dead cells (left) and after the correction (right).

6.5 Jet Selection

In this section, the k_T jet algorithm will be described as well as the selection of the two jet topologies studied in this analysis.

6.5.1 FastJet Algorithm

The Fast Jet algorithm[65] as implemented in the H1OO environment is a optimisation of the k_T algorithm. The k_T jet algorithm is a infra-red and collinear safe algorithm and the jet finding procedure is following:

1. For each pair of particles i, j calculate the k_t distance $d_{ij} = min(k_{ti}^2, k_{tj}^2) \cdot R_{ij}^2$, where $R_{ij}^2 = (\eta_i = \eta_j)^2 + (\phi_i - \phi_j)^2$. The k_{ti}, η_i and ϕ_i are the transverse momentum, pseudorapidity and azimuthal angle of the particle i. For each particle also the distance to the beam has to be estimated $d_{iB} = k_{ti}^2$.

2. The minimum d_{min} of all the d_{ij}, d_{iB} has to be found. If $d_{min} = d_{ij}$, merge these two particles into a single one, summing their four momenta. If $d_{min} = d_{iB}$, declare the particle as a final jet.

3. Repeat this procedure until no unused particles are left.

63

6.5.2 Jet Topologies

The Fast Jet algorithm is applied on the hadronic final state which is boosted into the γp centre-of-mass (HCM) frame. The transverse momentum cuts are applied in the HCM frame, the pseudorapidity selection is applied in the laboratory frame in order to cover the acceptance of the LAr calorimeter in the most precise way. Two jet topologies have been selected (see Sec. 2.3): "2 central jets" and "1 central + 1 forward jet".

The "2 central jets" selection selects two hardest jets with following criteria:

$$p^*_{T,1} > 5 \ GeV \tag{6.17}$$
$$p^*_{T,2} > 4 \ GeV \tag{6.18}$$
$$-1 < \eta_{1,2} < 2.5, \tag{6.19}$$

where $p^*_{T,1(2)}$ means the transverse momentum of the hardest respectively second hardest jet found by the k_T algorithm in the HCM frame. The pseudorapidity range covers the central part of the H1 detector.

The topology, which will be referred as "1 central + 1 forward" is defined as:

$$p^*_{T,1} > 3.5 \ GeV \tag{6.20}$$
$$p^*_{T,2} > 3.5 \ GeV \tag{6.21}$$
$$-1 < \eta_1 < 2.5 \tag{6.22}$$
$$1 < \eta_2 < 2.8 \tag{6.23}$$
$$M_{12} > 12 \ GeV, \tag{6.24}$$

where index 1 means the central jet and index 2 means the jet going to the forward direction. These cuts are imposed in order to enhance the non-DGLAP phase space (see Sec. 2.3). Additional condition on η_{jets} ordering has been applied in order to obtain stable NLO QCD predictions, i.e.

$$\eta_2 > \eta_1. \tag{6.25}$$

In order to have the possibility to study the whole accessible pseudorapidity range, the cut on η_2 has been extended to the backward region

$$-0.6 < \eta_2 < 2.8 \tag{6.26}$$

6.6 Diffractive Selection

The diffractive selection is based on the tagging of the scattered proton in the FPS detector (see Sec. 4.3). In order to ensure correct reconstruction of the diffractive variables, acceptance cuts on the proton kinematic variables have to be applied and the background described in the Sec. 6.7 has to be subtracted. The FPS acceptance cuts are defined as:

$$E'_p > 820 \ GeV \tag{6.27}$$
$$-0.63 < p'_X < -0.27 \ GeV \tag{6.28}$$
$$-0.8 \ GeV < p'_Y < 0.8 \ GeV \tag{6.29}$$
$$x_{I\!P} < 0.1, \tag{6.30}$$

where the E'_p, p'_X, p'_Y stand for the scattered proton energy and X and Y momentum coordinate respectively. The $x_{I\!P}$ is the fractional longitudinal energy loss of the leading proton. The simulation of the FPS detector is not a part of the official Geant3 simulation of the whole H1 detector as it is implemented in the H1SIM [62] program.

The FPS acceptance function $FpsAcc(E'_p, p'_X, p'_Y)$ shown in Figs. 4.6 and 4.7 has been obtained by the simulation of passing of the scattered protons through the magnetic optical system between the FPS detector and the interaction point. For every event the FPS acceptance has been calculated using the proton kinematics and applied as a detector level event weight.

6.7 Background Treatment

The following section describes background subtraction from the data measured with the FPS detector.

6.7.1 Physics Background

In order to take into account only the processes with the scattered proton in the final state, other physics processes detectable in the FPS kinematical range have to be investigated. Events with standard deep-inelastic scattering in non-diffractive mode and events with proton dissociation have been generated with RAPGAP MC generator and simulated with H1SIM. These samples are normalised to the same luminosity.

The Fig. 6.6 a) presents the $x_{I\!P}$ distribution of inclusive diffractive DIS events ($I\!P \ uds$, see Sec. 5.1.1) in the FPS detector. In the Fig 6.6 b) the ratio of proton dissociation to diffractive DIS and in Fig. 6.6 c) the ratio of non-diffractive to
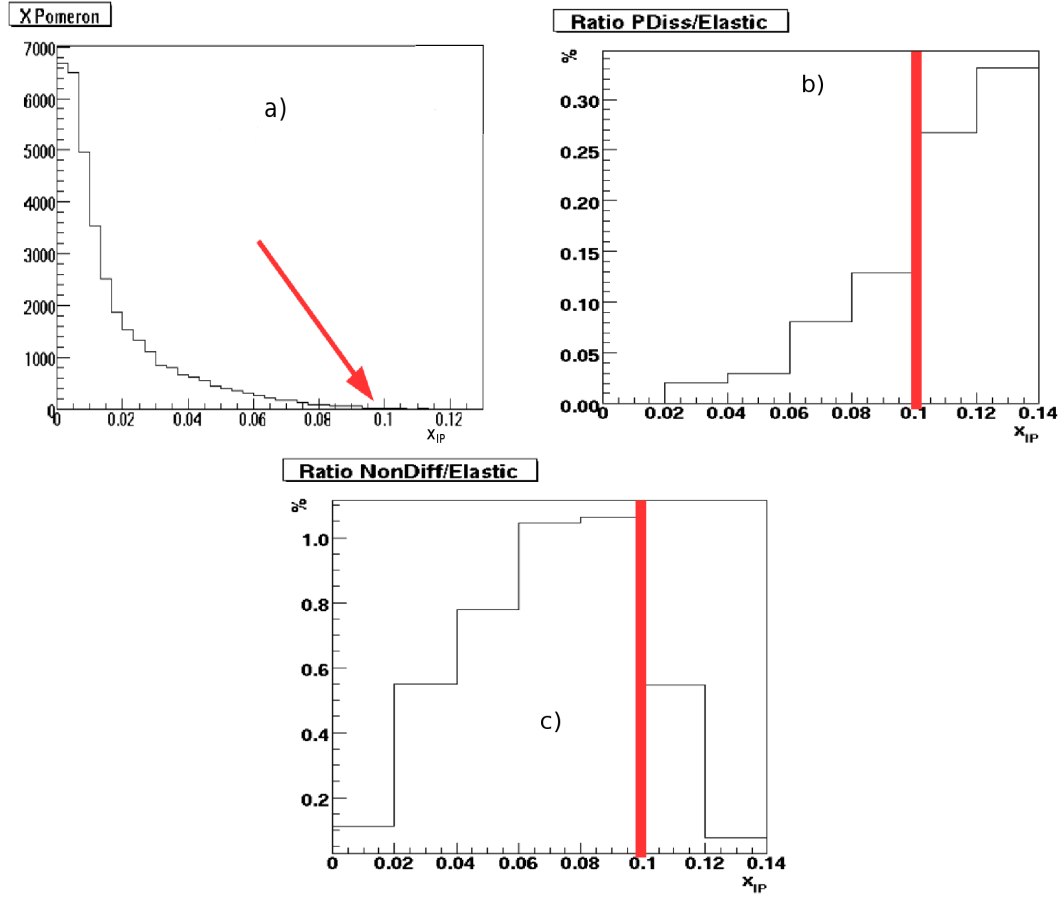
Figure 6.6: $x_{I\!P}$ dependence of inclusive diffractive DIS events simulated in FPS with the `RAPGAP` MC. The red arrow shows the upper limit on the FPS acceptance. b) ratio of proton dissociation events to diffractive events ($I\!P\ uds$, for definition see Sec. 5.1.1) as a function of $x_{I\!P}$, c) ratio of non-diffractive events to diffractive events ($I\!P\ uds$) as a function of $x_{I\!P}$. The red vertical line corresponds to the upper limit of the FPS acceptance.

diffractive DIS events in the FPS kinematical range is presented. The ratio of the background processes to the diffractive signal is rising with increasing value of $x_{I\!P}$, with maximal value of 0.15% in the case of proton dissociation and 1.0% in the case of non-diffractive events. The region of the highest background to signal ratio is denoted by the red arrow in the Fig 6.6 a). The values of the ratios of the diffractive signal to the non-diffractive and proton dissociative background are most significant at the high $x_{I\!P}$ tail, but at the level of 1 %. Therefore, the background induced by these two physics processes is not further considered in

this analysis.

6.7.2 Hardware Background

The PMTs and the scintillating fibres are sensitive to the "crosstalk". Even though a particular PMT or scintillator has not been hit directly, it can produce a signal which is accepted as a scattered proton candidate. The following procedure is correcting the measured data for these effects as well as for fake signal produced by the noise in the electronic parts of the FPS detector. This type of background will be further denoted as "hardware background".

The probability for the hardware background is independent on the U-V position (for the definition of U-V planes see Sec. 4.3) of the hit in the planes of the FPS detector. Two data samples have been selected - one with the protons emerging the interaction point in the cone of ± 15 $mrad$, other sample within the cone of ± 30 $mrad$. The distribution of hits in each coordinate (see Fig. 6.7) shows a peak close to 0 $mrad$ with width of approximately 1 $mrad$. The 15 $mrad$ sample contains the expected signal and background, the 30 $mrad$ sample consists of the signal and twice as high amount of background in comparison to the 15 $mrad$ sample. Following equation leads to estimation of the corrected signal:

$$S = 2 \cdot (S + B) - (S + 2B), \tag{6.31}$$

where S stands for signal and B for hardware background. A sample in the range 15 $mrad < \theta_{emitted} < 30$ $mrad$ (i.e. containing only background) has been selected and subtracted from the 15 $mrad$ in the analysis procedure.

The scattered or beam halo proton can hit the beam-pipe or the FPS detector itself. Such collision produces a shower, which is then registered in the detection area of the FPS. Due to the loose requirements on the hit multiplicity in the FPS stations, the event can be accepted. Since this shower production is independent on the U-V coordinates, the procedure described above takes into account this effect and corrects for it.

6.7.3 Coincidence Background

In diffractive events the signal from the FPS detector corresponding to the scattered proton is measured in parallel with the signal in the main H1 detector. This topology can be faked by "coincidence" background events. In the FPS, a well reconstructed proton is detected, even though its origin is not in the interaction. It is a randomly deflected beam proton and if in the same time window a DIS event in the main detector is reconstructed according to the selection criteria, a diffractive DIS event is faked. These protons come mainly from the protons
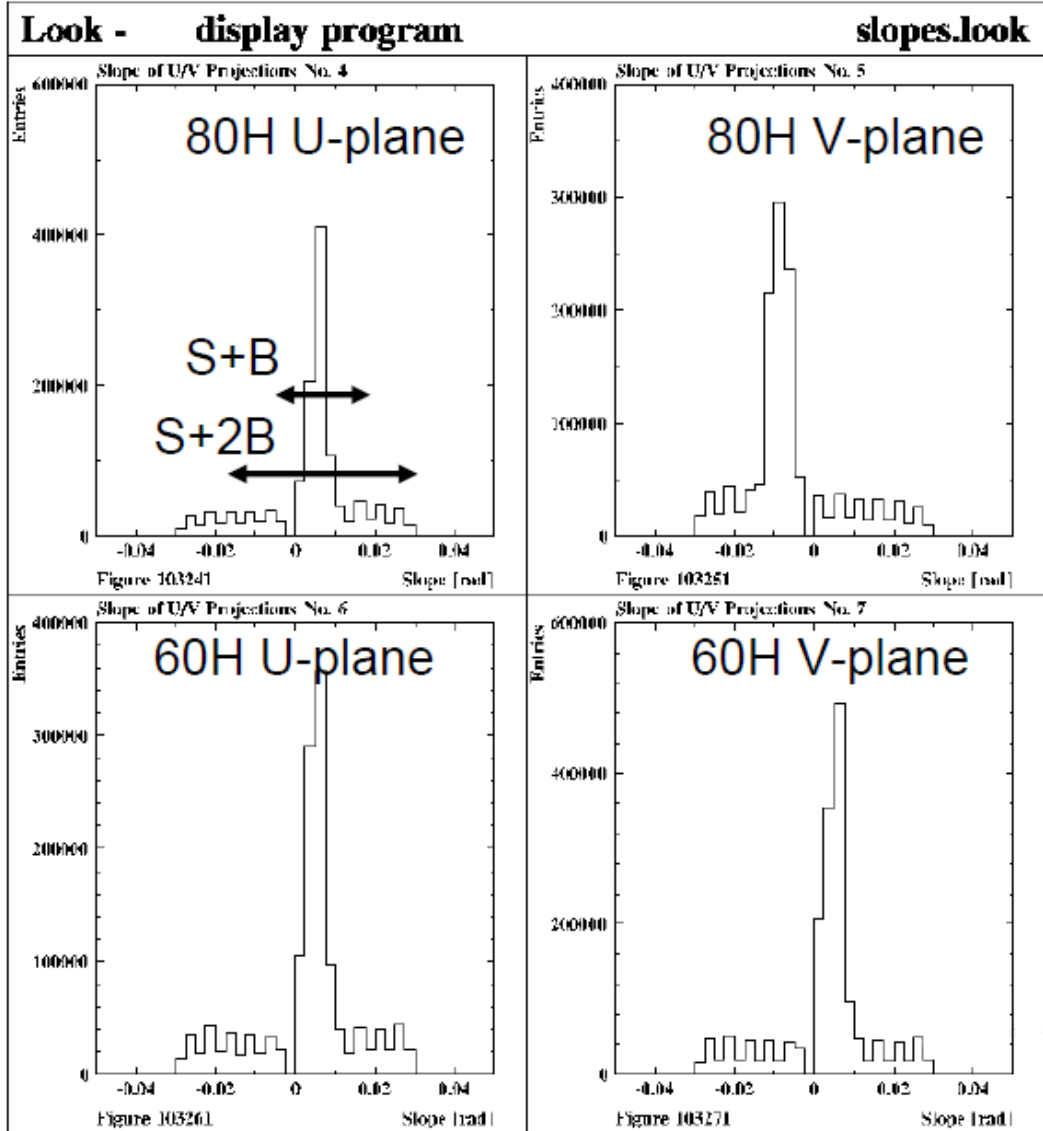
Figure 6.7: The number of hits as a function of the angle under which the proton has been emitted at the interaction point for the U and V projections for the 63 m and 80 m horizontal stations. The arrows in the U plane of the 80 m horizontal plane illustrate the 15 and 30 $mrad$ sample selection.

from the beam halo. In the following subsections two independent methods of rejections of coincidence background are described.

Bunch Crossing Method

The rough estimation of the coincidence background on the trigger element level is described in this subsection. On the DST level, it is possible to obtain the information on the trigger level not only from the current bunch crossing, i.e. interaction, but from the previous and following two bunch crossings as well. In the following, this information will be referred as BC-1,0,+1. In the BC0, the standard DIS selection is applied, which contains requirement for well reconstructed scattered electron, runs with good quality and at least one SpaCal sub-trigger active. A sub-sample with two central dijets has been selected as well. With the selected BC0 DIS event, the FPS TEs 164 and 165 (for definition see Sec. 4.5) are studied as a function of bunch crossings. The assumption is made, that the probability of having a DIS event right after or before a diffractive one is negligible in comparison to the background rate. Probability to have two diffractive events is assumed to be even smaller. That means, if in the BC0 a DIS event has been found, the FPS signal from other bunch crossings is produced by background. Assuming same background rate for the background in the BC0 as in the BC±1 event, a ratio of background to signal can be estimated taking the level of background in the neighbouring bunch crossings as a pedestal.

The study has been performed for the inclusive diffractive DIS selection and for the "2 central jets" topology. The bunch crossing method of estimating background is presented in Fig. 6.8. The pedestal is demonstrated with red horizontal line stretching over all three bunch crossings that are taken into account. The background in the inclusive diffractive DIS sample is $\sim 20\%$ and in the "2 central jet" topology $\sim 45\%$.

E+Pz Method

The Bunch crossing method based only on the trigger element information gives an approximate value of the background and serves as a feasibility study for different final state topologies. A more precise method based on the energy conservation is presented in this subsection. As defined in previous sections, the scattered proton is going along the positive z-axis, i.e. the $p'_Z \leq +920 \; GeV$. The variable $E + Pz$ defined as a sum of energy and the z component of the momentum of all particles

$$E + Pz = E^{FPS} + p_Z^{FPS} + E^{HFS} + p_Z^{HFS} + E^{elec} + p_Z^{elec} \qquad (6.32)$$

peaks at $E + Pz \approx 2 \cdot 920 = 1840 \; GeV$. Since the scattered electron goes to
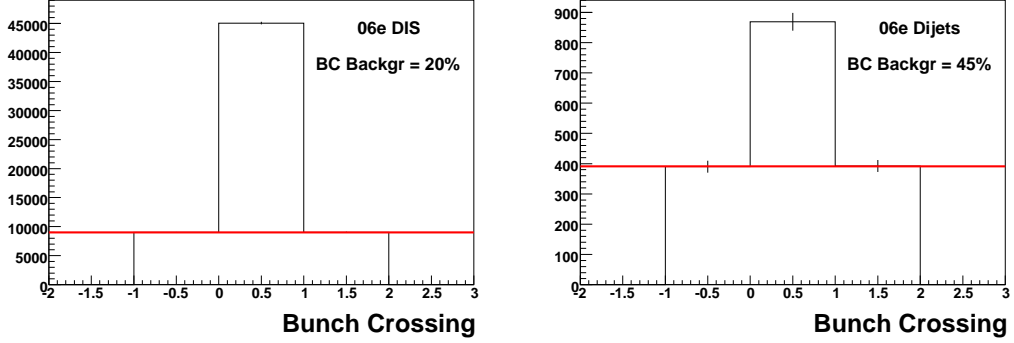
Figure 6.8: The signal and background trigger rate for bunchcrossings $0, \pm 1$ for the inclusive diffractive DIS (left) and for "2 central jets" selection for the 06e data taking period. The red horizontal line stands for the background pedestal.

the negative p_Z values and can be neglected in the sum, the major contributions come from the scattered proton and the HFS.

If we take into account the resolution of FPS detector and the fact that the proton energy can be reconstructed up to the value of 950 GeV, we can expect that events with $E + Pz > 1900\ GeV$ will belong mainly to the background.

Fig. 6.9 shows the $E + Pz$ distribution for inclusive diffractive DIS events. The full red line represents the analysis cut $E + Pz < 1880\ GeV$ which suppresses the background.

The contribution of the halo background below $E + Pz < 1880\ GeV$ is non-negligible, the background subtraction has been done with following method:

A dedicated data taking runs have been undertaken with the electron beam turned off, i.e. the signal collected in FPS originates from halo protons only. This sample has been convoluted with the non-diffractive DIS selection in order to mimic the coincidence events. In this sample and in the signal selections, the $E + Pz$ observable has been estimated (for the halo protons, $E + Pz = E + Pz(FPS)$, for the non-diffractive events the $E + Pz = E + Pz(HFS)$) and then these two observables have been randomly combined together in order to mimic coincidence background. This sample will be further referred as "background sample". Under the assumption, that in the signal sample, events with $E + Pz > 1900\ GeV$ belong to the background, the background sample with $E + Pz > 1900\ GeV$ has been normalised to the tail in the signal sample. Since the tail of the signal sample is described very well (See Fig. 6.9) by the background, the assumption holds. The shape of the background distribution below the analysis cut is then modelled by the background sample. In the analysis, the halo background has been estimated
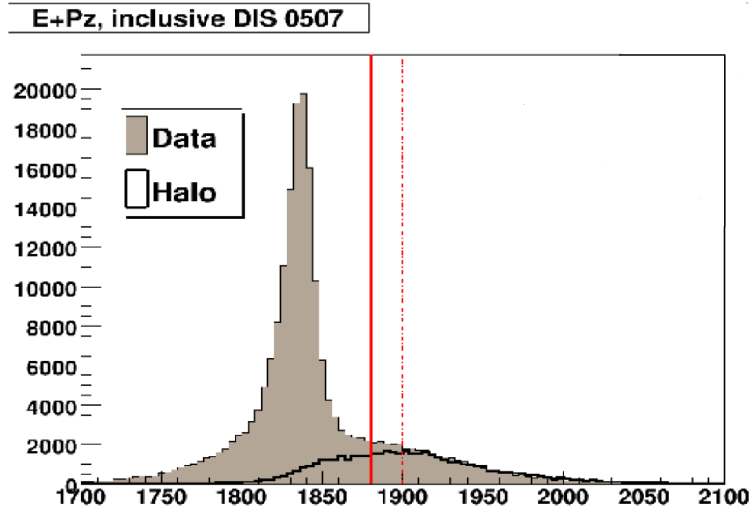
70

Figure 6.9: The $E + Pz$ distribution of inclusive diffractive DIS events. The dotted red line stands for the upper limit for the diffractive events, the full red line stands for the cut applied in the analysis to suppress the coincidence events.

for every observable and subtracted. In the analysis of 06e data running period, the background in the inclusive diffractive DIS selection is $\sim 19\%$ and in the "2 central jets" selection $\sim 50\%$ (See Fig. 6.10).

6.7.4 Consistency Check

A consistency test for the two independent coincidence background estimations is discussed in this section. As shown in previous sections and due to to errors of background subtraction, the two methods give similar results of $\sim 20\%$ background for the inclusive diffractive DIS selection and $\sim 50\%$ for the "2 central jets" selection.

For this analysis the $E + Pz$ method of halo protons subtraction will be used, since it provides a more detailed information and allows to subtract the background for every distribution separately. Estimation of $E + Pz$ background for both jet topologies is presented in Fig. 6.11. The $E + Pz$ background subtraction is a source of systematic error and will be treated in the estimation of the systematic errors.
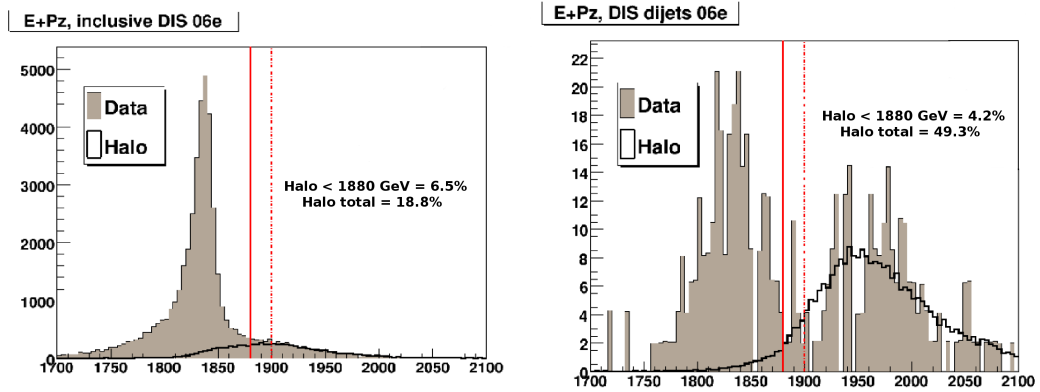
Figure 6.10: The $E + Pz$ distribution for inclusive DIS (left), the $E + Pz$ distribution for cental dijets (right). The solid red line represents the cut $E + Pz = 1880 \; GeV$.
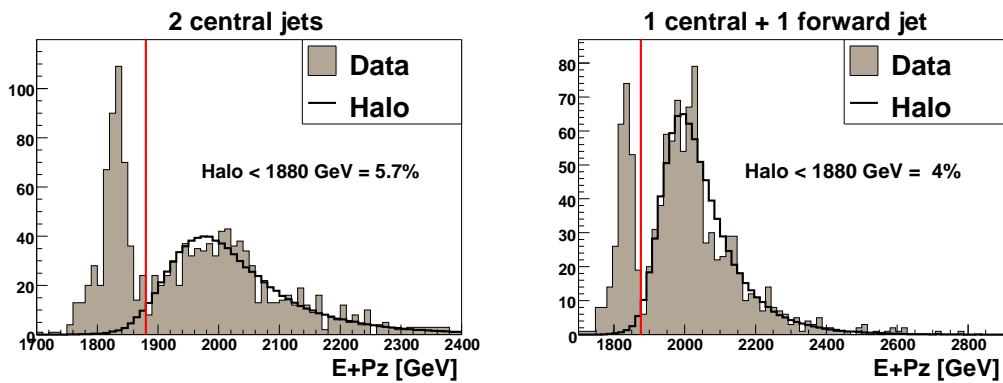

Figure 6.11: The $E + Pz$ distribution for the "2 central " jet selection (left), the $E + Pz$ for the "central + forward" jet selection (right). The halo tail below the cut represented by the solid red line is used for the background estimation.

6.8 Cuts Summary

The Table 6.2 summarise the analysis cuts.

cut	value
$|VtxZ_{prim}|$	$< 35\ cm$
E'_e	$> 10\ GeV$
r_{clus}	$< 4\ cm$
r_{SpaCal}	$\in\ (13\ cm, 75\ cm)$
Q^2_{av}	$\in\ (4\ GeV^2, 110\ GeV^2)$
y_{av}	$\in\ (0.05, 0.7)$
$|y_e - y_{da}|$	< 0.3
$E - Pz$	$\in (35\ GeV, 70\ GeV)$
E'_p	$> 820\ GeV$
p'_X	$\in (-0.63\ GeV, -0.27\ GeV)$
p'_Y	$\in (-0.8\ GeV, 0.8\ GeV$
$x_{I\!P}$	< 0.1
$E + Pz$	$< 1880\ GeV$
"2 central jets"	
$p^*_{T,1}$	$> 5\ GeV$
$p^*_{T,2}$	$> 4\ GeV$
$\eta_{1,2}$	$\in (-1.0,\ 2.5)$
"1 central + 1 forward jet"	
$p^*_{T,1}$	$> 3.5\ GeV$
$p^*_{T,2}$	$> 3.5\ GeV$
M_{12}	$> 12\ GeV$
η_1	$\in (-1.0,\ 2.5)$
η_2	$\in (1.0,\ 2.8)$
η_2	$> \eta_1$

Table 6.2: Summary of analysis cuts

After applying all selection criteria and the background subtraction 460 events for the "2 central jets" topology and 245 events for the "1 central + 1 forward jet" topology survived.

6.9 Jet Profiles

First requirement for the correct description of the jet variables is that the energy flow of the particles which belong to the jet as reconstructed with the k_T-algorithm
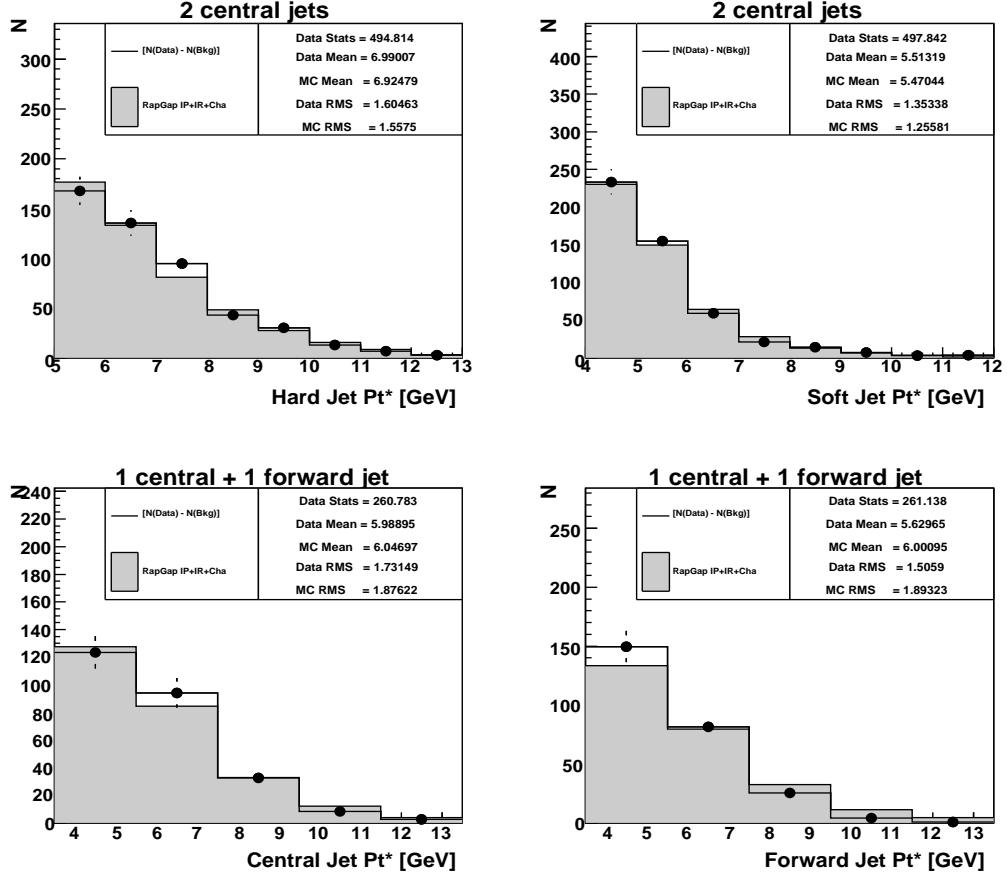
Figure 6.12: Transverse momenta in the hadronic centre-of-mass system for both jet topologies.

is well described.

The Fig. 6.12 presents the distributions on the detector level of jet transverse momenta for both jets in both topologies in the hadronic centre-of-mass frame.

In the control plots 6.13 and 6.14, the E^* and E_T^* flows are presented as a function of η^* and ϕ^*. In the profile of a jet j, its axis is taken as a reference. The sum of the transverse energy runs over all particles that have been assigned to the jet by the jet finding algorithm. Then, the distance of every particle i is plotted as $\eta_j^* - \eta_i^*$ and $|\phi_j^* - \phi_i^*|$ respectively. The distributions are normalised to the number of events and are weighted by the transverse energy E_T^* of each contributing particle. In this way, the total integral over the jet profiles should be in rough agreement with the mean transverse energy of the jets when measured

from the jet distributions. The jet particles are centred in a narrow peak around the jet η^* and ϕ^* axes. The data are well described by the Monte Carlo.

jet	$\int \frac{dE_T^*}{N \cdot d\eta^*} d\eta^*$	$\int \frac{dE_T^*}{N \cdot d\phi^*} d\phi^*$	$< p_T^* >$
Hard Jet "2c"	$7.1\ GeV$	$7.1\ GeV$	$7.0\ GeV$
Soft Jet "2c"	$5.5\ GeV$	$5.5\ GeV$	$5.5\ GeV$
Central Jet "1c+1f"	$6.1\ GeV$	$6.1\ GeV$	$6.0\ GeV$
Forward Jet "1c+1f"	$5.7\ GeV$	$5.7\ GeV$	$5.6\ GeV$

Table 6.3: Consistency of jet transverse energy measurement

Table 6.3 presents the integrated transverse energies over η^* and ϕ^* jet profiles (Figs. 6.13 and 6.14) and the means of the control plots of the transverse energy (Fig. 6.12). The numerical comparison is presented only for data.

The values obtained with the integration over jet profiles are in an excellent agreement with the mean values of the mean values of the transverse energy distributions.

6.10   Description of Data by Monte Carlo

The cross section measurement is performed on the level of stable hadron and the corrections from detector to hadron level are done with the bin-by-bin method. It is therefore essential that the simulated Monte Carlo describes the data within the errors well. In order to achieve the best description of the data by Monte Carlo, reweighting of the MC at the detector level to the data is applied. The observables chosen for the reweighting have been: $Zvtx$, y, pt_2^*, η_2^*, $|\Delta\eta^*|$, $x_{I\!\!P}$ and $z_{I\!\!P}$ for the "2 central jet topology" and $Zvtx$, y, η_2, $|\Delta\eta^*|$, β and $z_{I\!\!P}$ for the "1 central + 1 forward jet" topology. The distributions have been reweighted one after the other, the comparison of original and reweighted distributions are shown in the Figs. 6.15 and 6.16.

6.11   Control Plots

6.11.1   RAPGAP LLPS

In this section, the control plots for both jet topologies are presented.

In the Sec. 5.1.1, the three constituents of the Monte Carlo sample were described: the elastic pomeron, reggeon and charm exchange. The Fig. 6.17 presents the relative contribution of these three sub-samples in comparison to
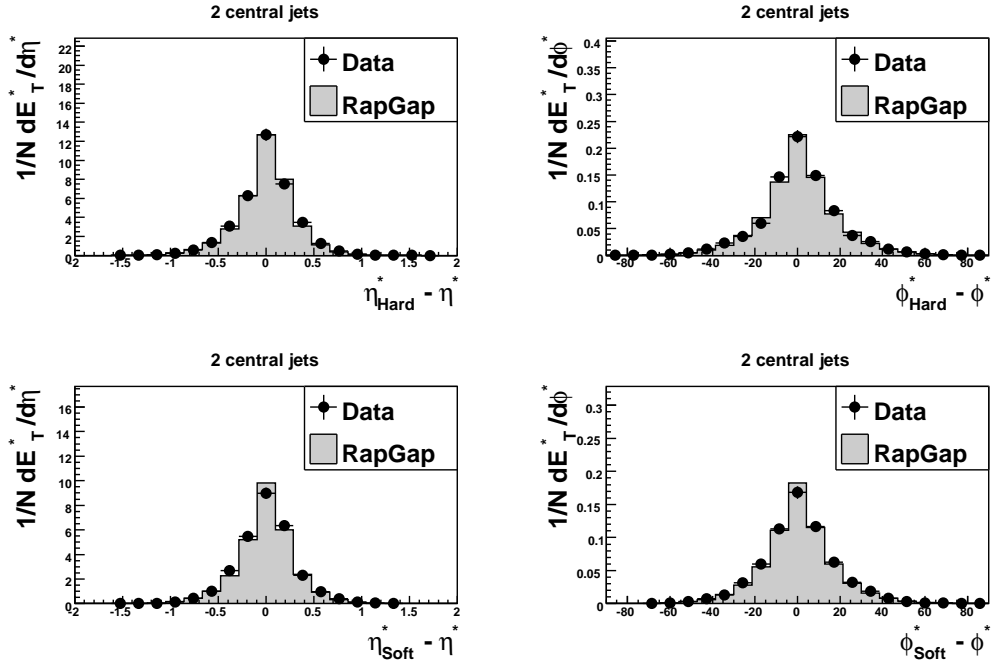
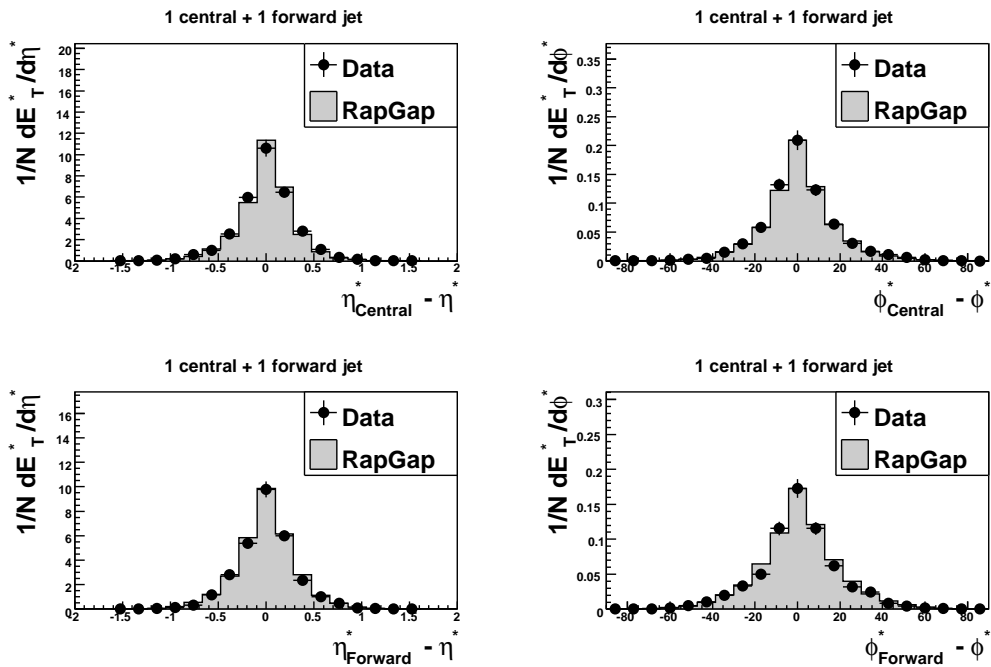Figure 6.13: Jet transverse energy profiles for "2 central jets" selection.

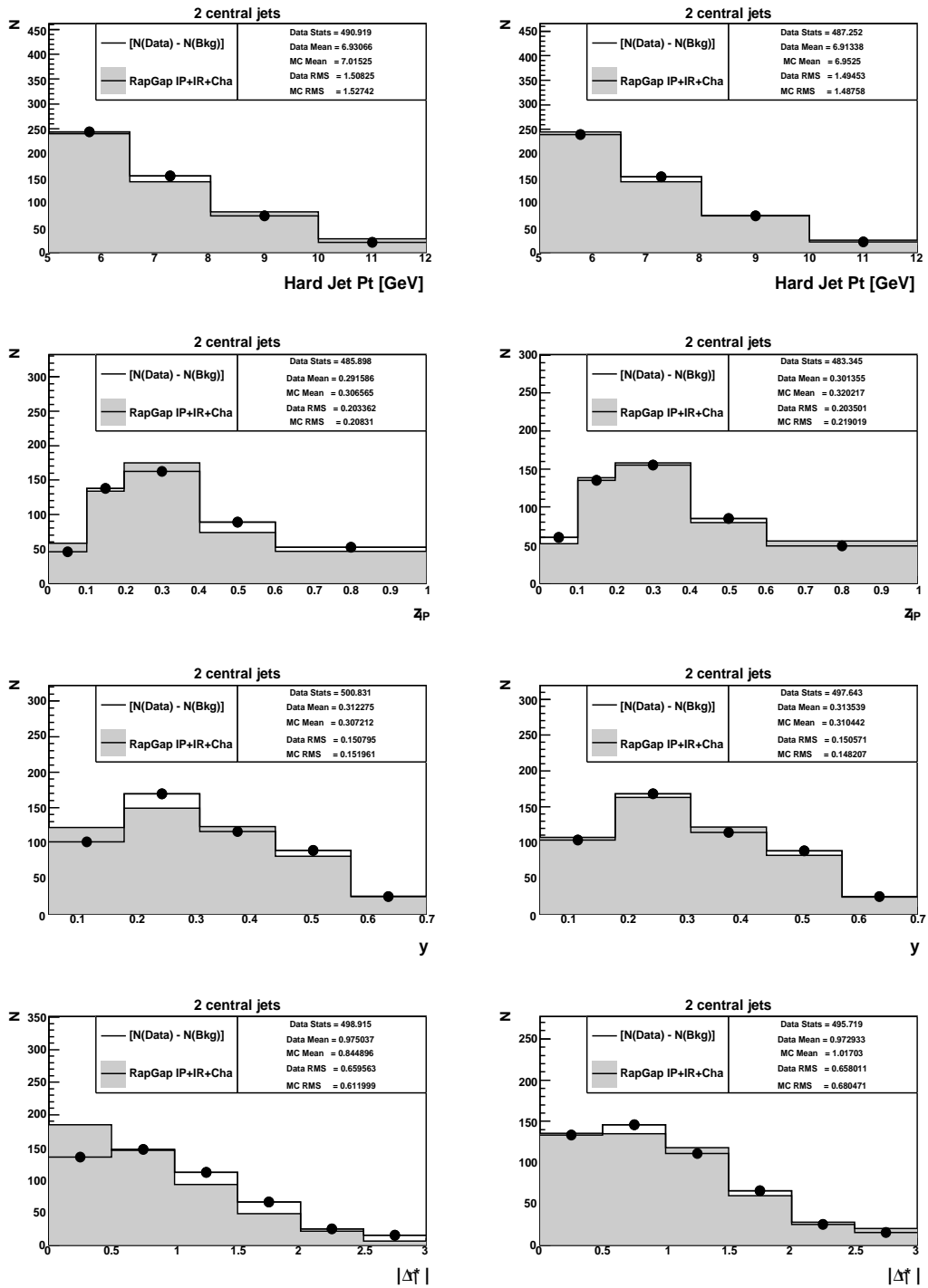Figure 6.14: Jet transverse energy profiles for "1 central + 1 forward jet" selection.

Figure 6.15: Selected "2 central jets" distributions before (left) and after (right) the reweighting of the MC to the data.
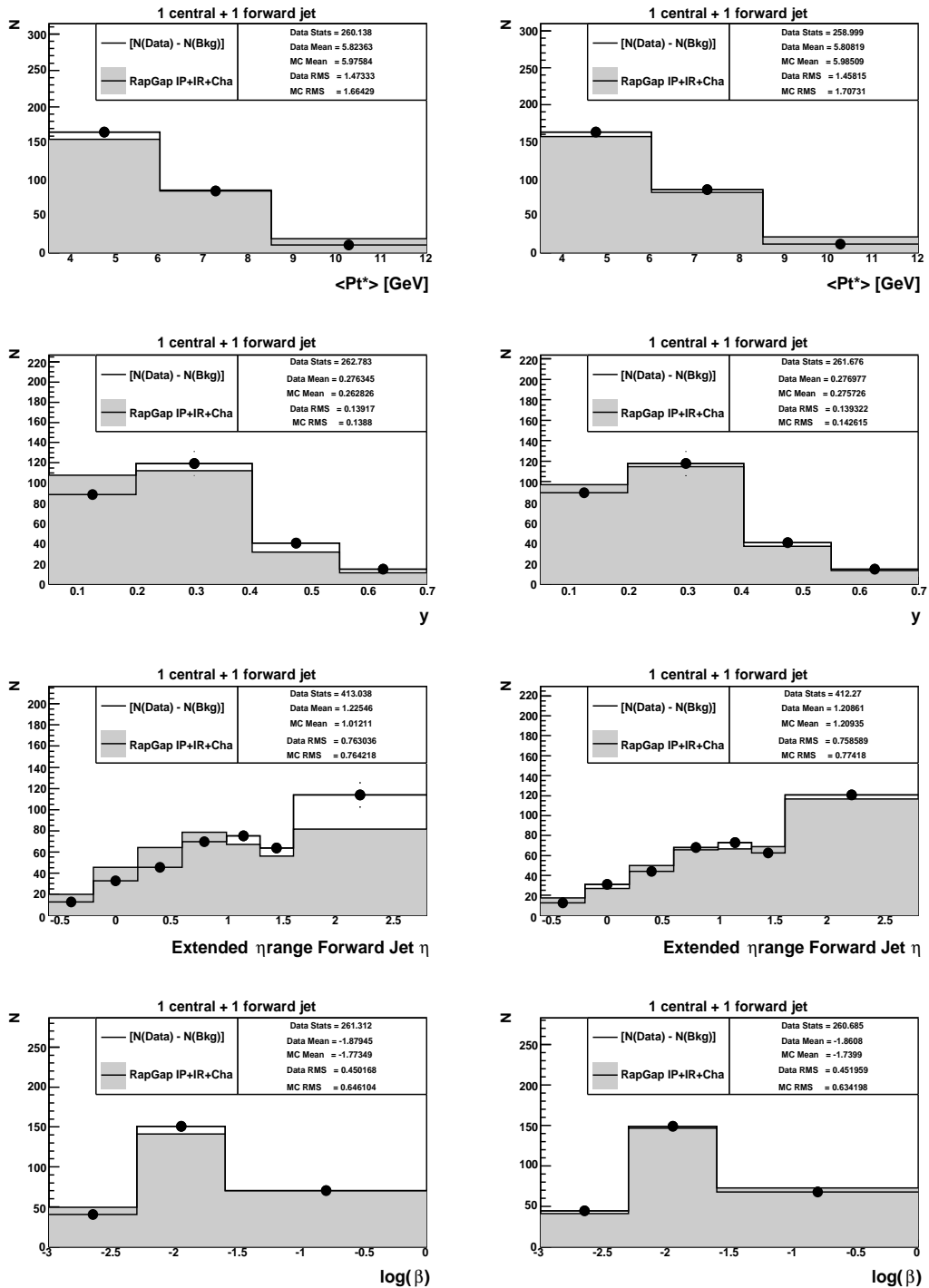
77

Figure 6.16: Selected "1 central + 1 forward jet" distributions before (left) and after (right) the reweighting of the MC to the data.
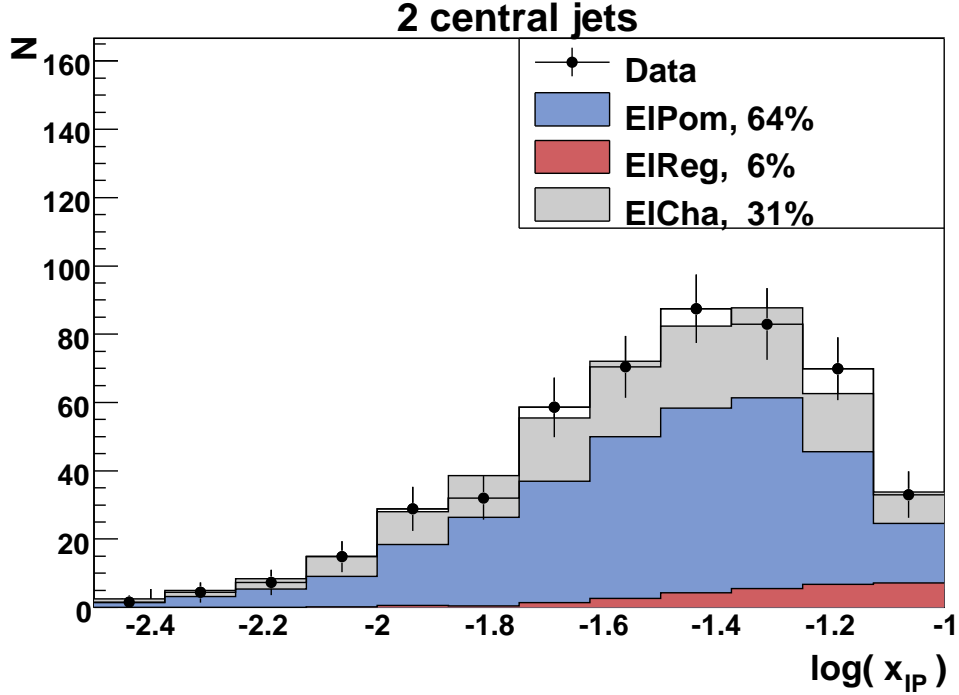
Figure 6.17: The distribution of $\log(x_{I\!\!P})$ as measured with the FPS detector. The elastic pomeron contribution ("$I\!\!P$ uds") is displayed in blue, the elastic reggeon ("$I\!\!R$ uds") in red and the charm ("$I\!\!P$ charm") component of the Monte Carlo sample in grey colour.

the data in the $\log(x_{I\!\!P})$. The sample of light quarks produced by elastic pomeron exchange ("$I\!\!P$ uds") creates $\sim 64\%$ of the total Monte Carlo signal, the light quarks produced by elastic reggeon exchange ("$I\!\!R$ uds") $\sim 6\%$ and the charm quark produced by elastic pomeron exchange ("$I\!\!P$ charm") $\sim 30\%$. The reggeon contribution is rising with increasing $x_{I\!\!P}$.

Control plots for both jet topologies are presented in Figs. 6.18-6.25. The description of the data by Monte Carlo is satisfactory and the MC can be therefore used for the bin-by-bin corrections for the detector effects.
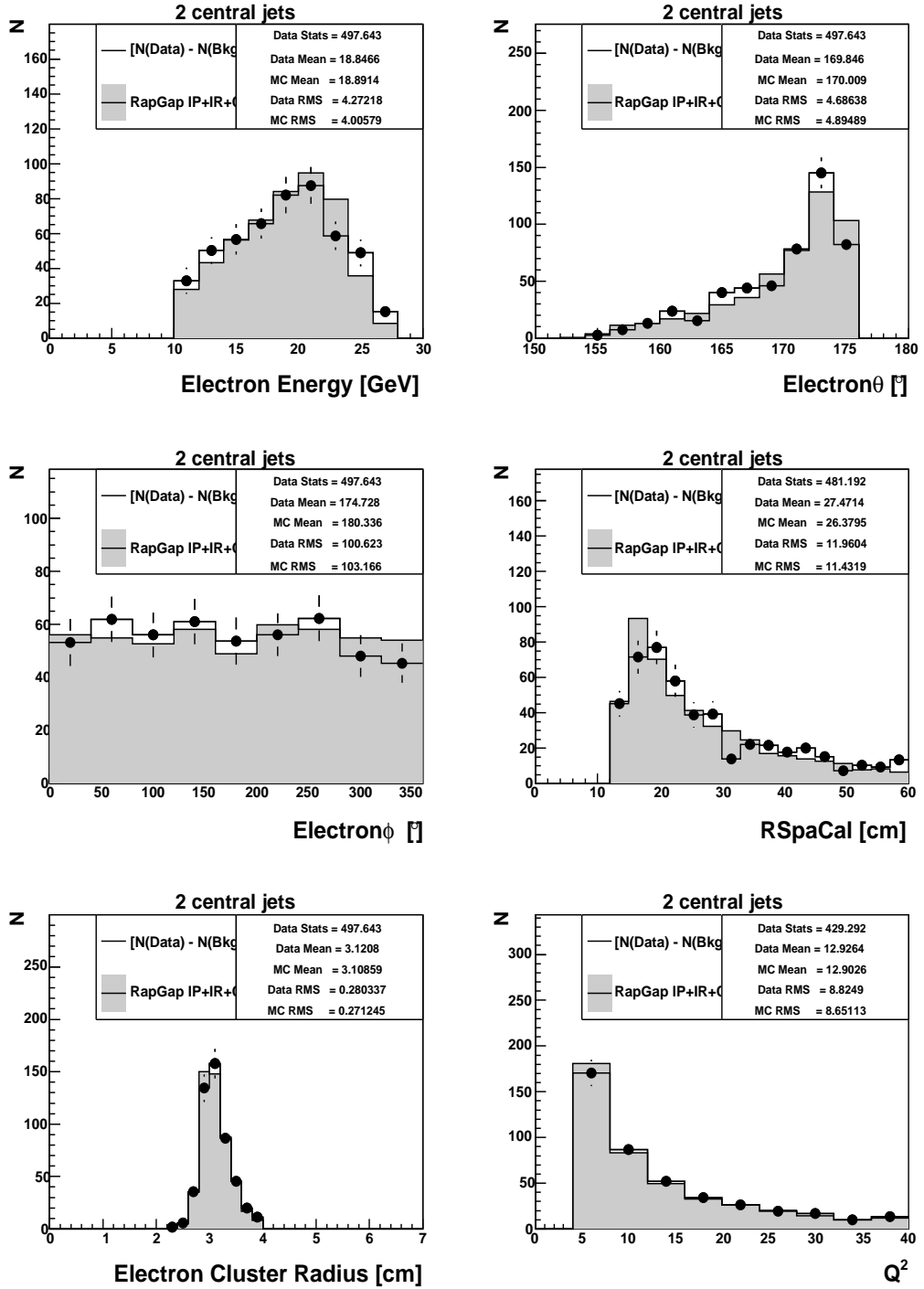
Figure 6.18: The data and `RAPGAP` MC distributions (normalised to data) for the "2 central jets" selection.
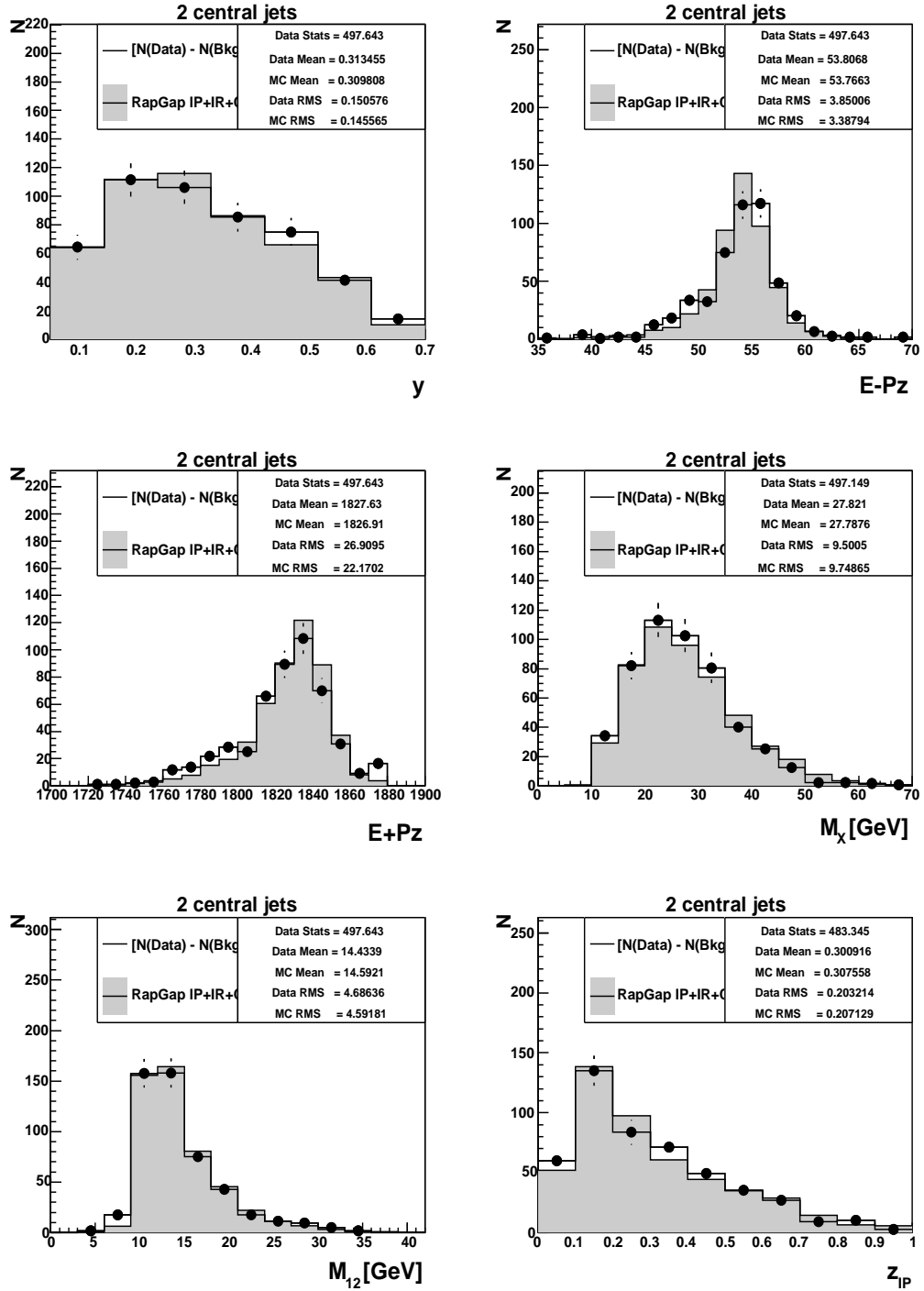
Figure 6.19: The data and RAPGAP MC distributions (normalised to data) for the "2 central jets" selection.
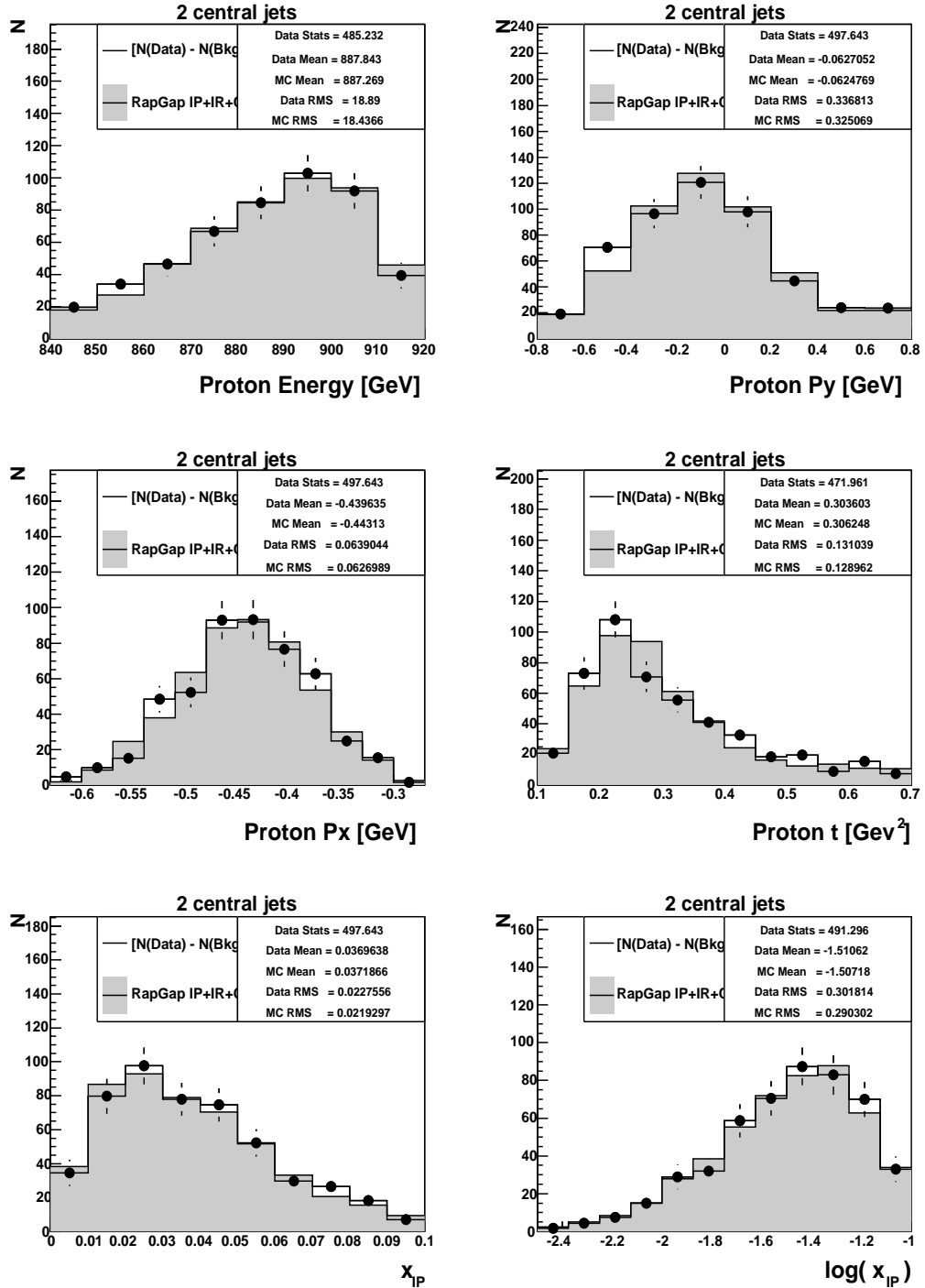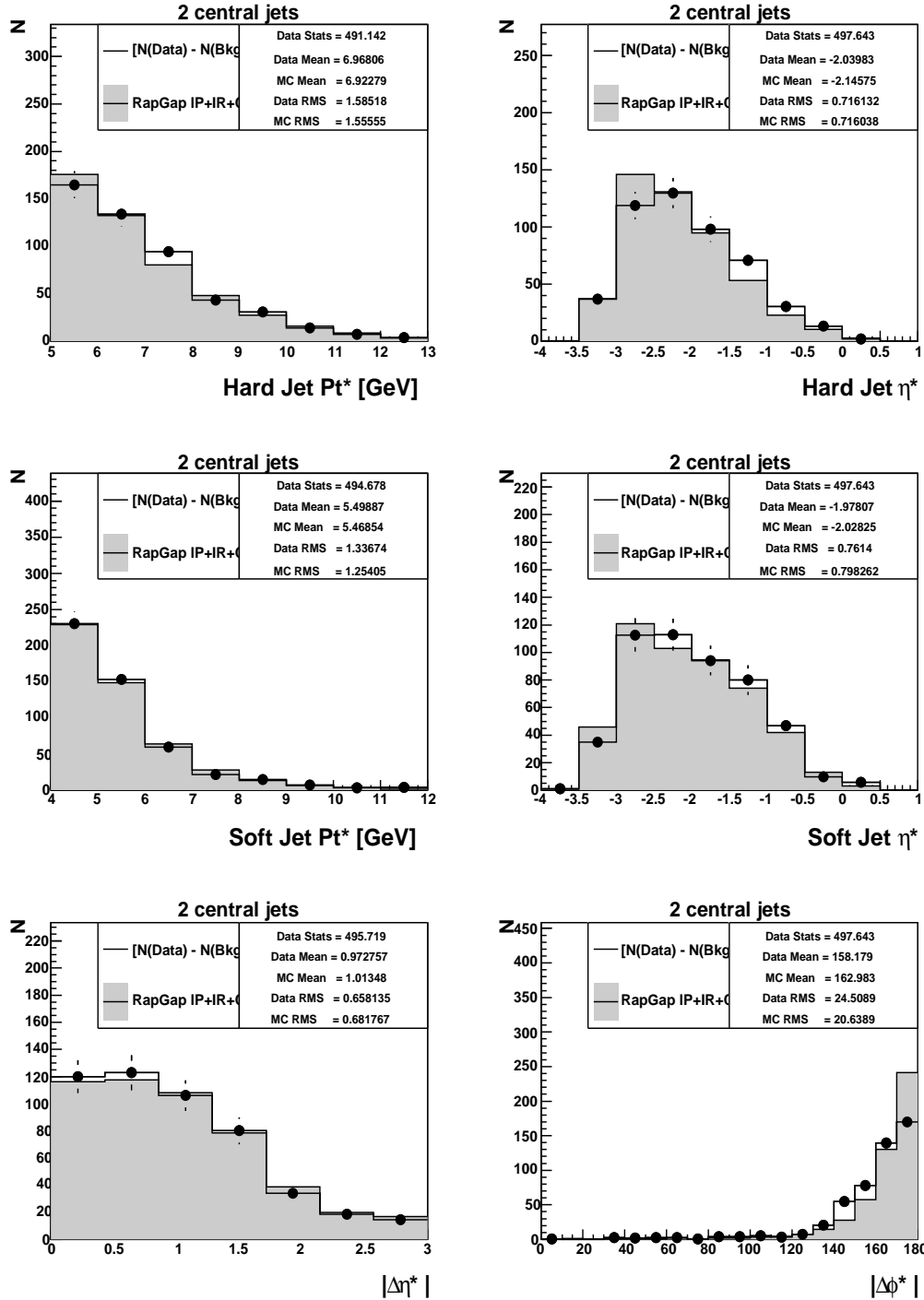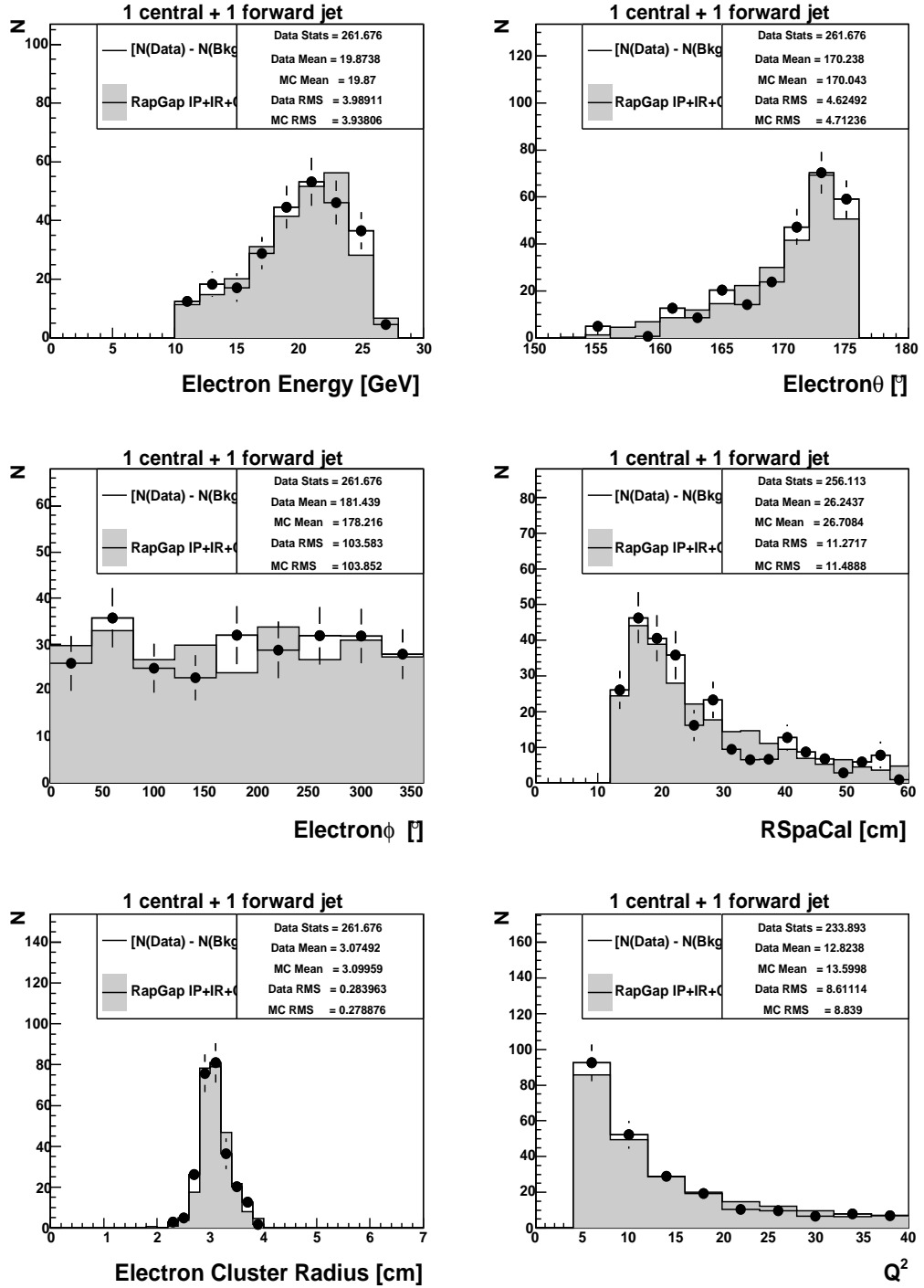
Figure 6.20: The data and RAPGAP MC distributions (normalised to data) for the "2 central jets" selection.

Figure 6.21: The data and `RAPGAP` MC distributions (normalised to data) for the "2 central jets" selection.

Figure 6.22: The data and `RAPGAP` MC distributions (normalised to data) for the "1 central + 1 forward jet" selection.
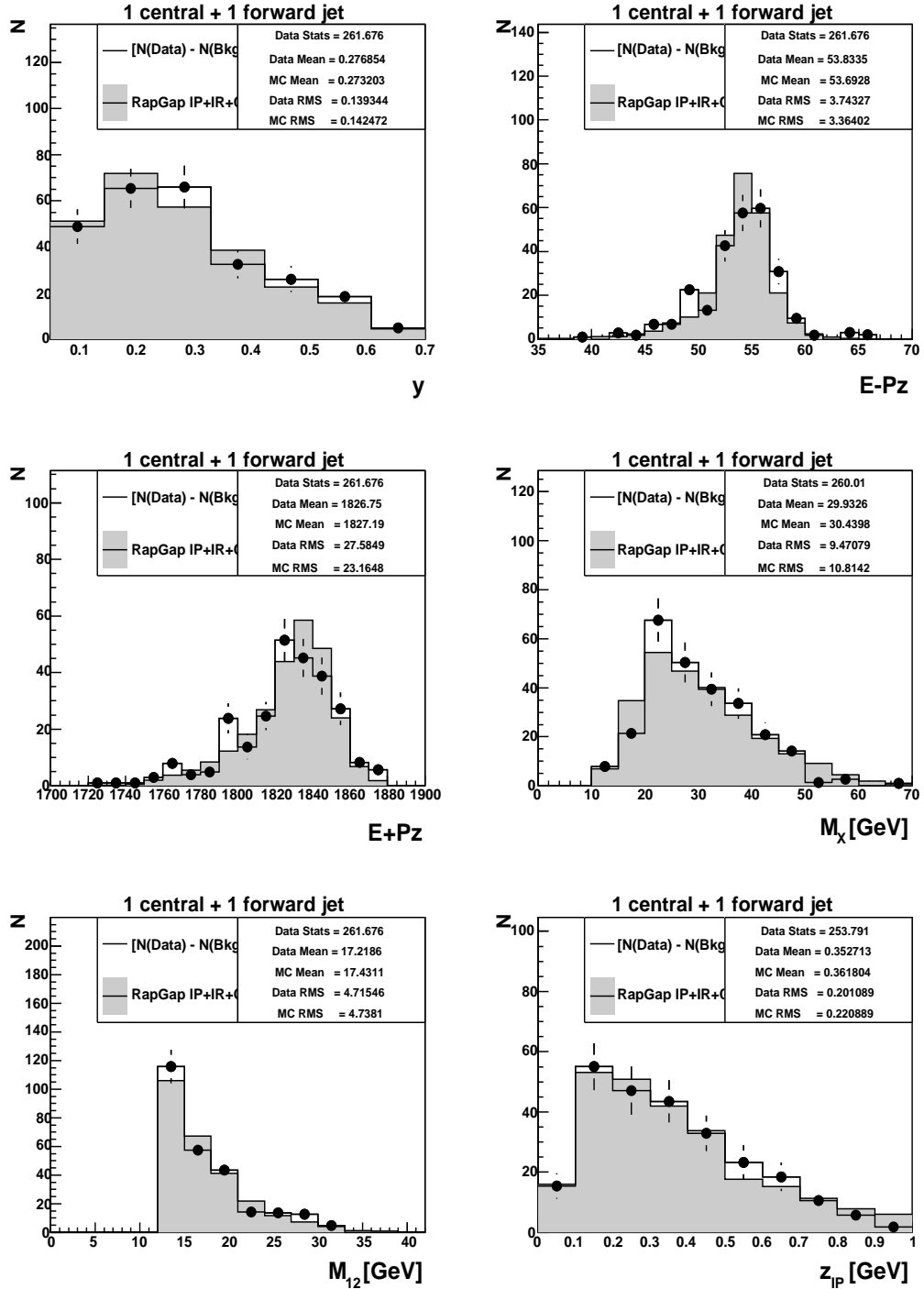
Figure 6.23: The data and `RAPGAP` MC distributions (normalised to data) for the "1 central + 1 forward jet" selection.
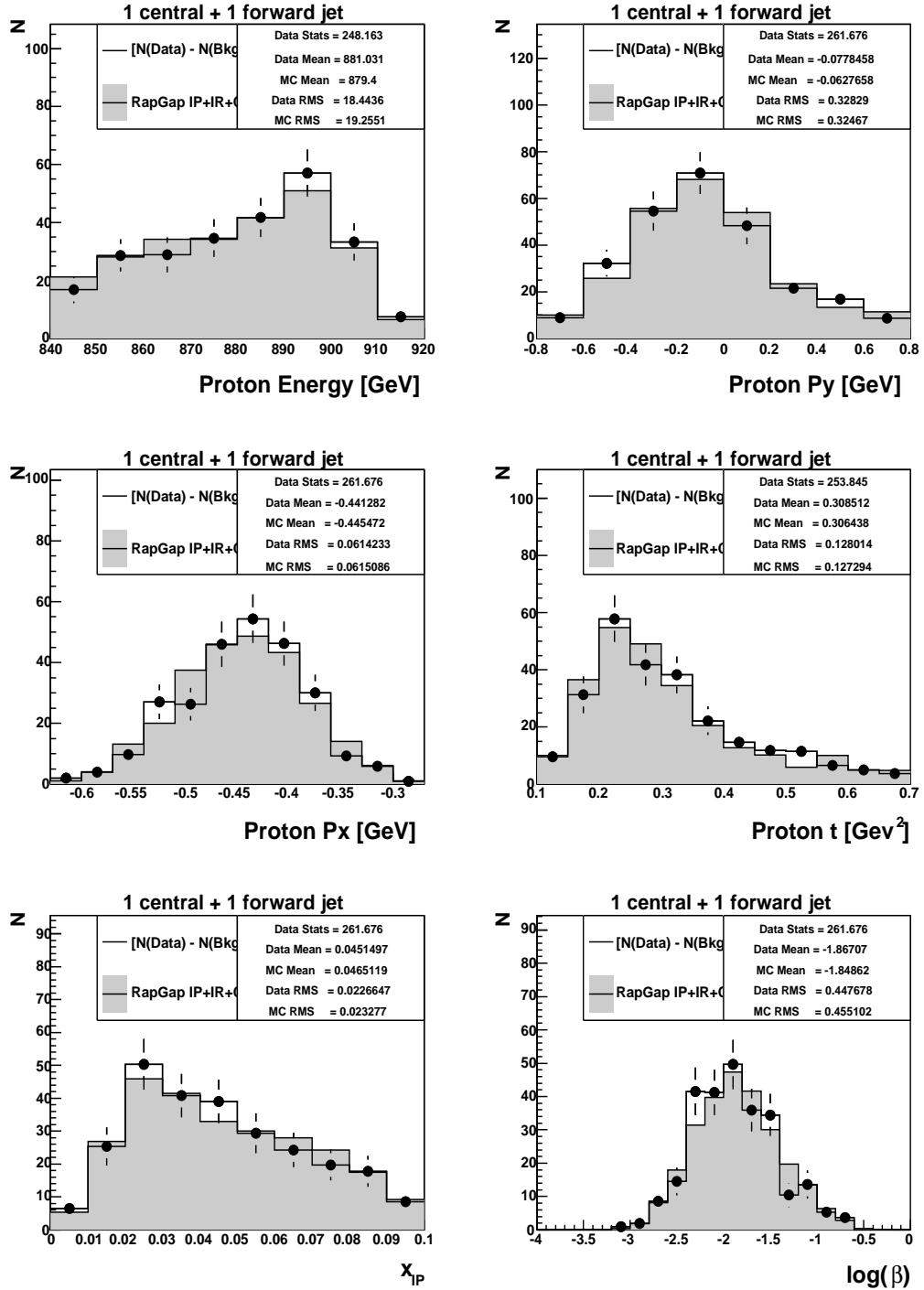
Figure 6.24: The data and RAPGAP MC distributions (normalised to data) for the "1 central + 1 forward jet" selection.
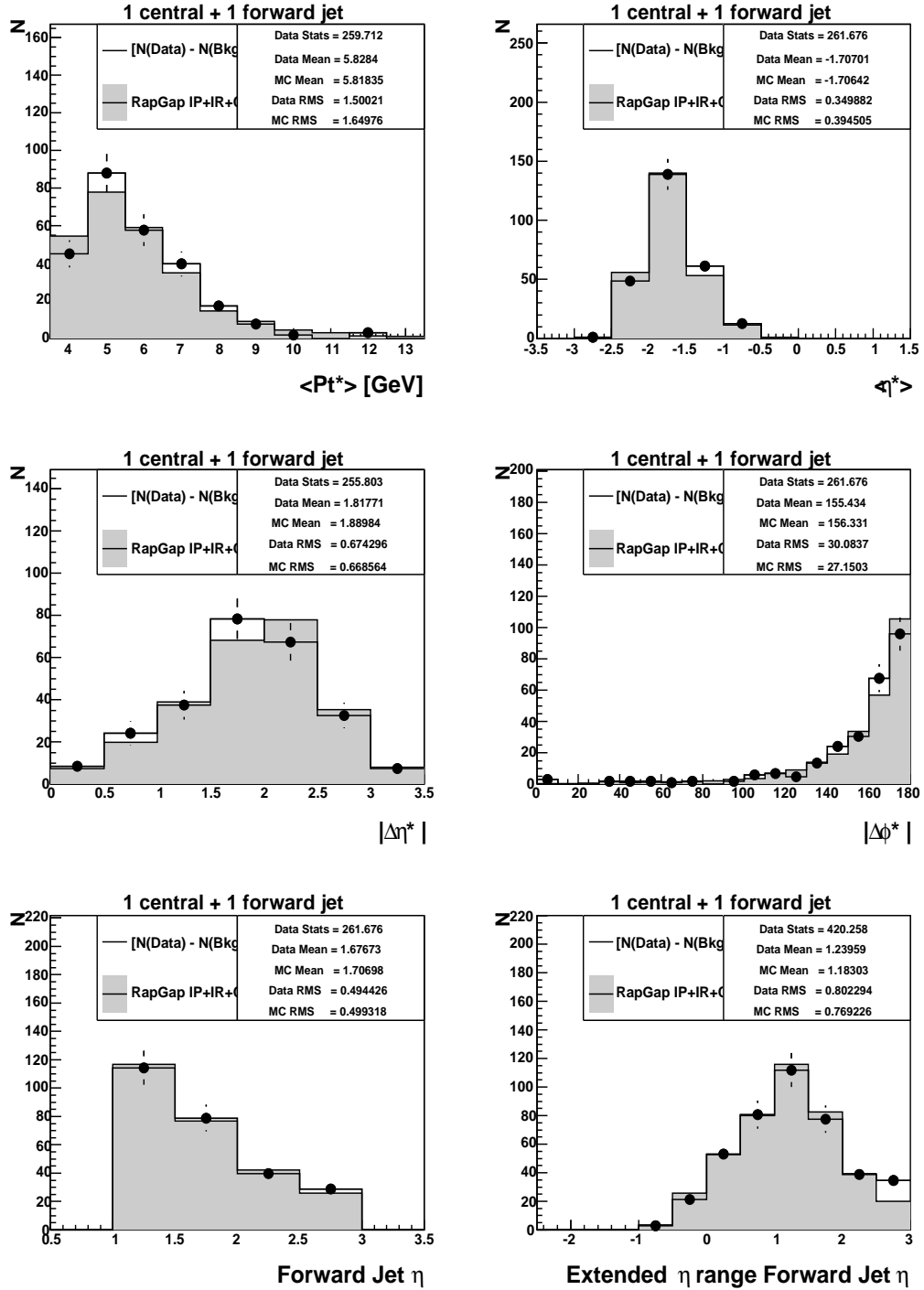
Figure 6.25: The data and `RAPGAP` MC distributions (normalised to data) for the "1 central + 1 forward jet" selection.

6.11.2 `RAPGAP` CDM

For the study of hadronisation corrections, additional MC with parton showers generated with the CDM model has been generated and simulated. This MC can be used for the estimation of the hadronisation effects only if the simulated spectra are in a rough agreement with the measured data.

Control plots for data and CDM MC are presented in Figs. 6.26 and 6.27. For the reweighting of the MC to the data the same parametrisation has been used as for the `RAPGAP` LLPS MC. The agreement between data and CDM MC is acceptable, this MC will be used for the estimation of hadronisation uncertainties.
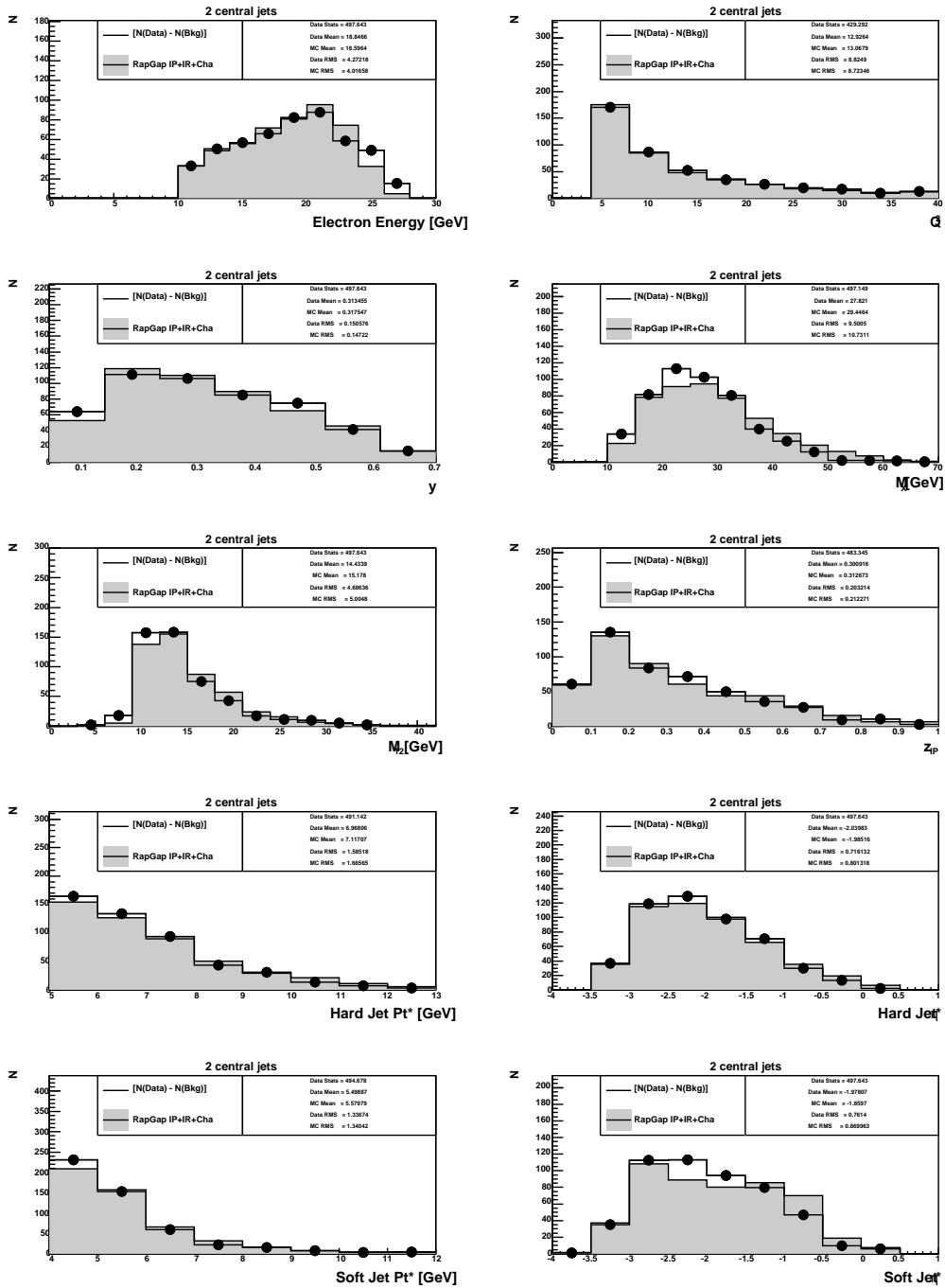
Figure 6.26: The data and `RAPGAP` CDM MC distributions (normalised to data) for the "2 central jets" selection.
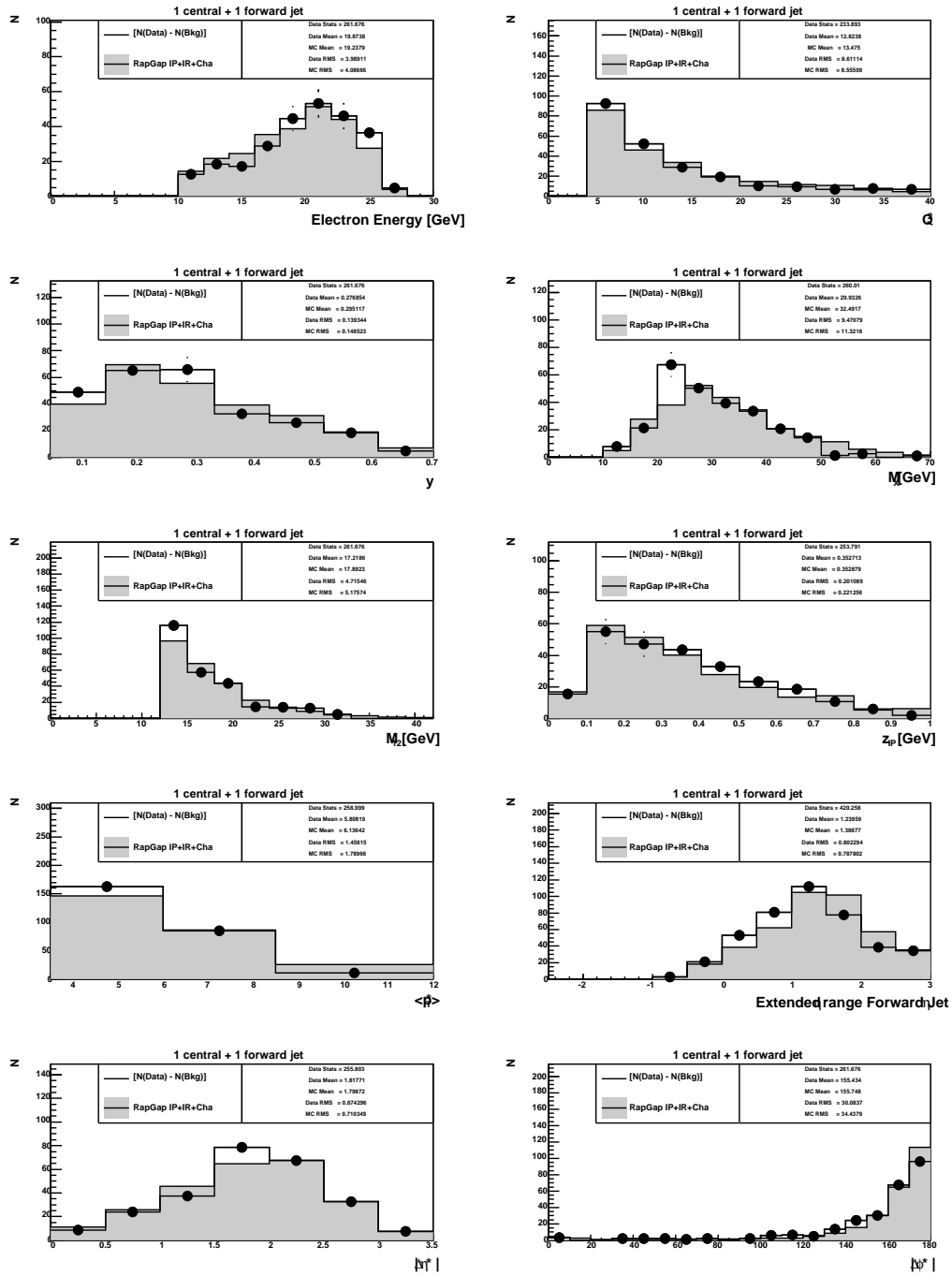
Figure 6.27: The data and `RAPGAP` CDM MC distributions (normalised to data) for the "1 central + 1 forward jet" selection.

Chapter 7

Cross Section Measurement

The measurement of the cross section will be described in this chapter, as well as the estimation of correction factors and systematic uncertainties. The single differential cross sections are measured for the "2 central jet" topology in the variables $p^*_{T,1}$, $p^*_{T,2}$, Q^2, y, $|\Delta\eta*|$, $z_{I\!P}$, $\log(x_{I\!P})$ and t and for the "1 central + 1 forward jet" topology in $< p^*_T >$, y, $|\Delta\eta*|$, $z_{I\!P}$, $log(\beta)$, $|\Delta\phi*|$, η_2. For definition of η_2 see Eq. 6.26.

In the measurement of the differential cross section in η_2 the pseudorapidity range of the forward jet is extended to $-0.6 < \eta_2 < 2.8$.

7.1 Definition

The total cross section is defined in a simplified way as

$$\sigma = \frac{N}{L},\tag{7.1}$$

where N stands for number of events and L for integrated luminosity. The differential cross section in variable X is measured according to the formula:

$$\frac{d\sigma}{dX}_j = \left(\sum_{i=05e1}^{07p} \frac{N^i_{obs} - N^i_{bkg}}{\mathcal{A}^i \cdot \mathcal{E}^i_{FPStrack} \mathcal{L}^i} \right)_j \frac{1}{\Delta^X_j} \, \mathcal{C}^{rad}{}_j,\tag{7.2}$$

for every bin j. The number of observed events N_{obs} has to be corrected by background subtraction N_{bkg}, the sum runs over the five sub-periods of HERA II data, $\mathcal{A}^i_{\mathrm{comb}}$ stands for the combined geometrical acceptance of H1 and FPS and the FPS kinematical acceptance described in Sec. 4.3. The $\mathcal{E}^i_{\mathrm{FPStrack}}$ is the FPS track reconstruction efficiency (described in Sec. 4.4) and $\mathcal{L}$ is the luminosity. The run-period independent radiative corrections $\mathcal{C}_{\mathrm{rad}}$ are applied on the cross

section divided with the width of the corresponding bin j (Δ^X). The background subtraction has been described in Sec. 4.3 and 6.6 in detail.

7.2   Detector - Hadron Level Correlations

Once the good agreement between data and Monte Carlo in the control plots is established, the correlations between detector (reconstructed) and hadron level have to be investigated. Figs. 7.1 and 7.3 present the two dimensional correlation plots of observable "O" with the detector level on the Y-axis and hadron level on the X-axis. The detector - hadron resolution for observable "O" is defined as:

$$Resolution = \frac{O^{rec} - O^{gen}}{O^{gen}} \tag{7.3}$$

The resolutions are shown in Figs. 7.2 and 7.4. The observables directly influenced by the measurement of the hadronic final state ($p_{T,1}^*$, $p_{T,2}^*$, M_{12}) have worse resolution in comparison to the diffractive and basic kinematical variables ($\log(x_{I\!\!P})$, Q^2, y). The observable $z_{I\!\!P}$ (for definition see Eq. 2.35) shows the worst resolution for both jet topologies.

7.3   Differential Cross Section Binning

The differential cross section measurement as obtained with the bin-by-bin method relies on good description of data by Monte Carlo and acceptable detector - hadron level correlations. Once these criteria are fulfilled, the proper binning of the differential cross section distributions has to be chosen. The requirement is that the migrations between the bins and from outside of the measured phase space are minimal. The *Purity*, which is defined as

$$P = \frac{N_{rec\&\&gen}^i}{N_{rec}^i} \tag{7.4}$$

quantifies for each bin i the migrations from other bins on the generator level. The index rec (gen) stands for selection with all reconstructed (generated) cuts applied. In the nominator, only events which belong to the particular bin i on reconstructed AND generated level in the same time are filled, whereas in the denominator only reconstructed events in the bin i are filled. Total *Purity* of the sample can be defined as ratio of events passed by generator AND reconstructed level selection compared to the reconstructed level selection. The total *Purity* of the "2 central jet" topology is 75%, for the "1 central + 1 forward jet" topology is the total *Purity* 64%. The binning of the one dimensional cross sections has been chosen in order to obtain purities in each bin to be higher than 30%. The
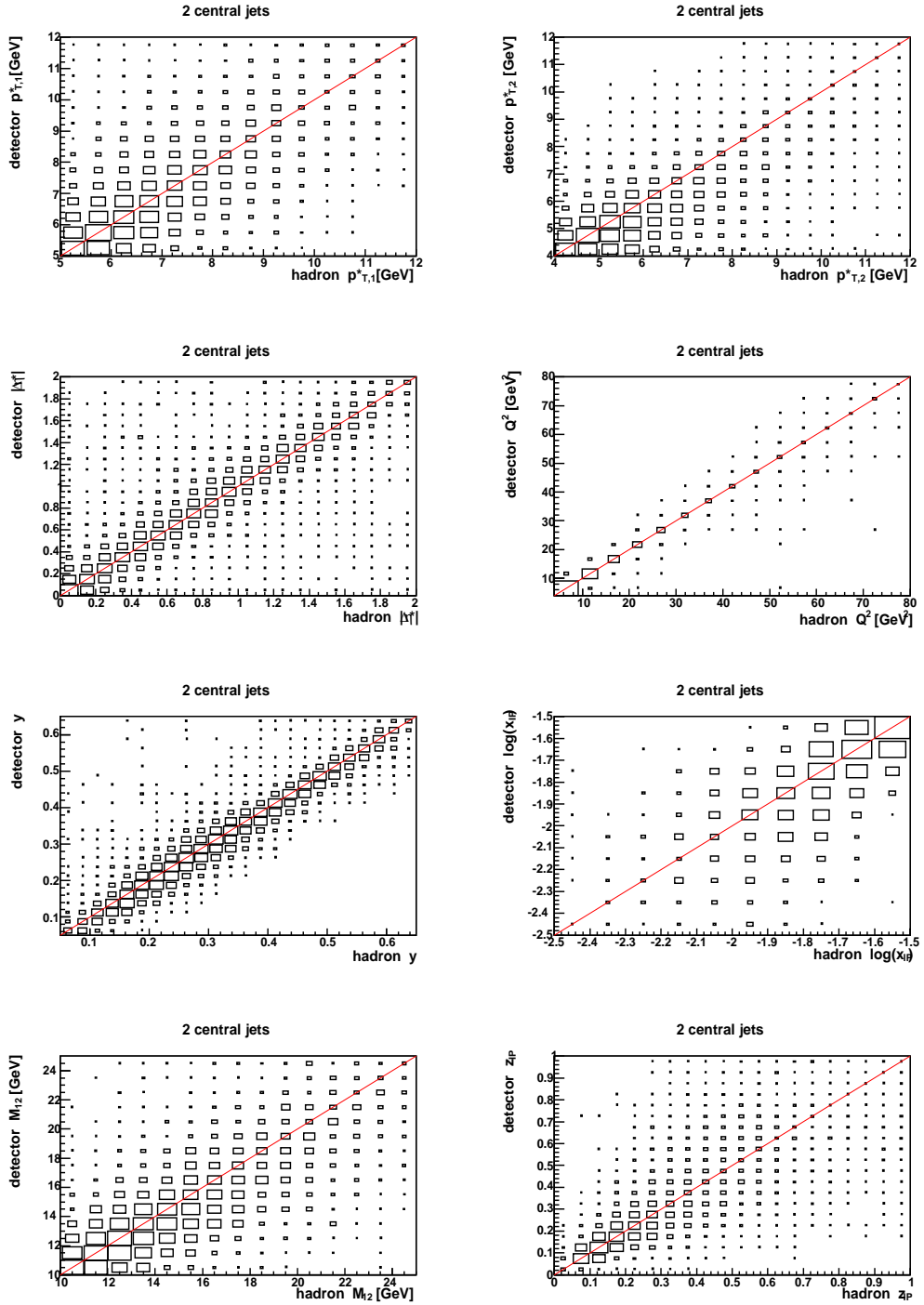
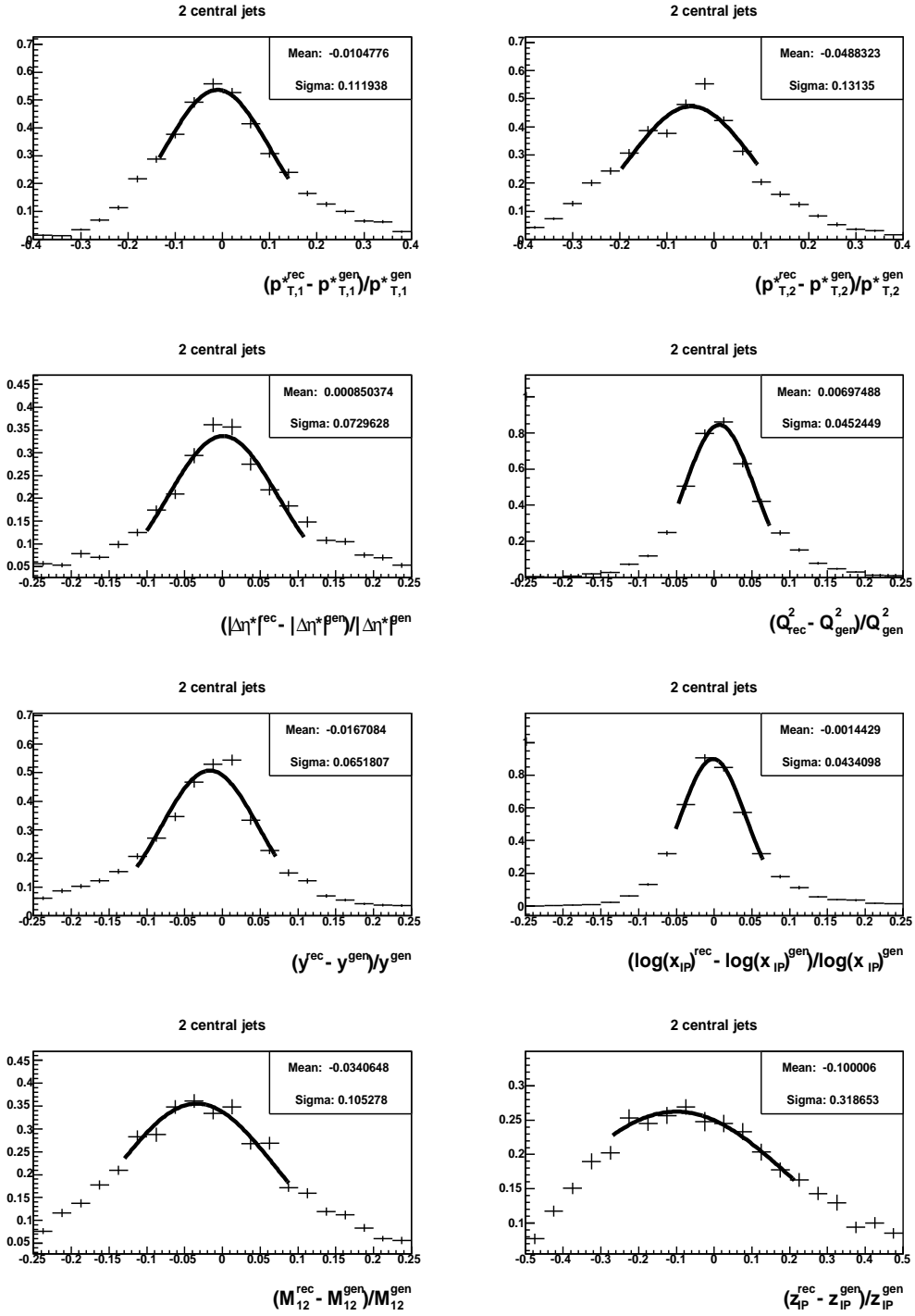Figure 7.1: The correlation plots for the "2 central jet" topology.

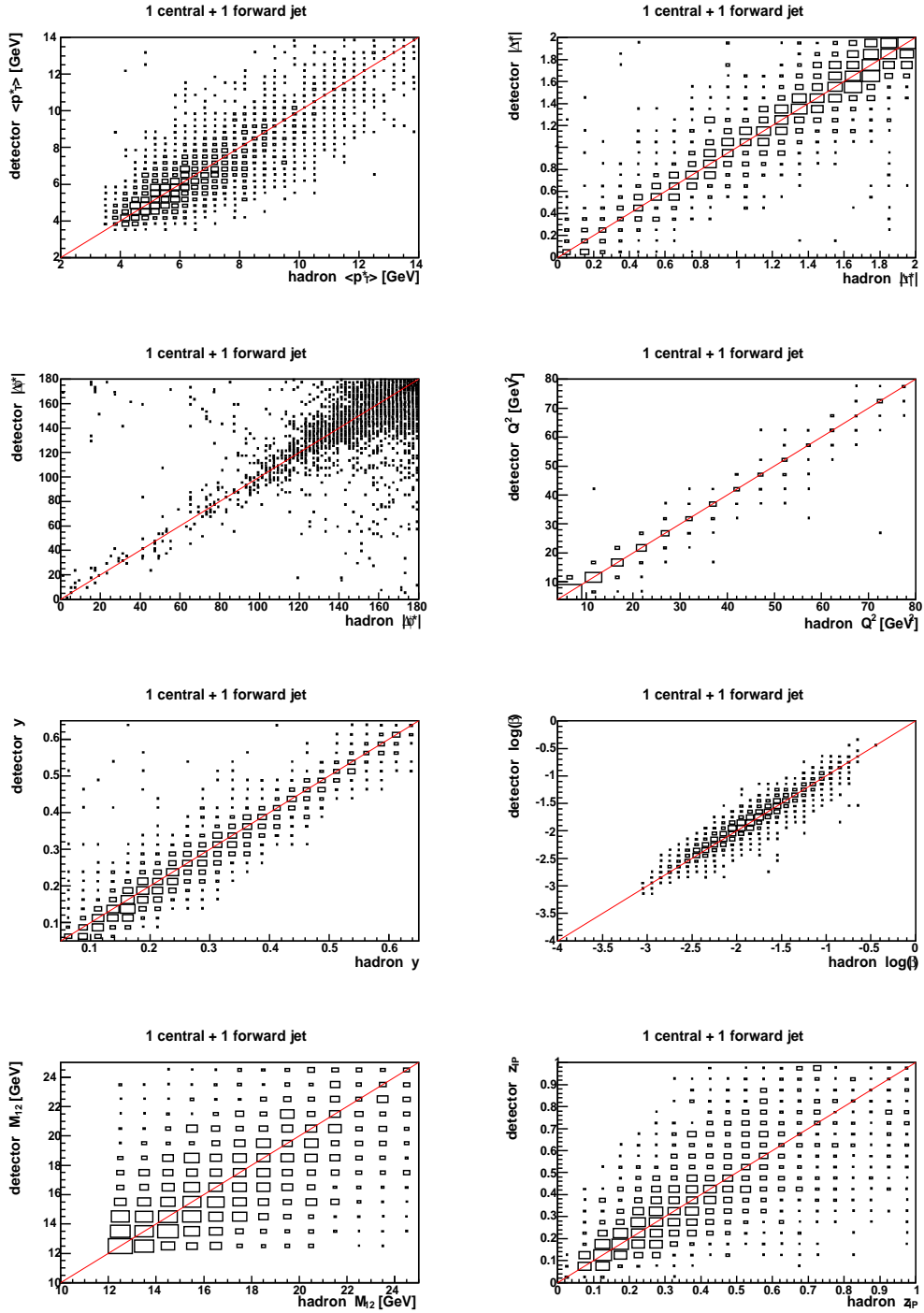Figure 7.2: The detector-hadron level resolution plots for the "2 central jet" topology.

Figure 7.3: The correlation plots for the "1 central + 1 forward jet" topology.
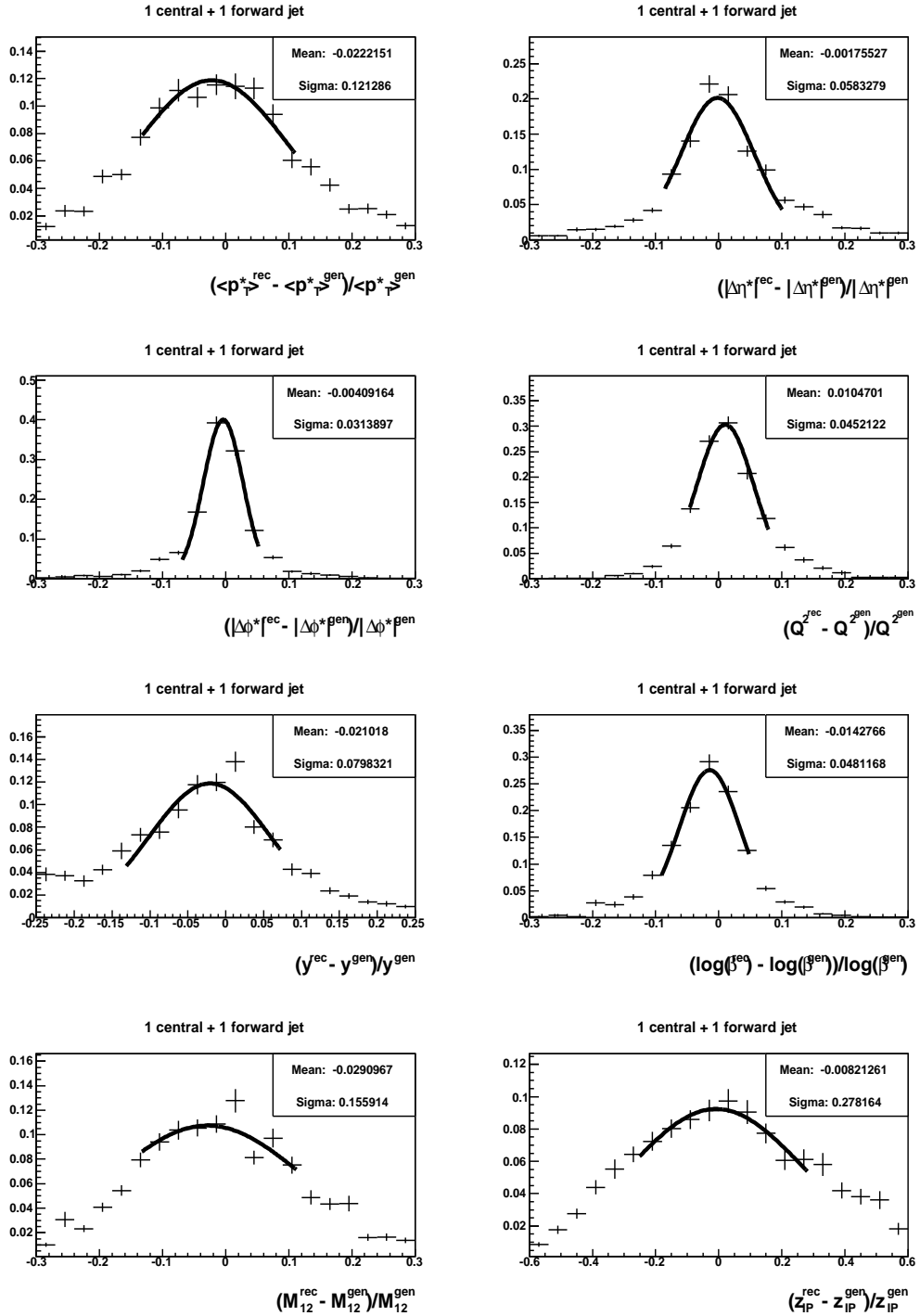
Figure 7.4: The detector-hadron level resolution plots for the "1 central + 1 forward jet" topology.
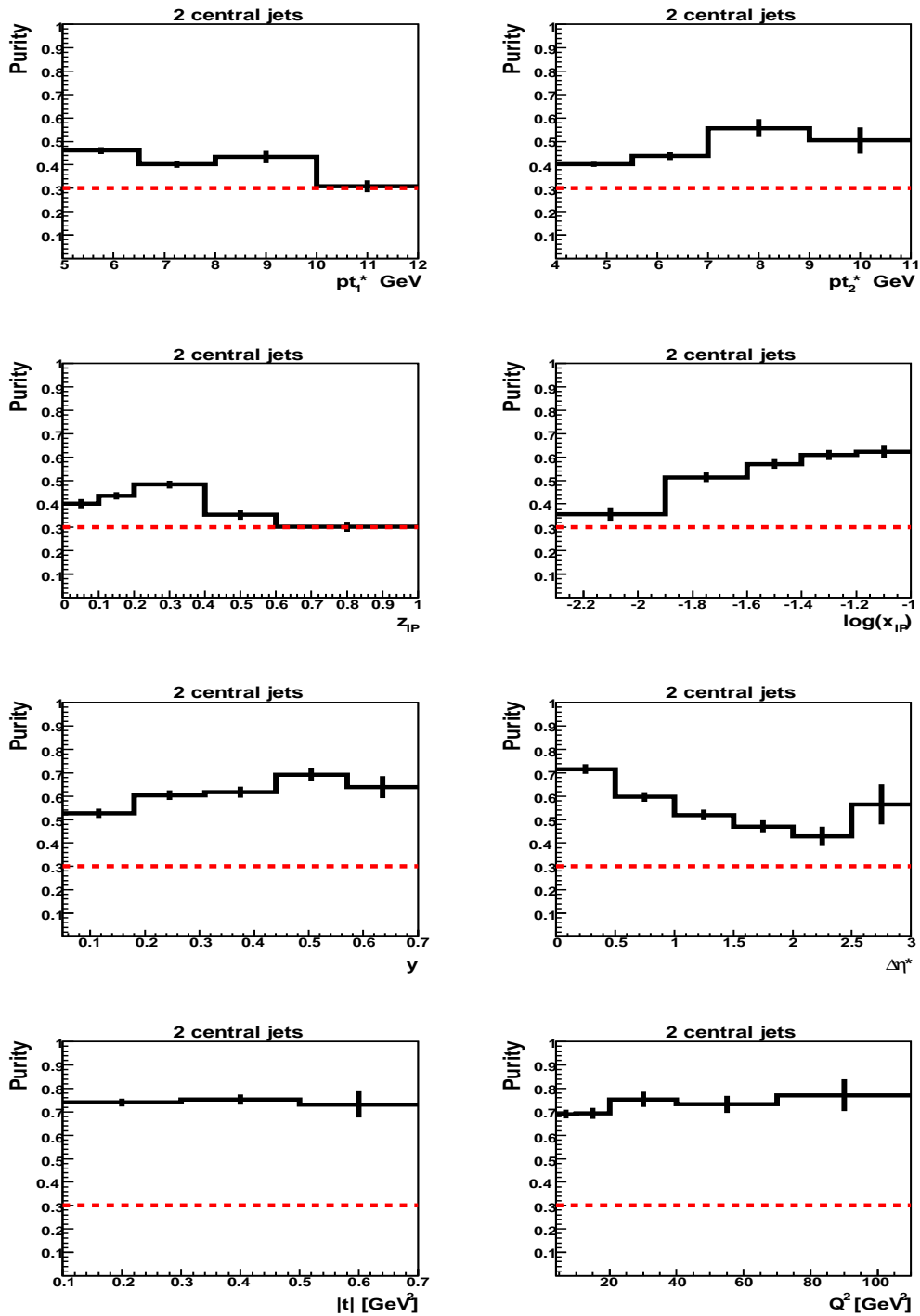
Figure 7.5: The purity for the "2 central jet" topology. The dashed line stands for the minimum required purity of 30%.
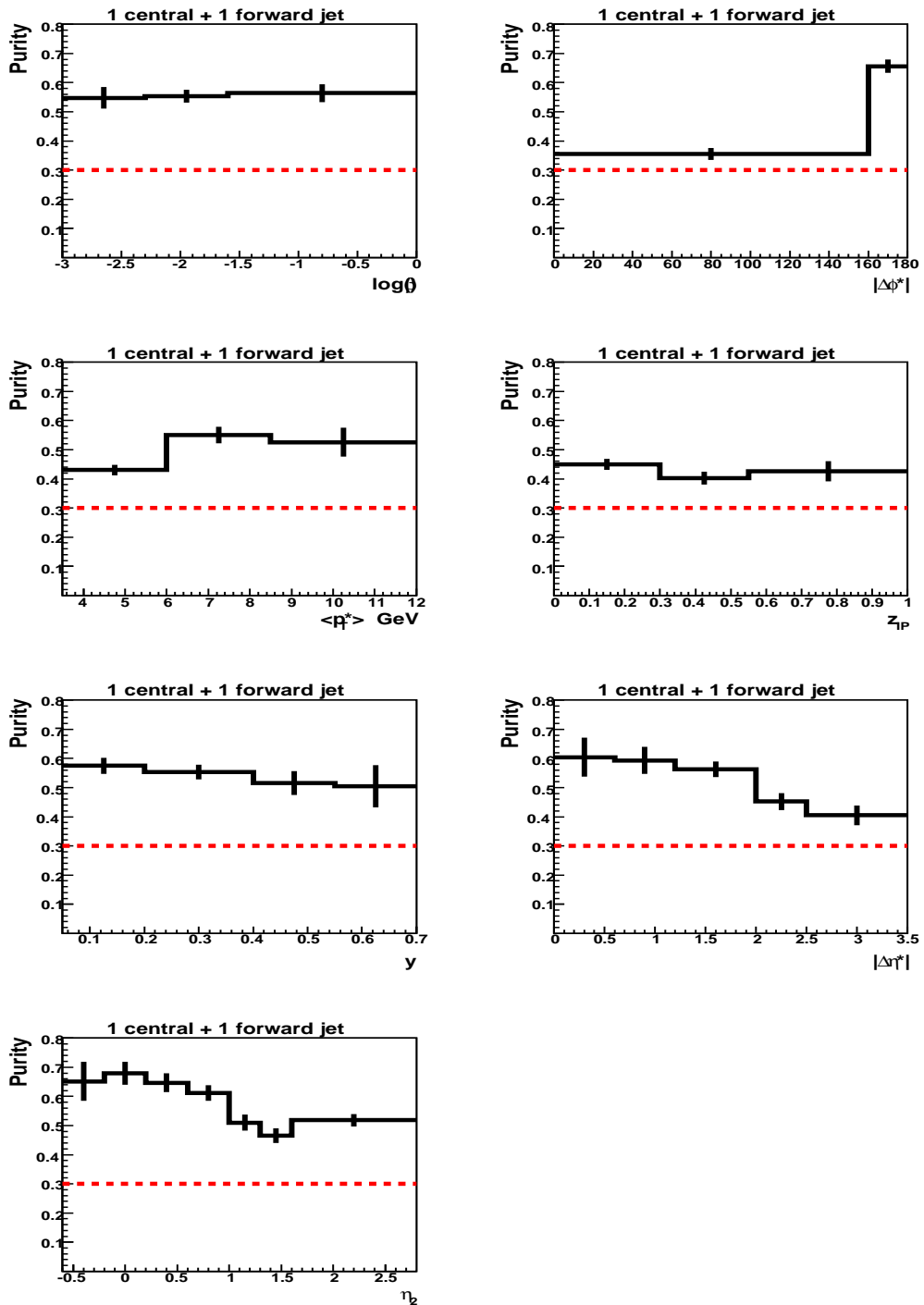
97

Figure 7.6: The Purity for the "1 central + 1 forward jet" topology. The dashed line stands for the minimum required purity of 30%.
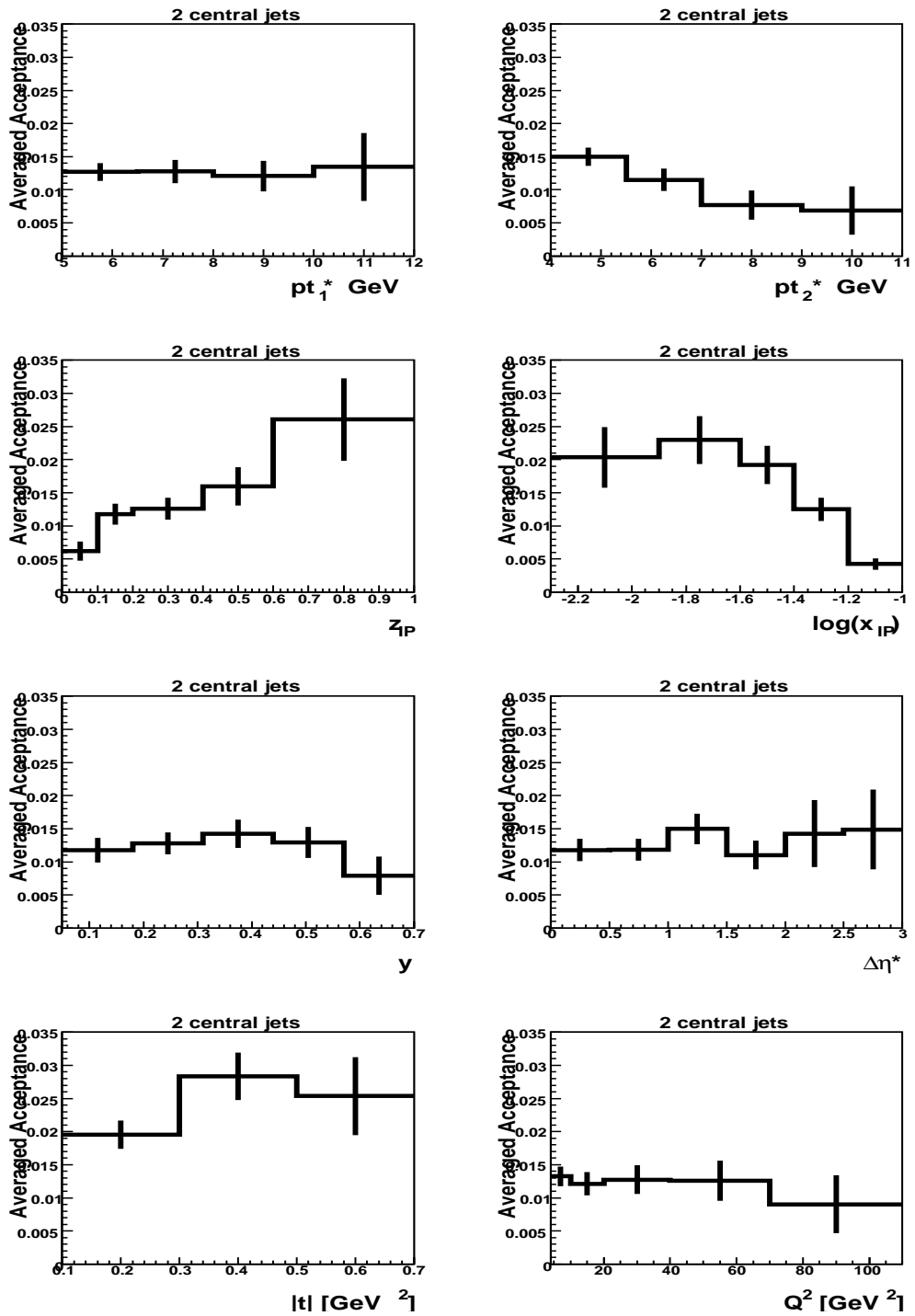
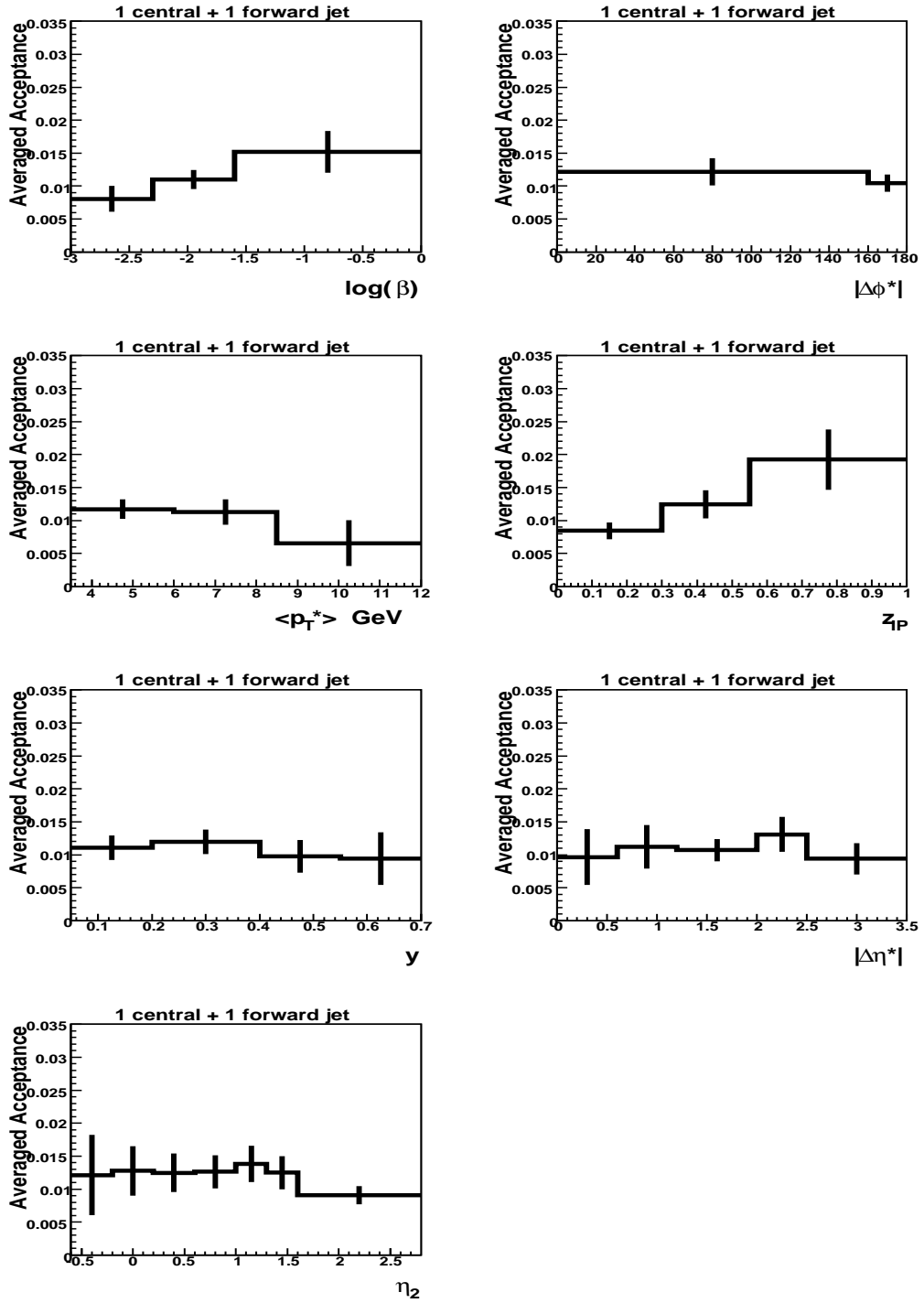Figure 7.7: The Averaged Acceptance for the "2 central jet" topology.

Figure 7.8: The Averaged Acceptance for the "1 central + 1 forward jet" topology.

worse resolution of jet transverse momentum and of $z_{I\!P}$ in comparison to kinematical and diffractive variables is reflected in lower purities for that particular distributions. The purities are presented in the Figs. 7.5 and 7.6.

For the detector to hadron level corrections, combined H1 and FPS acceptance is calculated as follows:

$$\mathcal{A} = \frac{N_{rec}^i}{N_{gen}^i}, \tag{7.5}$$

where N_{rec}^i stands for number of reconstructed events and N_{gen}^i for the number of generated events for every run period and bin i. In Figs. 7.7 and 7.8 the acceptance combined over all five running periods as:

$$\mathcal{A}_{Averaged} = \frac{\sum_{i=05e1}^{07p} N_{corr}^i}{\sum_{i=05e1}^{07p} \frac{N_{corr}^i}{\mathcal{A}^i \cdot \mathcal{E}_{FPStrack}^i}}. \tag{7.6}$$

is presented. Since the statistics of the measured data is included in the definition of the averaged acceptance, the errors in Figs. 7.7 and 7.8 correspond to the statistical error of the data. The average error of the acceptance which is used in the calculation of the cross section (See Eq. 7.5) is $\sim 2\%$. The low value of the acceptance is caused by the low geometrical and kinematical acceptance of the FPS detector.

7.4 Radiative Corrections

The effect of the initial and final state QED radiation which should not bias the final measurement is taken into account by estimating the ratio

$$C_i^{Rad} = \left(\frac{\sigma^{NoRad}}{\sigma^{Rad}} \right)_i \tag{7.7}$$

for every bin i. The cross sections are obtained at the level of stable hadrons from `RAPGAP` Monte Carlo (See Sec. 5.1.1) generated within same kinematical limits with and without QED radiation. The radiative corrections are presented in Figs. 7.9 and 7.10. The correction factors do not depend in general on the kinematical variables, except for the y and Q^2 variables, where the measurement of the scattered electron plays a crucial role in the calculation. The average value of the radiative corrections is $\sim 5\%$. The correction factors are estimated and applied for each bin of the measured cross sections.

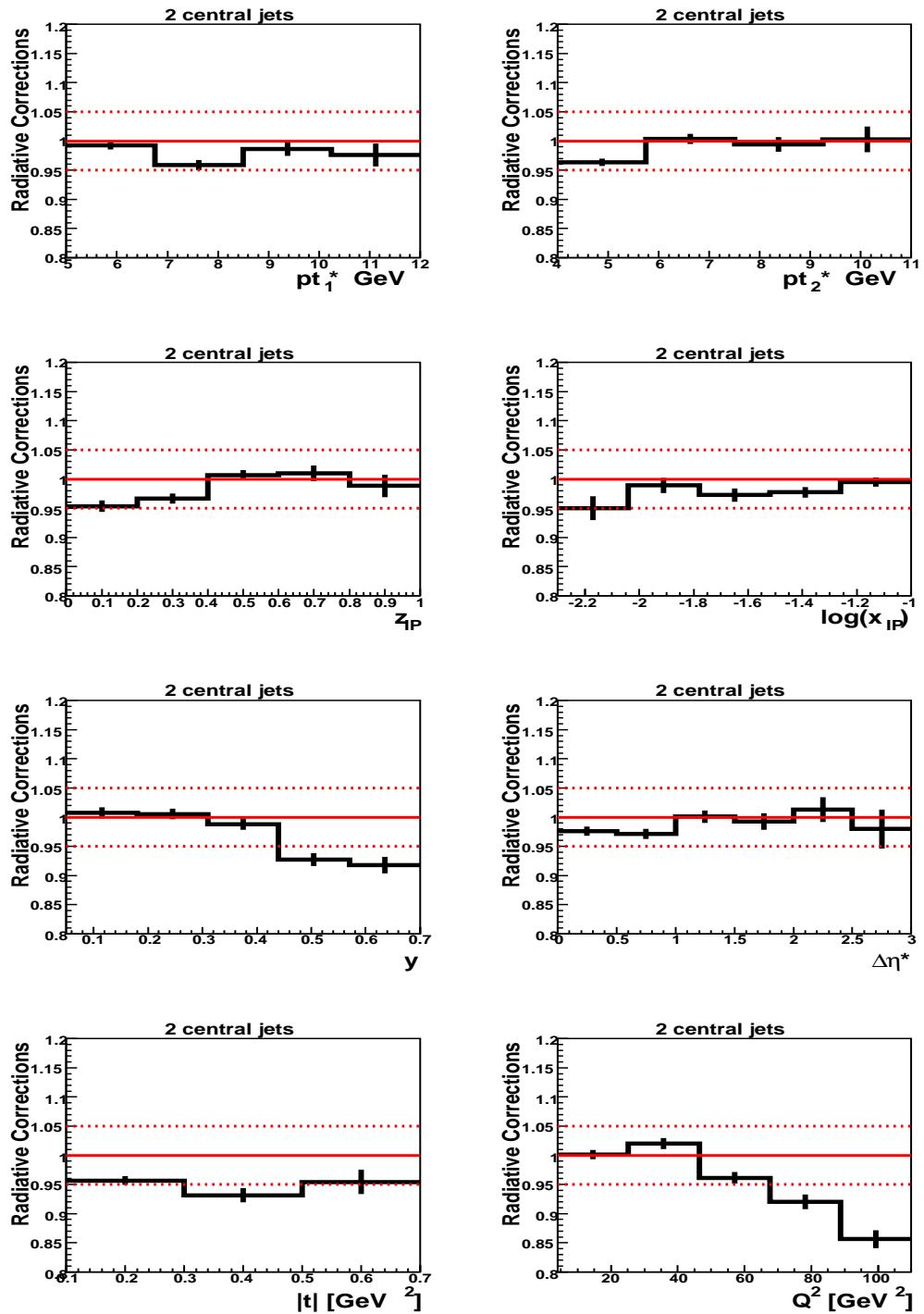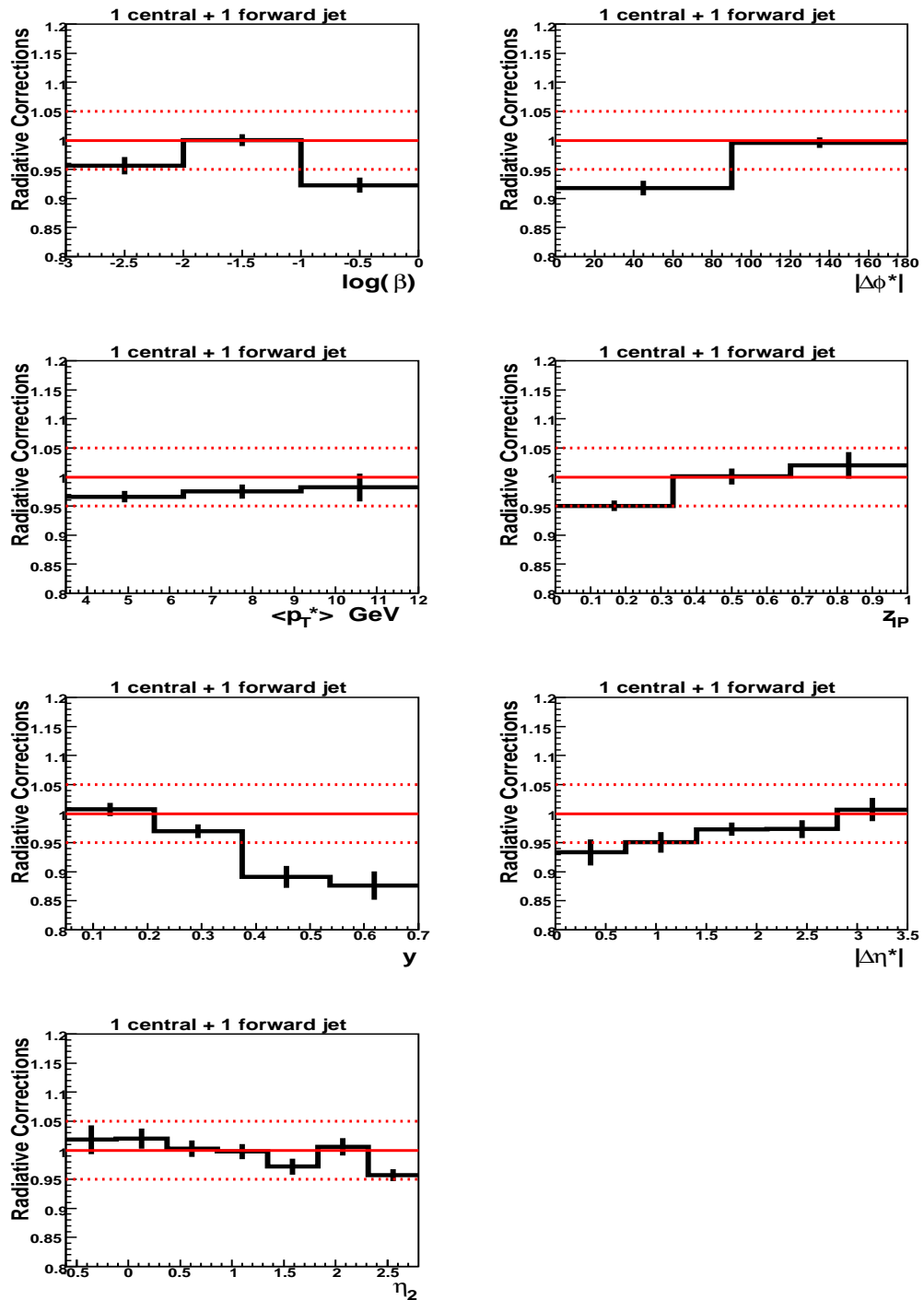Figure 7.9: The radiative corrections for the "2 central jet" topology. The dashed lines stand for the ±5% band.

Figure 7.10: The radiative corrections for the "1 central + 1 forward jet" topology. The dashed lines stand for the ±5% band.

7.5 Hadronisation Corrections

The measured cross sections will be presented at the level of stable hadrons. The NLO QCD calculations are performed on the parton level, therefore the effect of the hadronisation has to be taken into account. In order to extract the hadronisation corrections defined as

$$1 + \delta_{hadr} = \frac{\sigma_{hadron}}{\sigma_{parton}} \tag{7.8}$$

for every bin as a ratio of the cross section at the hadron level (σ_{hadron}) to the cross section at the parton level (σ_{parton}) a Monte Carlo model with a good hadron parton level correspondence has to be used. The Fig. 7.11 and 7.13 present the two dimensional correlation plots for both jet topologies, Fig. 7.12 and 7.14 present the hadron parton resolution plots.

Since in the `RAPGAP` MC generator is implemented only one fragmentation model (Lund String Model [28]) for hadronisation and no other diffractive Monte Carlo is available for ep interactions, a `RAPGAP` MC set has been used with the parton showers modelled with the colour dipole model (see Sec. 5.1.1). The acceptable agreement of this model with the data on the reconstructed level has been presented in Sec. 6.11.2.

In order to estimate the hadronisation corrections correctly, the parton level cross section of the Monte Carlo must be in a good agreement with the NLO QCD cross section obtained from the `nlojet++` program. The reweighted distributions of the LLPS MC and CDM MC to the QCD predictions are presented in the Figs. 7.15, 7.16. The reweighting has been done for two different DPDFs "H1 2006 Fit B" and "H1 2007 Jets".

In Figs. 7.17-7.20 the hadronisation corrections obtained with LLPS and CDM `RAPGAP` MC reweighted to the NLO QCD predictions are presented. The average difference between the two samples of hadronisation corrections is $\sim 10\%$, the biggest difference $\sim 20\%$ is in the region of phase space characterised by low Q^2, low p_T^* and high $x_{I\!\!P}$. In the following the average of LLPS and CDM hadronisation corrections (as shown in Figs. 7.17-7.20) will be used for the corrections of the NLO QCD calculations to the hadron level.

For estimation of the uncertainties of the corrections the biggest difference between the averaged values and both values in every bin is calculated. The average uncertainties are $\sim 7\%$. These errors are combined in quadrature with the errors caused by the scale uncertainties of the NLO QCD corrections.
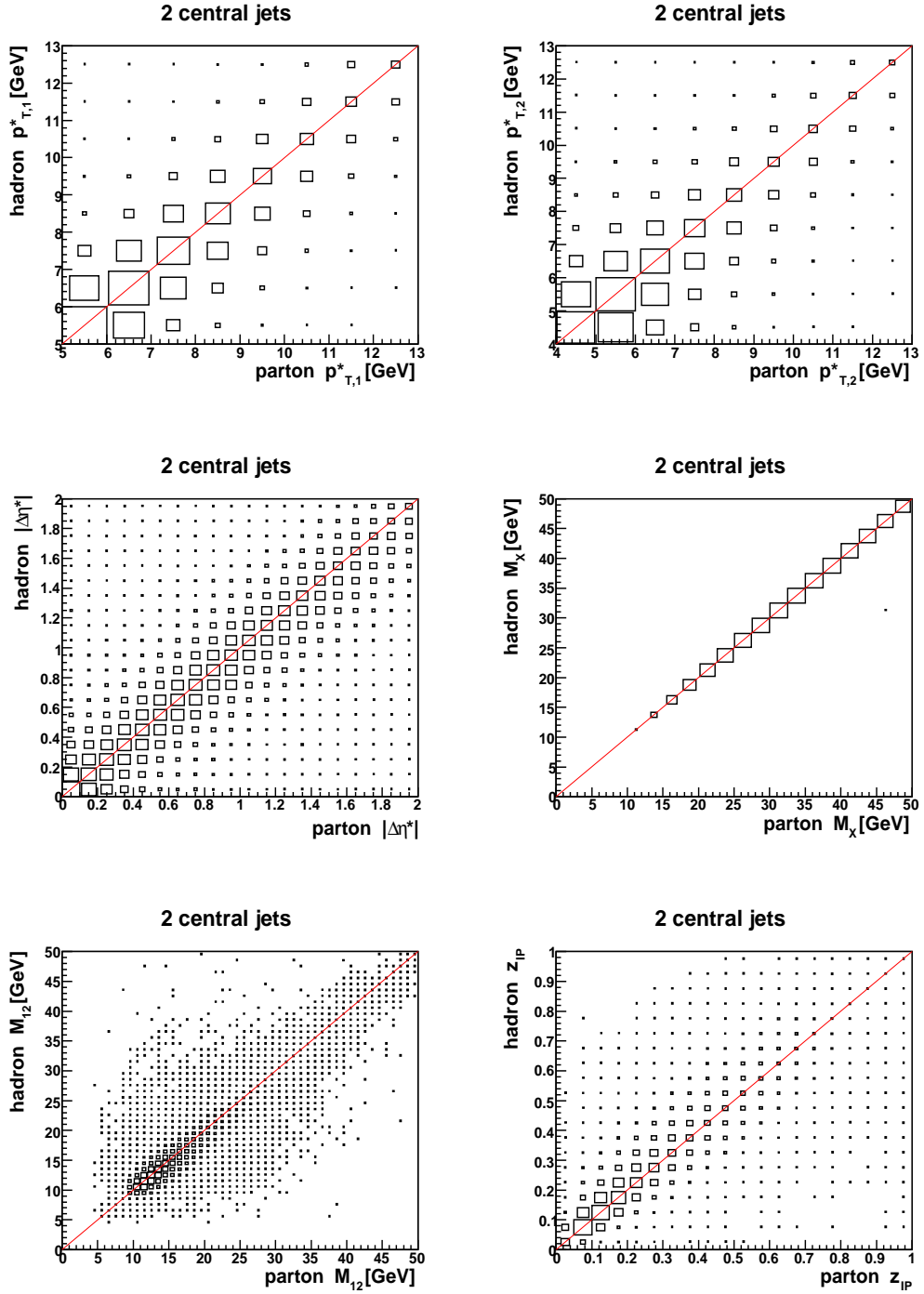
Figure 7.11: The hadron parton level correlation plots for the "2 central jet" topology.
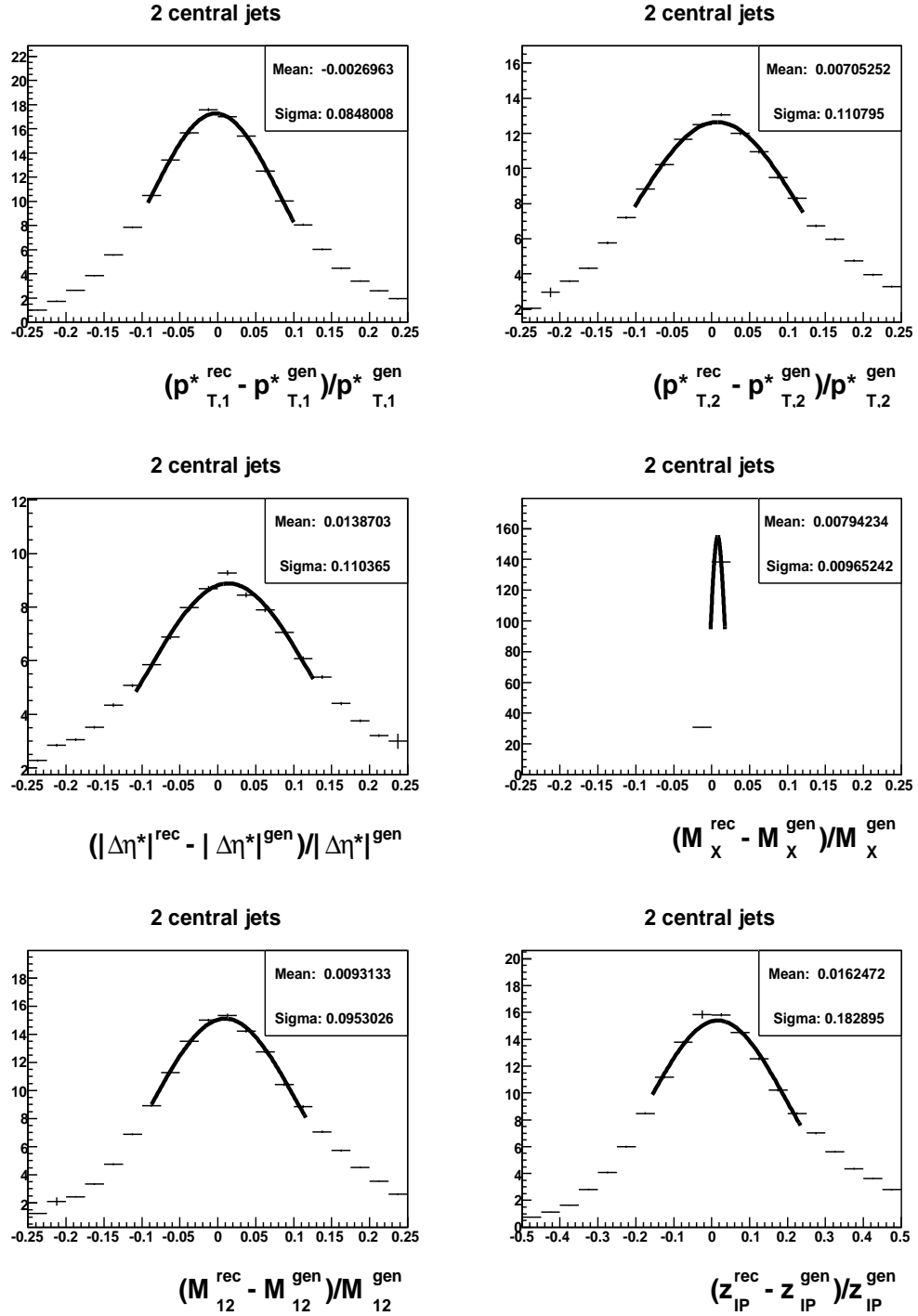
Figure 7.12: The parton-hadron resolution plots for the "2 central jet" topology.
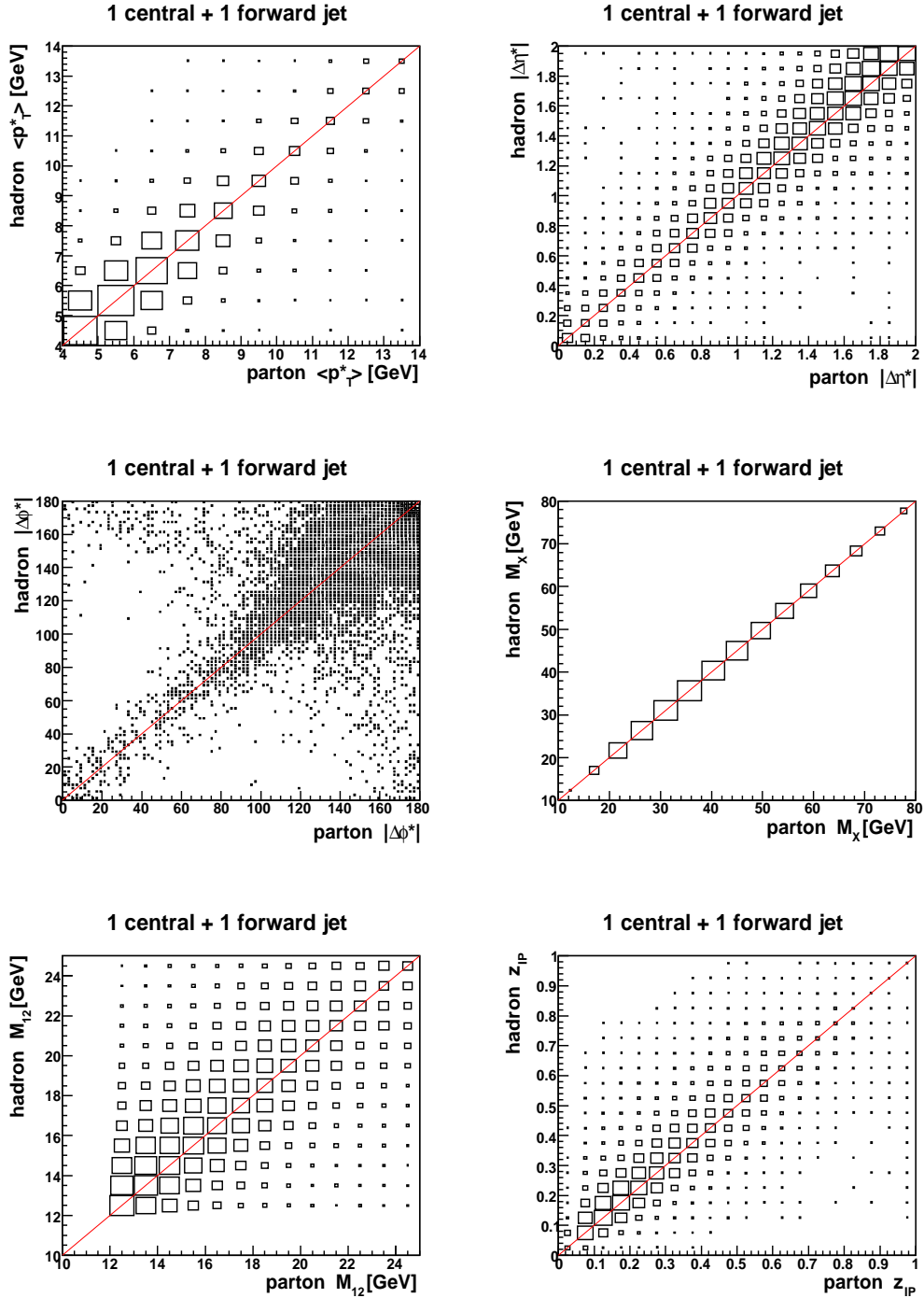
Figure 7.13: The hadron parton level correlation plots for the "1 central + 1 forward jet" topology.

1 central + 1 forward jet

Mean: -0.00263929

Sigma: 0.083728

$(<p^*_T>^{rec} - <p^*_T>^{gen})/<p^*_T>^{gen}$

1 central + 1 forward jet

Mean: 0.0223163

Sigma: 0.0871835

$(|\Delta\eta^*|^{rec} - |\Delta\eta^*|^{gen})/|\Delta\eta^*|^{gen}$

1 central + 1 forward jet

Mean: -0.00104641

Sigma: 0.0492944

$(|\Delta\phi^*|^{rec} - |\Delta\phi^*|^{gen})/|\Delta\phi^*|^{gen}$

1 central + 1 forward jet

Mean: 0.00876387

Sigma: 0.0121735

$(M_X^{rec} - M_X^{gen})/M_X^{gen}$

1 central + 1 forward jet

Mean: 0.0124203

Sigma: 0.097674

$(M_{12}^{rec} - M_{12}^{gen})/M_{12}^{gen}$

1 central + 1 forward jet

Mean: 0.0237039

Sigma: 0.197804

$(z_{IP}^{rec} - z_{IP}^{gen})/z_{IP}^{gen}$
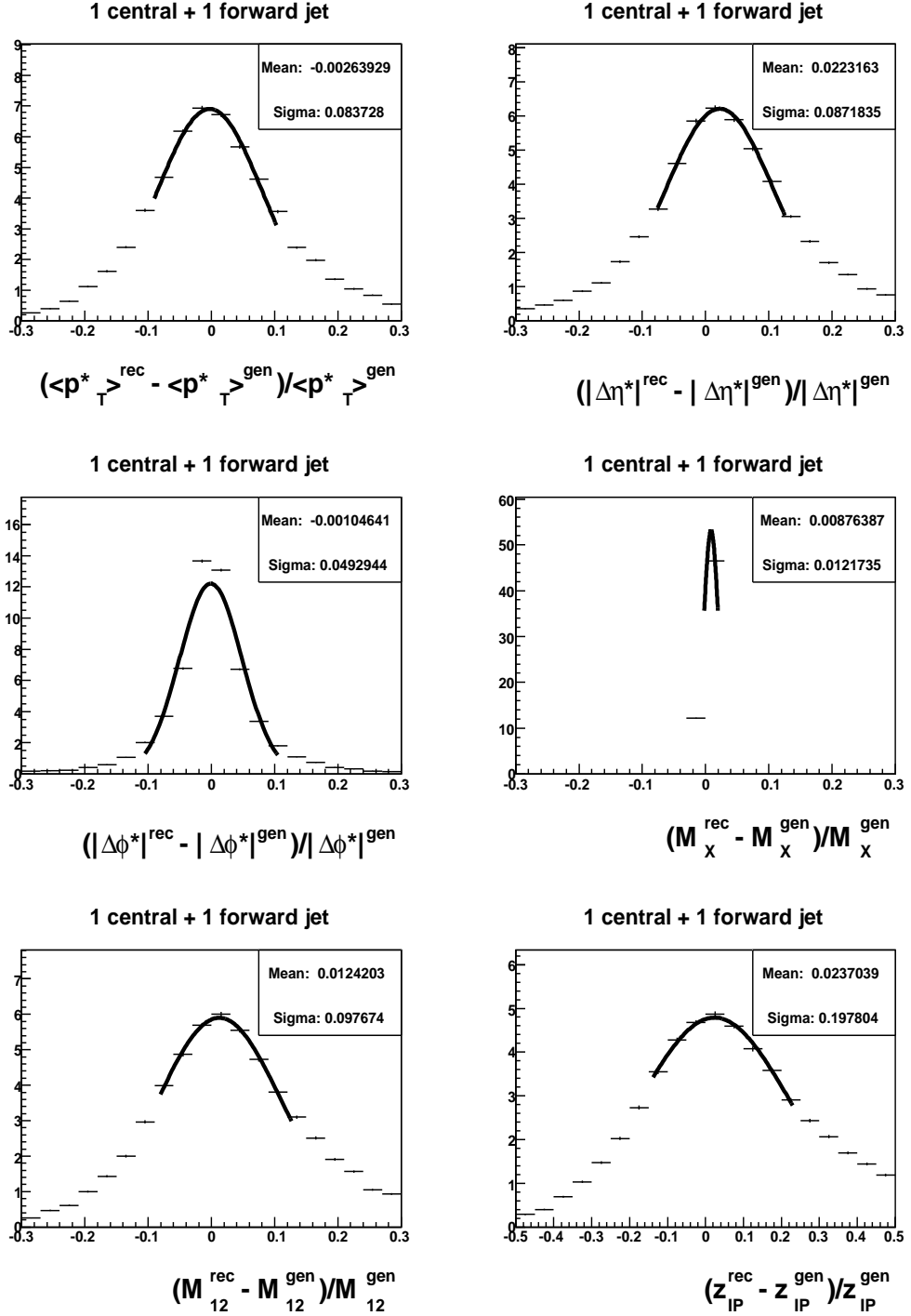
Figure 7.14: The parton-hadron resolution plots for the "1 central + 1 forward jet" topology.

Figure 7.15: Comparison of the reweighted `RAPGAP` MC on the parton level to the NLO QCD predictions based on DPDFs "H1 2006 Fit B" and "H1 2007 Jets" for the "2 central jets" topology.
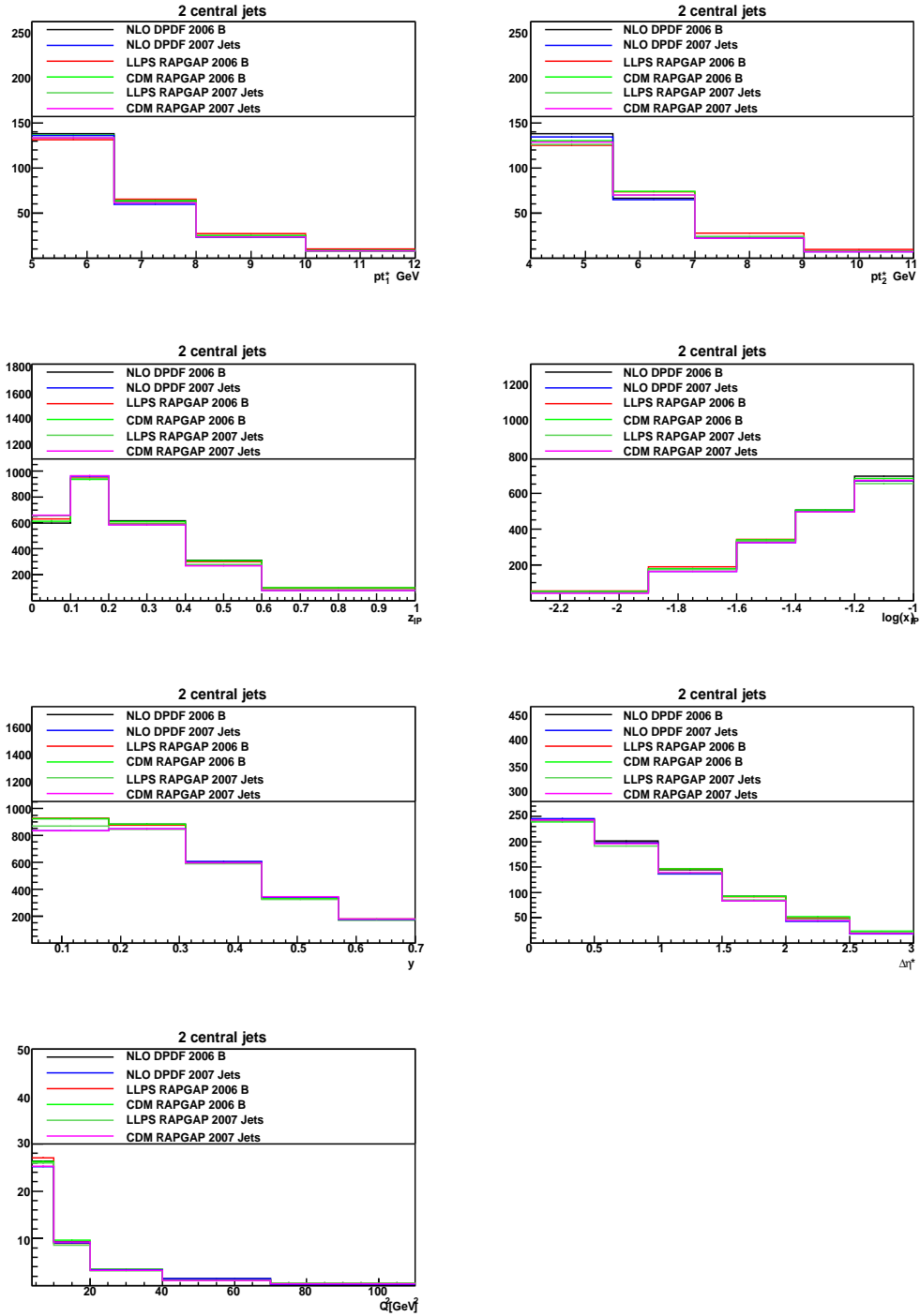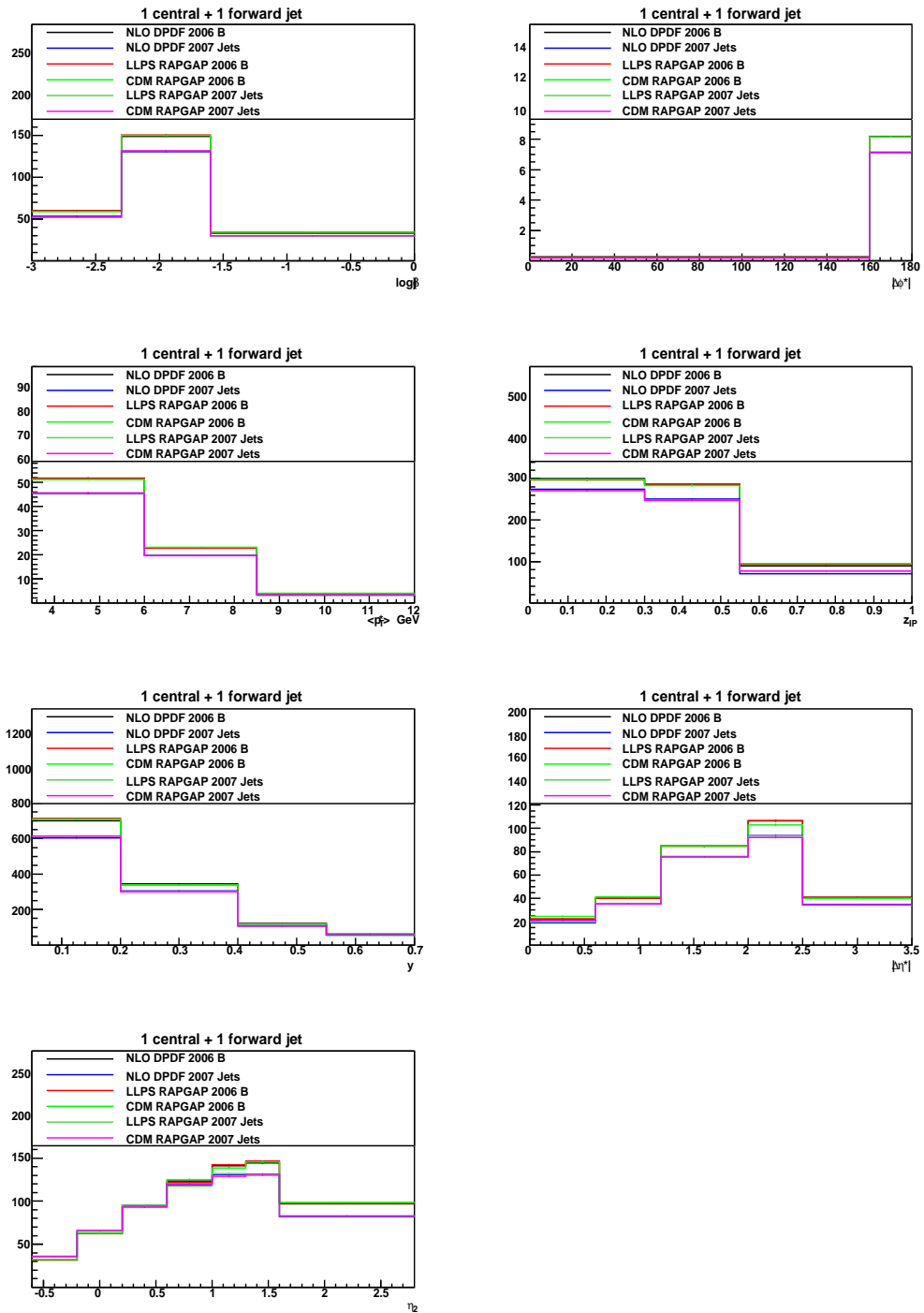
Figure 7.16: Comparison of the reweighted `RAPGAP` MC on the parton level to the NLO QCD predictions based on DPDFs "H1 2006 Fit B" and "H1 2007 Jets" for the "1 forward + 1 central jet" topology.

Figure 7.17: Hadronisation corrections for the set reweighted to the DPDF "H1 2006 Fit B" for the "2 central jets" topology.

Figure 7.18: Hadronisation corrections for the set reweighted to the DPDF "H1 2006 Fit B" for the "1 central + 1 forward jet" topology.

Figure 7.19: Hadronisation corrections for the set reweighted to the DPDF "H1 2007 Jets" for the "2 central jets" topology.

Figure 7.20: Hadronisation corrections for the set reweighted to the DPDF "H1 2007 Jets" for the "1 central + 1 forward jet" topology.
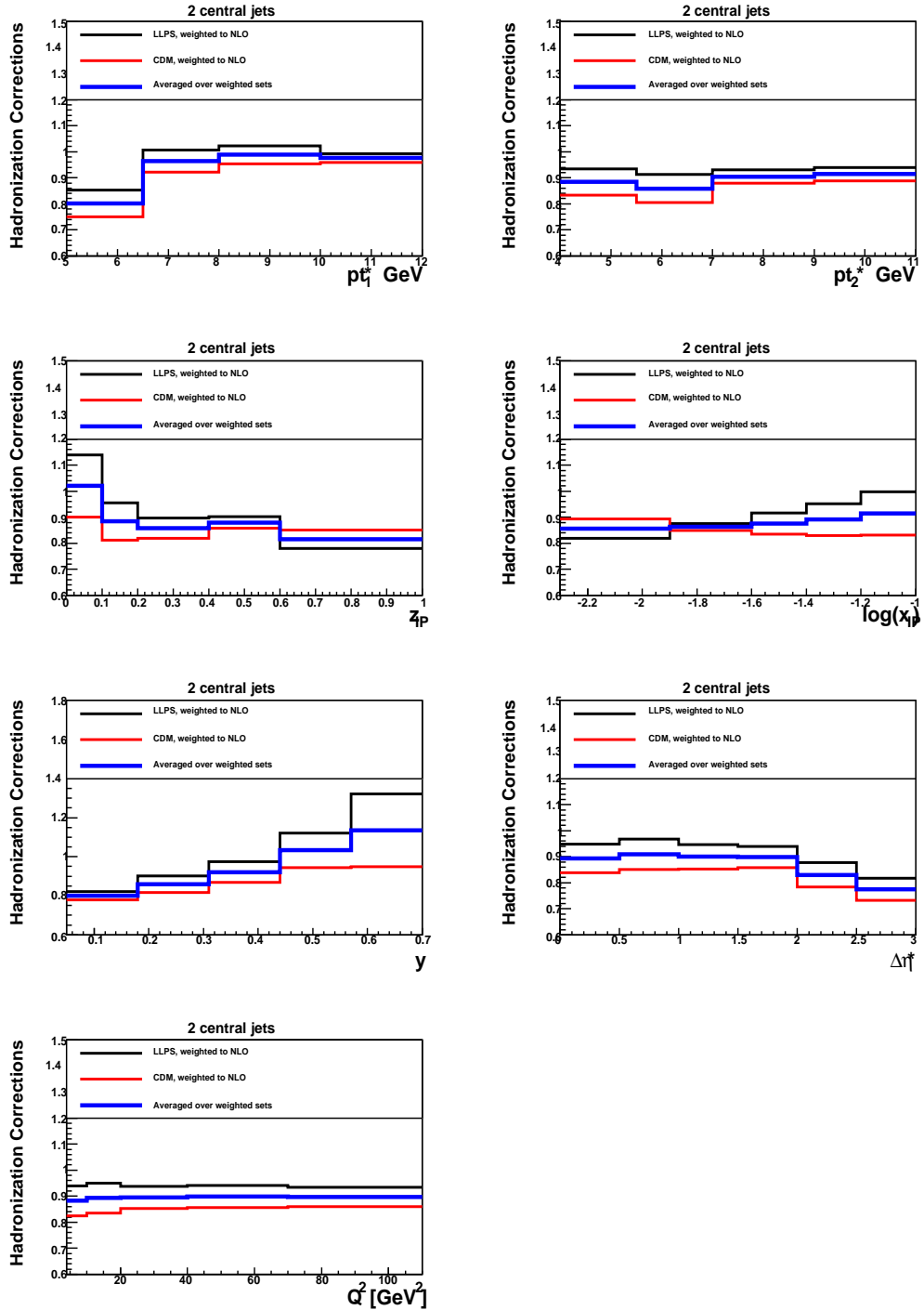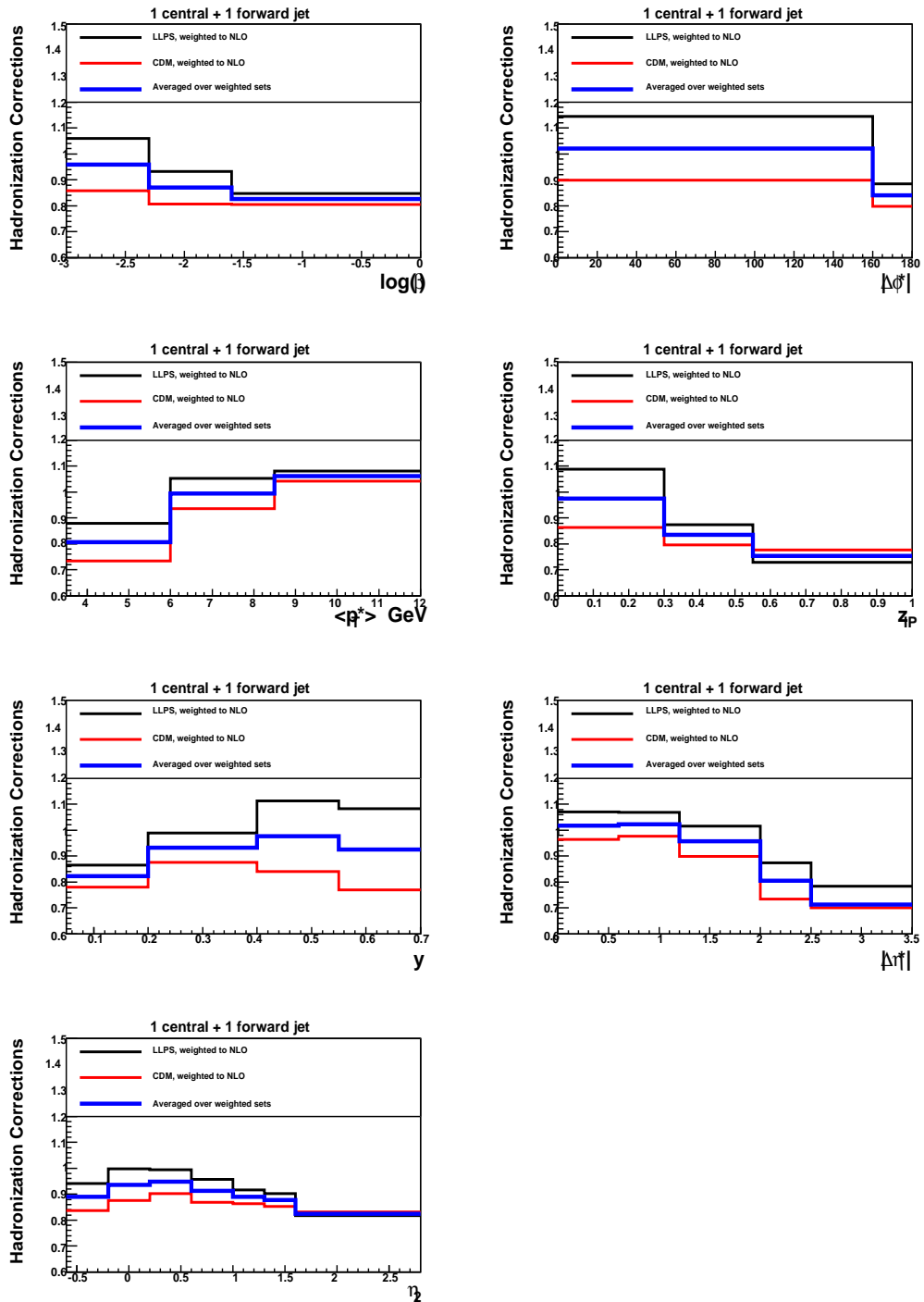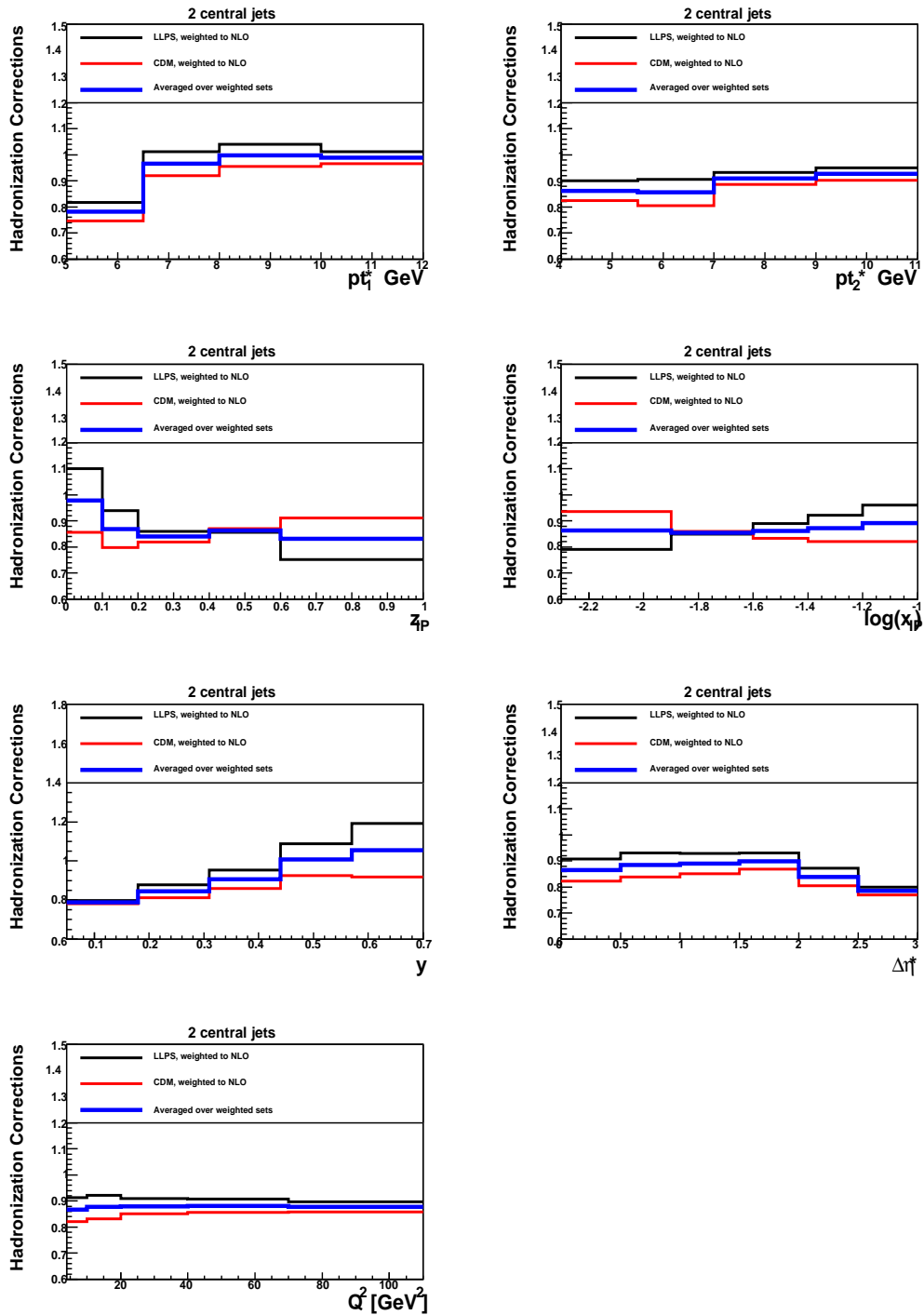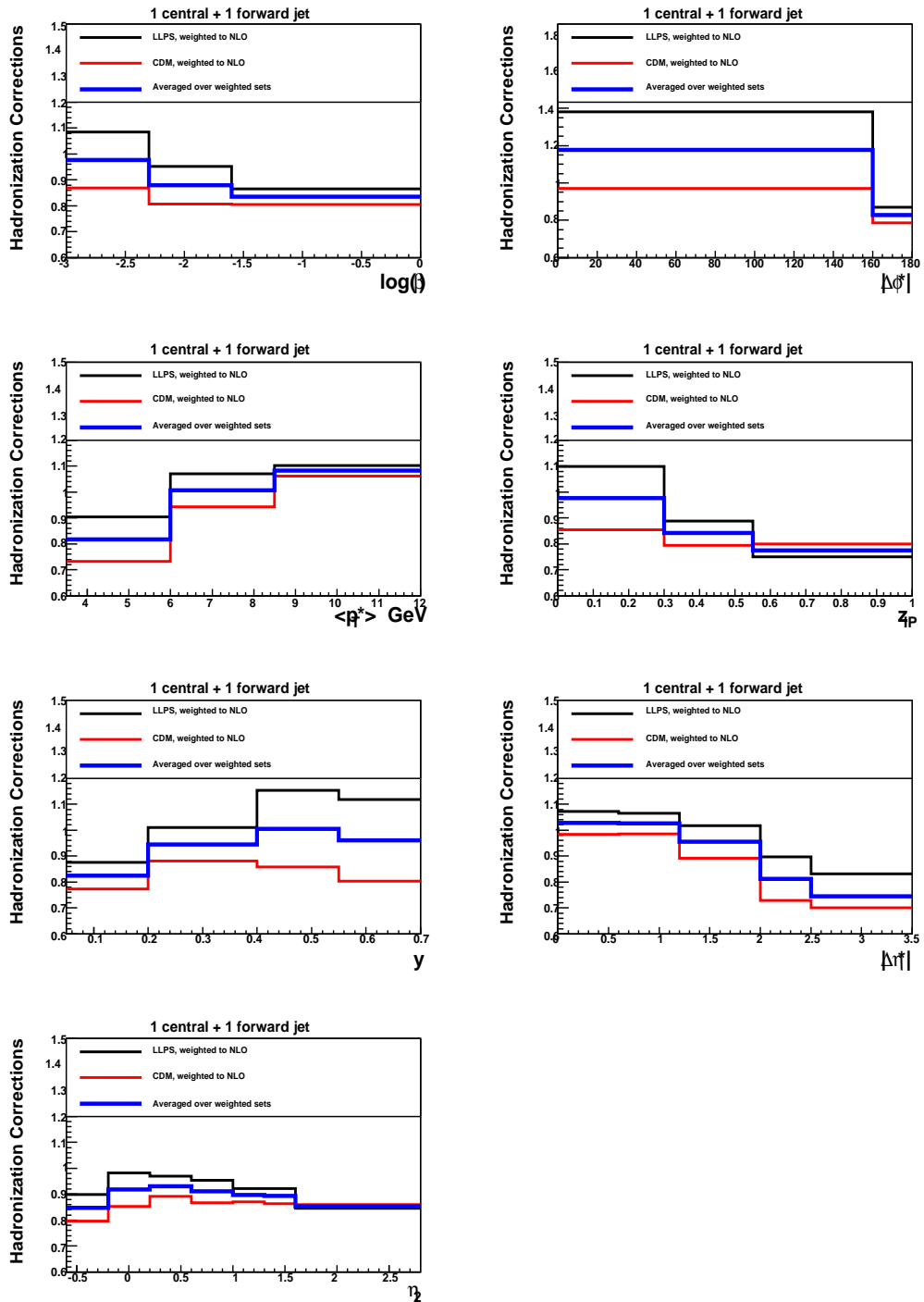
7.6 Systematic Errors

The detector effects are responsible for emerging of additional uncertainties and cannot be minimised by enlarging the statistical sample. These systematical errors propagate to the acceptance estimation and influence the cross section measurement. The systematic errors are estimated using Monte Carlo models. Different sources of systematic errors are treated independently. For every bin, the systematic error is obtained as the biggest difference between the cross section obtained with the shifted kinematical variables and the nominal cross section.

7.7 Uncorrelated Errors

The uncorrelated systematic errors are related to the scattered electron and proton measurement, to the uncertainties of the description of the data by the signal Monte Carlo, the uncertainty in the hadronic final state energy measurement and the subtraction of the halo background. The general procedure is to modify the particular variable, recalculate the whole event kinematics and estimate the influence of that shift on the cross section. A detailed description of individual shifts follows:

- The measurement of the scattered electron is very precise. A systematic shift of $\pm 1\%$ has been applied on the electron energy and $\pm 1 \ mrad$ on the electron angle.

- The systematic shifts applied on the scattered proton variables result from the FPS detector resolution. The energy of the proton has been shifted by $\pm 1 \ GeV$, the X coordinate of the momentum by $\pm 0.01 \ GeV$ and the Y coordinate by $\pm 0.03 \ GeV$.

- The iterative calibration of the hadronic final state has been described in Section 6.3. From the double ratio of p_T-balances the 2 % uncertainty on the energy of the hadronic final state was estimated. This systematic error is one of the dominant errors in this measurement, since the jet analysis is very sensitive to energy shifts of the hadronic final state particles. Due to the low cut on the transverse energy of the jets the systematic shift has a significant influence on the number of events which pass the cuts.

- The systematic error on the subtraction of the $E + Pz$ background is estimated in two ways. The "vertical" procedure shifts the integral above the $E+Pz$ cut by $\pm 1/\sqrt{N_{Signal\ above\ E+Pz\ cut}}$, which is then used in the subtraction method for estimation of two new sets of background subtraction constants. The "horizontal" procedure shifts the non-diffractive background

which is convoluted with the beam-halo protons. The shift is defined as $(E + Pz)_{Shifted} = 2 \cdot (E'_p(FPS) \pm 1\ GeV) + (1.00 \pm 0.02) \cdot (E + Pz)(HFS)$, the systematic shifts of FPS proton energy and HFS Energy are defined above. In this way, two new shifted $E + Pz$ distributions are obtained and fitted to the signal distribution in order to obtain two new sets of background subtraction constants.

- The detector to hadron level corrections are dependent on the Monte Carlo model which is used. Therefore the systematic error estimated for the model uncertainty plays an important role in the systematic error estimation. The systematic error originates from the uncertainty of the DPDF and from the requirement of description of the data by MC within the statistical errors of the data. The following weights have been used independently on the generator level in order to describe the data by the Monte Carlo model within the statistical errors of the data:

  - $x_{I\!\!PA}^{\pm 0.05}$
  - $\beta^{\pm 0.1}(1 - \beta)^{\mp 0.1}$
  - $\log^{\pm 0.1}(Q^2)$
  - $\exp(\pm \Delta t)$, where Δ stands for the error of the exponential fit to the t-distribution. The value is 0.4.
  - $p_T^{\pm 0.1}$ for the "2 central dijet" selection, $p_T^{\pm 0.15}$ for the "1 central + 1 forward jet" selection. The higher uncertainty for the second topology is due to the lower p_T cuts applied on the jets, the migrations of generated events below the p_T cut are increasing with decreasing value of the p_T cut.

The errors arising from different sources of the model systematics are combined in quadrature and presented in Fig. 7.21. The statistical errors are comparable with the size of the data points. The measured data with statistical fluctuations are sufficiently described by the MC with model systematic uncertainties.

7.8 Correlated Uncertainties

The normalisation error has three sources: the uncertainty of the luminosity measurement, the FPS track reconstruction efficiency and the s112 sub-trigger systematic error.

7.9 Systematic Error Summary

Following table summarises the applied systematic shifts and its effects on the cross section in the two topologies:

systematic shift	value	"2 central jets"	"1 central + 1 forward"
E'_e	1%	0.3%	0.1%
θ_e	1 $mrad$	1.2%	1.1%
E'_p	1 GeV	0.1%	0.4%
p'_X	0.01 GeV	5.3%	4.4%
p'_Y	0.03 GeV	1.6%	2.3%
$E + Pz$	"vert"	0.5%	0.5%
$E + Pz$	"hor"	1.3%	1.0%
E_{HFS}	2%	6.9%	8.7%
Model	$p_T, x_{I\!P}, t, \beta, Q^2$	7.6%	11.6%
Total		11.7%	15.4%

Table 7.1: Uncorrelated Systematic Shifts Summary Table

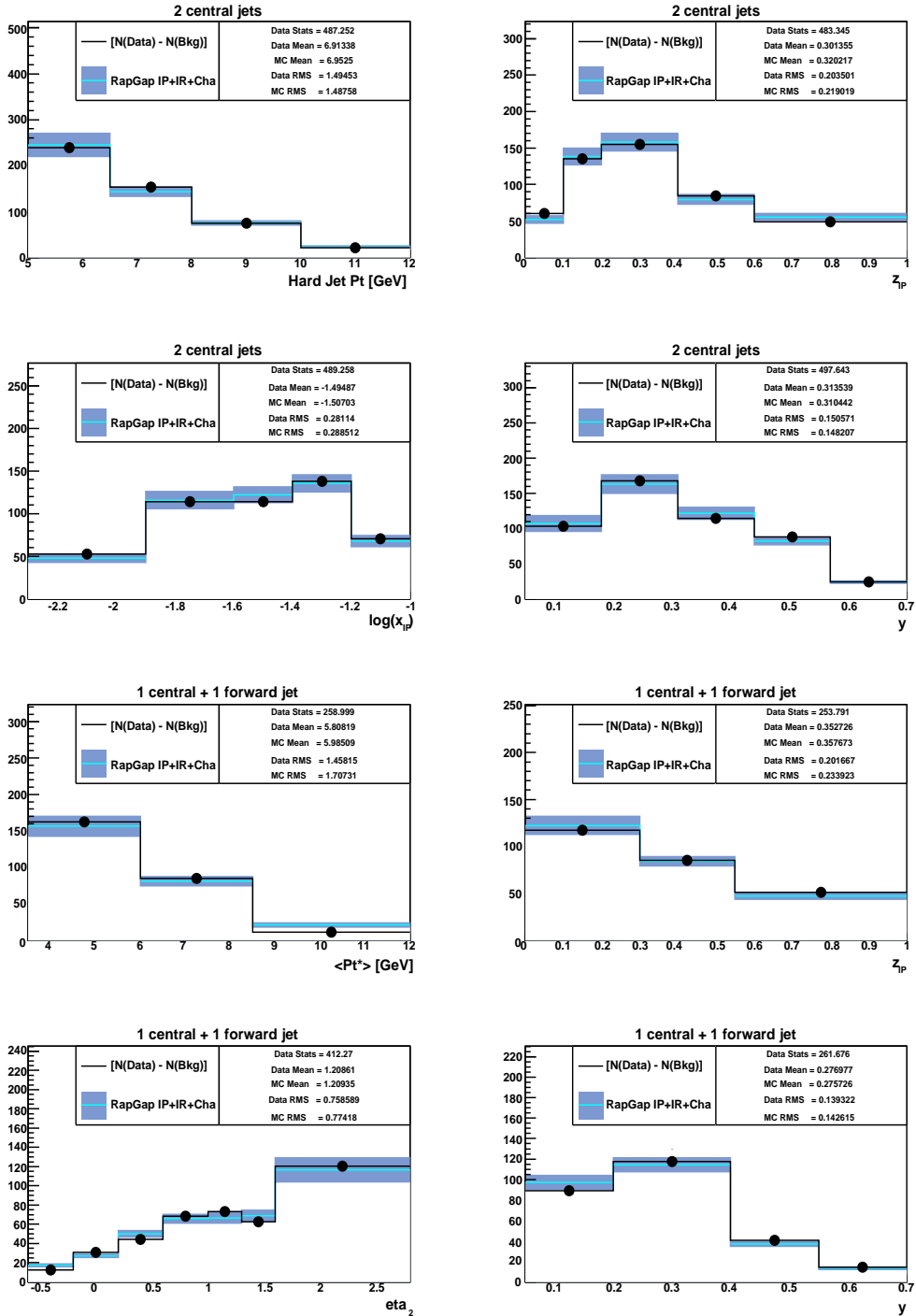| systematic shift	"2 central jets"	"1 central + 1 forward"
Luminosity	2.5%	2.5%
$\mathcal{E}_{\text{FPSeff}}$	2.0%	2.0%
s112	1.0%	1.0%
Total	3.4%	3.4%

Table 7.2: Correlated Systematic Shifts Summary Table

Figure 7.21: Jet variables for the "1 central + 1 forward jet" selection. The statistical errors are comparable with the size of the data points. The blue band corresponds to the combined model systematic uncertainties.

Chapter 8

Results

In this chapter, the measured cross section at the level of stable hadrons for both jet topologies will be presented. The measured data will be compared to the Monte Carlo predictions and to the NLO QCD calculations obtained with the program `nlojet++`. In the MC models and NLO QCD predictions the diffractive parton distribution functions "H1 2006 Fit B" and "H1 2007 Jets" are used.

The data points are presented with inner error bars corresponding to statistical uncertainties and outer error bars representing statistical and systematic errors added in quadrature. The NLO QCD theoretical predictions are shown with the combined error imposed by hadronisation uncertainties and scale variations. The $\sim 3.4\%$ normalisation uncertainty emerging from the estimation of correlated systematic errors (see Table 7.2) is not presented.

8.1 "2 central jets" Topology

In order to prove the consistency between LRG and FPS method of analysis of diffractive events, the measurement of the differential cross section in $\log(x_{I\!P})$ was performed in the phase space of the analysis [47]. The phase space of the analysis [47] is defined as:

$$4\ GeV^2 < Q^2 < 80\ GeV^2$$
$$0.1 < y < 0.7$$
$$x_{I\!P} < 0.03$$
$$p_{T,1}^* > 5.5\ GeV$$
$$p_{T,2}^* > 4\ GeV$$
$$-1 < \eta_{1,2} < 2.$$

If these cuts are implemented to our analysis, the only difference is in the selection of diffractive events and the method of reconstruction of the diffractive variables.
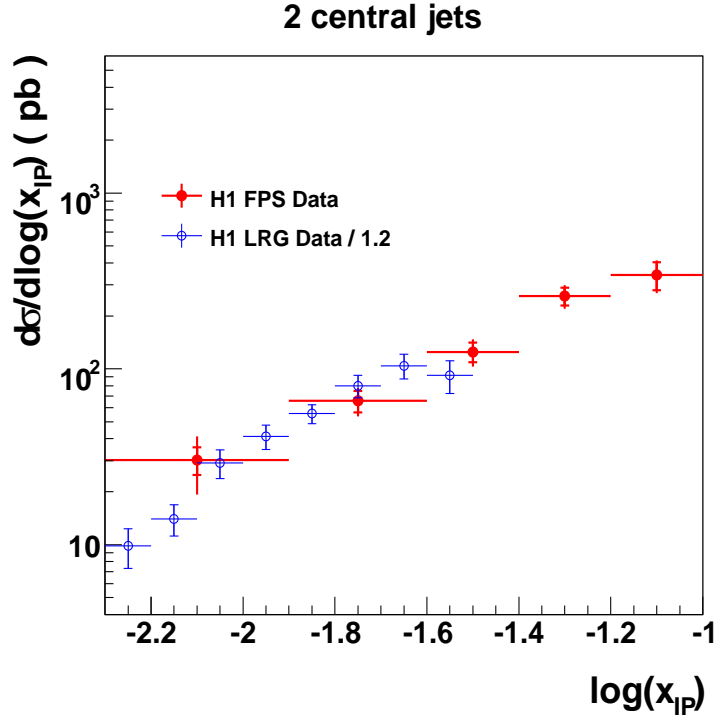
Figure 8.1: Differential cross section in $\log(x_{I\!P})$ in the phase space of [47]. The published data (blue) are scaled down by the factor 1.2 and are presented with total errors. Data measured in this analysis (red) are presented with the statistical (inner bar) and total (outer bar) errors.

The differential cross section in $\log(x_{I\!P})$ for the dijets in events tagged by FPS and results from [47] is presented in the Fig. 8.1. For the consistency check the LRG dijet data were scaled down by the factor 1.2 which is a measured normalisation difference between FPS and LRG reconstruction method [18] mainly due to the proton dissociation background in the LRG sample. The comparison is showing a very good consistency within the experimental errors. Note that the phase space of diffractive DIS dijet measurement in this analysis is extended by factor of 3 in comparison with [47].

The cross section for the topology "2 central jets" is measured over the full kinematic range specified as:

$$4 \ GeV^2 < Q^2 < 110 \ GeV^2 \tag{8.1}$$
$$0.05 < y < 0.7 \tag{8.2}$$
$$x_{I\!P} < 0.1 \tag{8.3}$$
$$p^*_{T,1} > 5 \ GeV \tag{8.4}$$
$$p^*_{T,2} > 4 \ GeV \tag{8.5}$$
$$-1 < \eta_{1,2} < 2.5. \tag{8.6}$$

The measured data are compared to NLO QCD predictions and three MC models: `RAPGAP` with resolved and direct pomeron model and `SCI` model. The NLO QCD predictions are calculated with `nlojet++` program and DPDFs "H1 2006 Fit B" and "H12007 Jets". Predictions based on the DPDF fits are scaled down by factor 1.2 due to the fact that the fits have been obtained with the LRG method with proton dissociation background.

The total experimental cross section for the "2 central dijets" topology as measured for the data is

$$\sigma_{2c} = 250.5 \pm 14.3 \ (stat) \pm 30.1 \ (syst) \ pb.$$

8.1.1 Comparison to NLO QCD calculations

In Figs. 8.2 and 8.3 the comparison of diffractive dijet cross sections measured single-differentially in $p^*_{T,1}$, $p^*_{T,2}$, Q^2, y, $|\Delta\eta *|$, $z_{I\!P}$ and $\log(x_{I\!P})$ with NLO QCD calculations are shown.

The NLO QCD calculations are corrected to the level of stable hadrons with the hadronisation corrections as described in Sec. 7.5. The average uncertainty of the hadronisation effects was estimated to be $\sim 7\%$. The scale uncertainties were obtained by varying the scale $\mu^2 = Q^2+ < p^*_T >^2$ by $4\mu^2$ and $\mu^2/4$, the average uncertainty is $\sim 40\%$. These uncertainties were combined in quadrature and will be further denoted as "combined". In the calculations, the errors are calculated for each bin separately. In the Figures, the inner error band of the NLO QCD predictions represents the scale uncertainties and the outer error band stands for the combined uncertainties for the DPDF "H1 2006 Fit B". The calculations obtained with DPDF fit "H1 2007 Jets" are presented as a line (uncertainties of the NLO QCD predictions are approximately the same as for the "H1 2006 Fit B").

In the lower part of each Figure, the ratios R of theory to data are presented. The total cross section as obtained with the NLO QCD predictions is

$$\sigma_{2c}^{H12006B} = 270.0 \pm 15.4 \ (hadro) \ ^{+98.9}_{-56.8} \ (scale) \ pb.$$
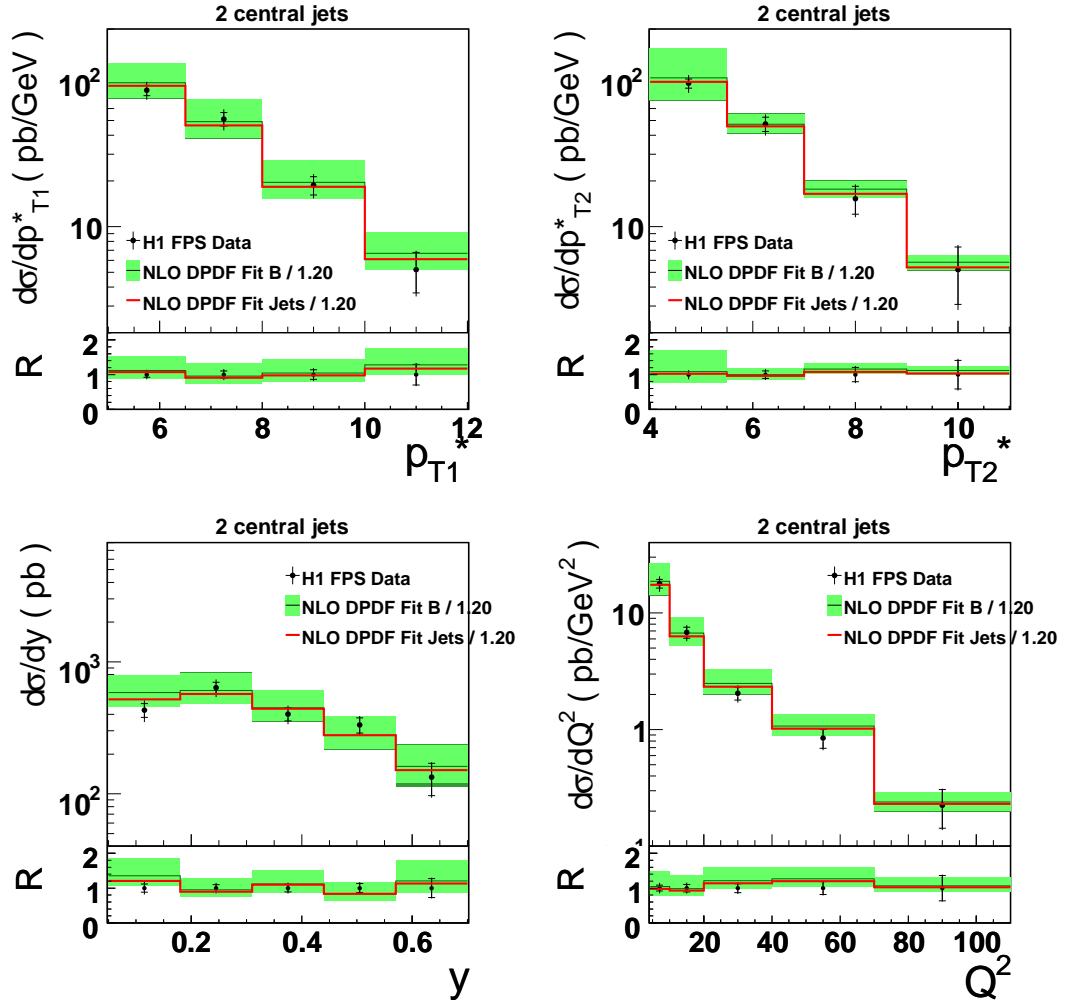$$\sigma_{2c}^{H12007J} = 254.3 \pm 11.6 \ (hadro) \ ^{+76.3}_{-45.7} \ (scale) \ pb.$$

Figure 8.2: Differential cross section as a function of $p^*_{T,1}$, $p^*_{T,2}$, y and Q^2 for the "2 central jet" topology. Data are presented with statistical error (inner bar) and total error (outer bar). The "H1 2006 Fit B" NLO QCD predictions corrected to the hadron level are presented with scale error (inner band) and total error (outer band), the calculations based on DPDF "H1 2007 Jets" with applied hadronisation corrections are presented as a line. Total normalisation error of 3.4% is not shown.
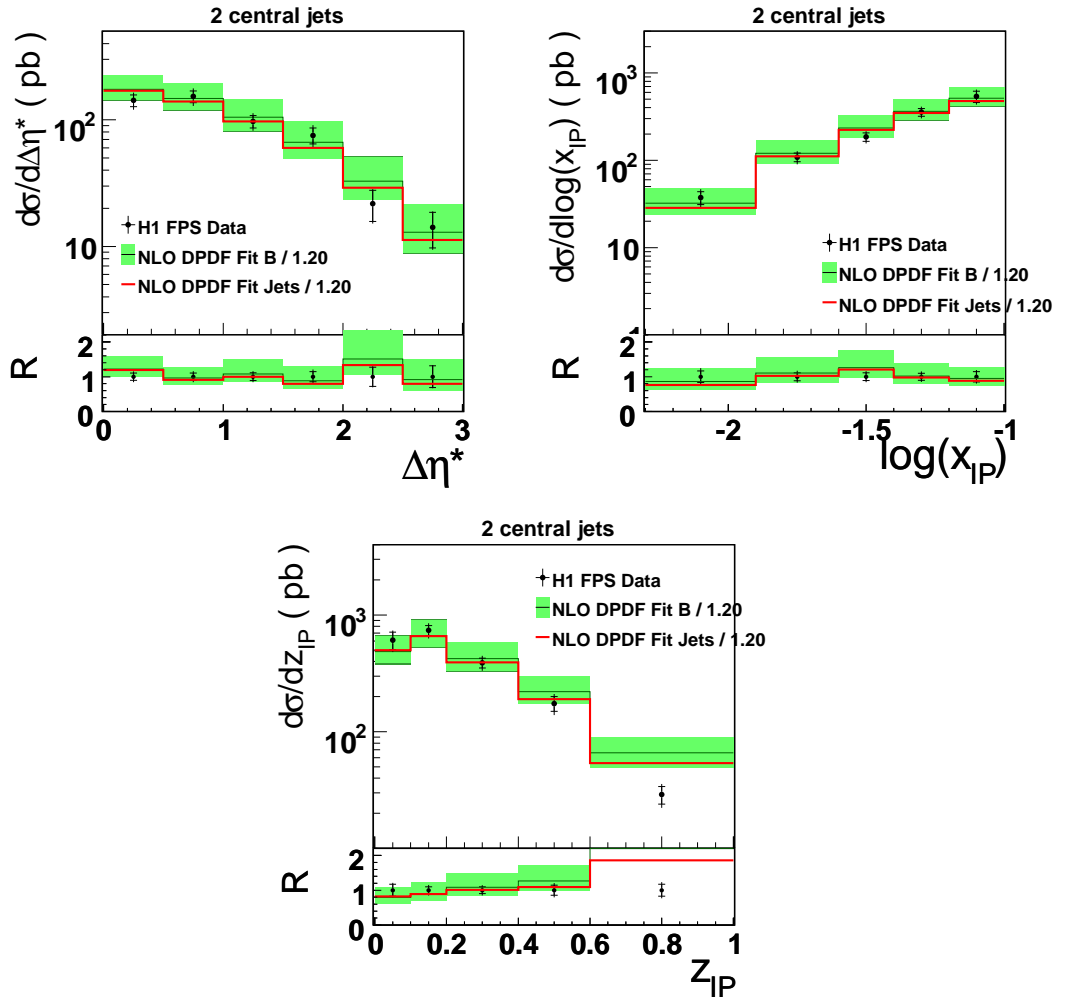
Figure 8.3: Differential cross section in $|\Delta\eta^*|$, $\log(x_{I\!P})$ and $z_{I\!P}$. For detailed description see Fig. 8.2.

Within the experimental errors, the data are satisfactorily described by NLO QCD calculations based on "H1 2006 Fit B" and "H1 2007 Jets". In accordance with expectations the fit "H1 2007 Jets" gives slightly lower prediction than "H1 2006 Fit B" and provides a slightly better description of the data.

The measured single-differential cross sections in Fig. 8.2 are described by NLO QCD within errors satisfactorily, the cross sections agree in the first bin of the y distribution better for the predictions of the "H1 2007 Jets" fit than for the DPDF "H1 2006 B". This is due to the fact that the "H1 2006 Fit B" does not constrain the gluon part of the DPDF fit above $\beta \sim 0.3$ well. The "H1 2007 Jets" fit includes the diffractive DIS dijet data which are sensitive to the gluon part of the DPDF and therefore constrains the gluon density for $0.1 < \beta < 1.0$.

In the Fig. 8.3 the NLO QCD predictions describe the data within errors satisfactorily with the exception of the last $z_{I\!P}$ bin. On should take into account, that the "H1 2006 Fit B" is constrained for values of $\beta < 0.8$ and the fit "H1 2007 Jets" is constrained for $0.05 < z_{I\!P} < 0.9$. Therefore the NLO QCD predictions for the highest $z_{I\!P}$ values are based on extrapolations and are not reliable.

8.1.2   Comparison to MC Models

For comparison to the data three different models have been used: `RAPGAP` resolved pomeron model with DPDF "H1 2006 Fit B", `RAPGAP` direct pomeron model and `LEPTO` with the Soft Colour Interaction model. The `SCI` MC parameters have been tuned to describe the total cross section.

Fig. 8.4 shows comparison of the single-differential cross sections of the jet transverse momentum of both jets $p_{T,1}^*$ and $p_{T,2}^*$, y and Q^2 with the MC models. None of the models succeeds in describing both the shape as well as the normalisation of the data. From the ratio plots can be deduced that the `RAPGAP` resolved pomeron model gives best shape description, but is off in total normalisation. The `SCI` model gives softer shapes for the transverse momenta as well as for the Q^2 cross section. The `RAPGAP` direct MC predicts softer shapes in the transverse momenta and Q^2 distributions in comparison to the resolved model. The shapes of the y distribution for `RAPGAP` direct and resolved pomeron model are similar except for the lowest bin and are off in normalisation in comparison to the data. The `SCI` model fails to describe the shape.

The Fig. 8.5 shows the differential cross sections in $|\Delta\eta^*|$, $\log(x_{I\!P})$, $z_{I\!P}$ and t for data and MC models. The observable $|\Delta\eta^*|$ is best described by the `SCI` model, both resolved and pomeron models are off in normalisation. The discrepancy in comparison to the data in $\log(x_{I\!P})$ is biggest for the direct pomeron model, the model prediction peaks at $\log(x_{I\!P}) \sim -1.5$. The `SCI` model is characterised by softer slope in comparison with the data. The best shape description is achieved by the resolved pomeron model, nevertheless it is off in normalisation. Since
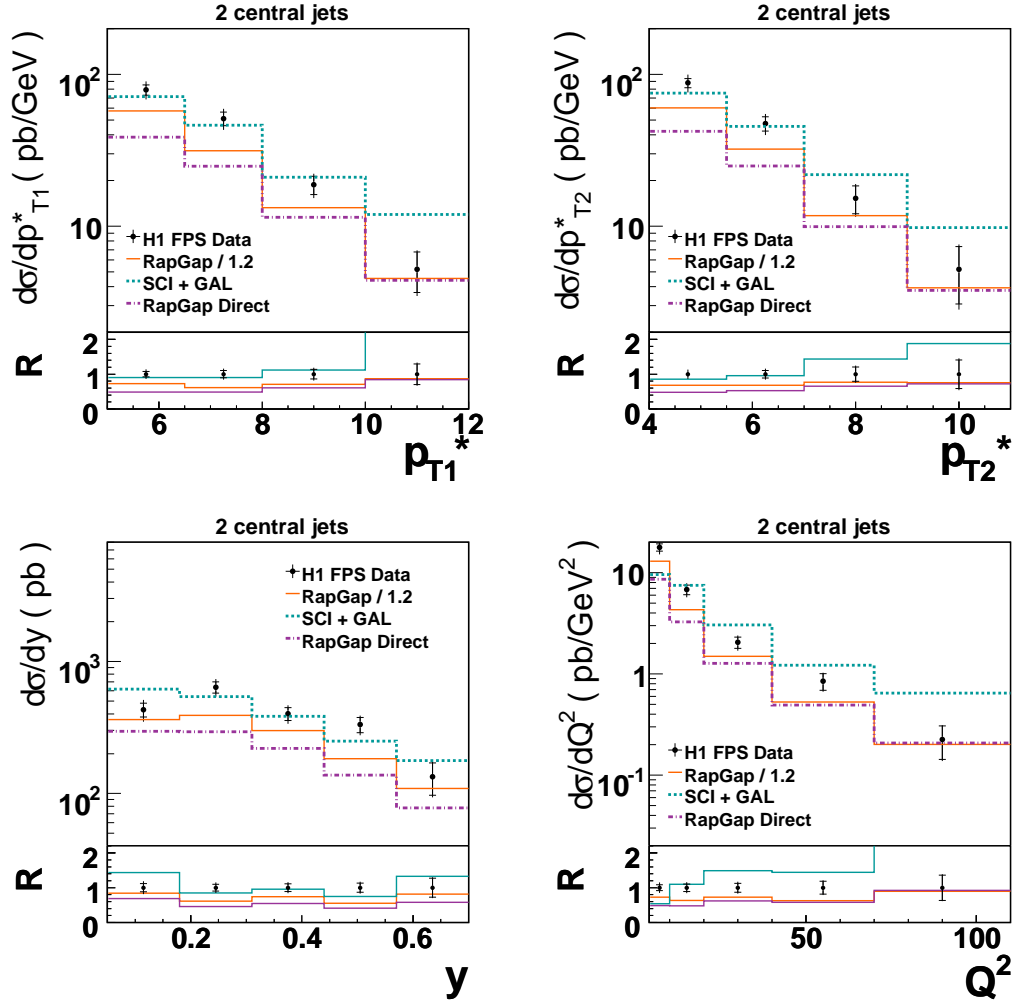
Figure 8.4: Differential cross section in transverse momentum of the hardest and second hardest jet, y and Q^2. Data are presented with statistical error (inner bar) and combined error (outer bar). The MC resolved and direct pomeron and SCI models are presented as a line. Total normalisation error of 3.4% is not presented.
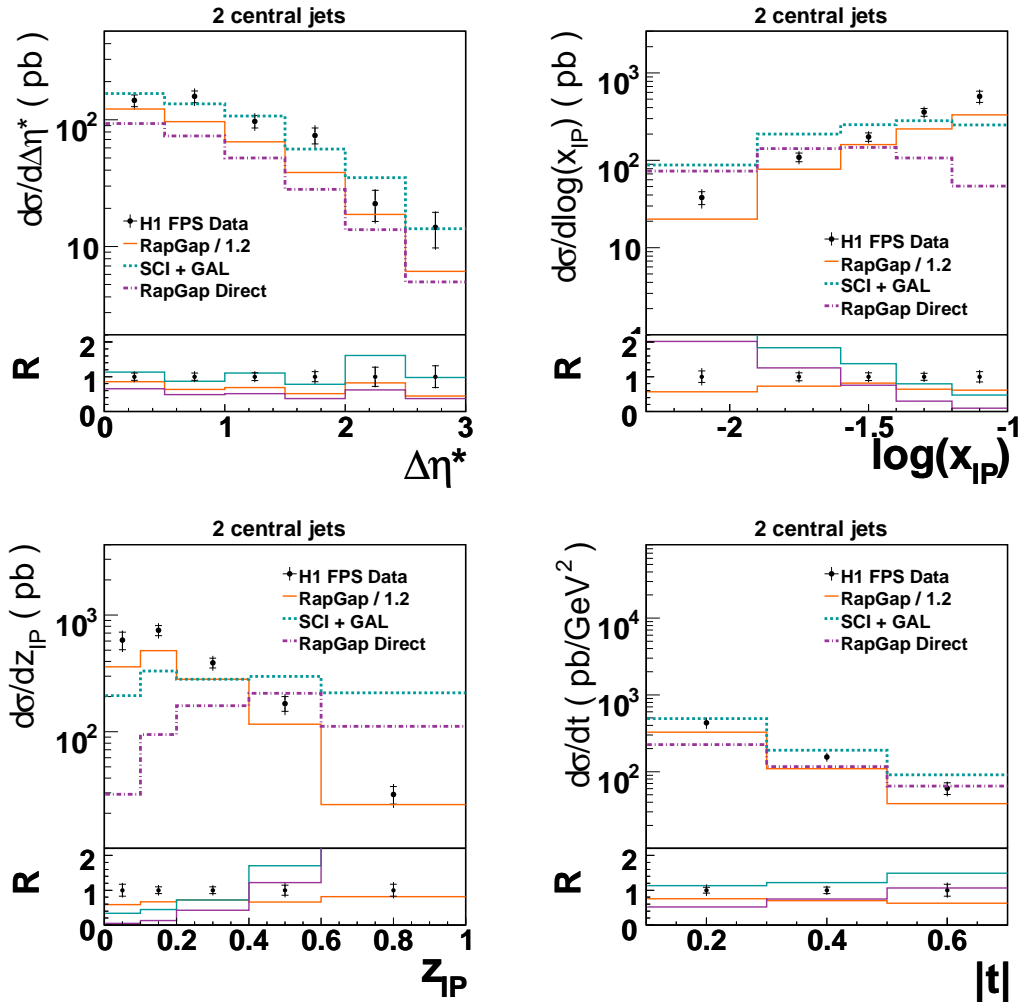
Figure 8.5: Differential cross section in $|\Delta\eta^*|$, $\log(x_{I\!P})$, $z_{I\!P}$ and t. For more detailed description see Fig. 8.4.
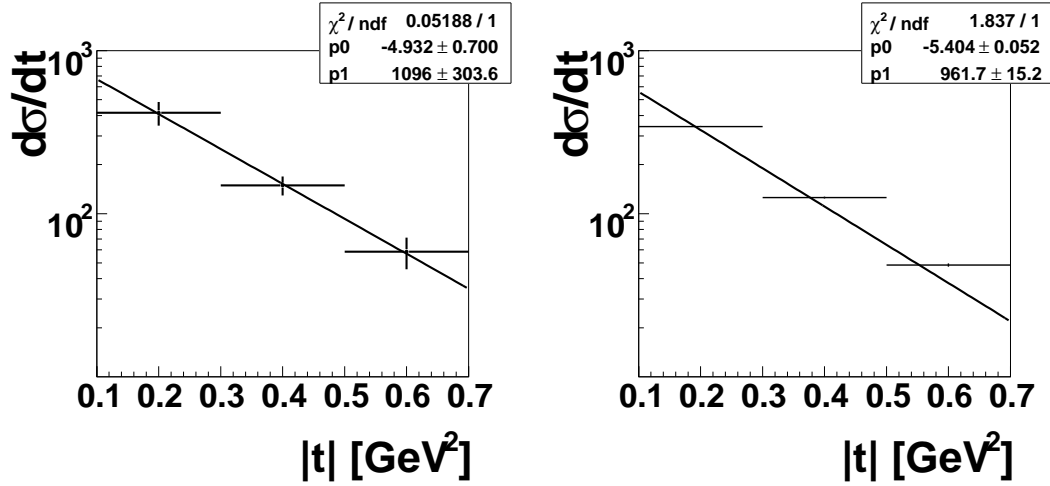
Figure 8.6: Exponential fit to the differential cross section measured in t: data (left), resolved pomeron MC model (right).

the $x_{I\!\!P}$ and $z_{I\!\!P}$ are correlated by definition, the big disagreement of the `SCI` and direct pomeron models is present also in the comparison to the data in the differential cross section measured in $z_{I\!\!P}$. The best shape description is obtained with resolved pomeron model.

The shape of the t-distribution is best described by the resolved pomeron model MC, the `SCI` and direct pomeron models predict softer slopes in comparison with the data. According to the pomeron flux Ansatz the data and the resolved pomeron model MC were fitted by means of using an exponential fit $\exp(Bt)$. For the fitting purposes the bin centre corrections have been applied to the differential cross section in t. The fit gives $\chi^2/ndf = 0.05$ for data and $\chi^2/ndf = 1.84$ for the resolved pomeron MC. The results for the fit of the slope parameter are:

$$B_{Data} = -4.93 \pm 0.7 \qquad (8.7)$$
$$B_{\texttt{RAPGAP}} = -5.40 \pm 0.05 \qquad (8.8)$$

The fits are presented in Fig. 8.6, the fitted parameters for data and MC are in agreement within experimental error.

We can conclude that the Monte Carlo models are in general not able to describe the measured differential cross sections successfully, the best description is provided by `RAPGAP` resolved pomeron model. This model describes the data

in shape but is off in normalisation. The direct pomeron and `SCI` MC models fail to describe mainly the differential cross sections directly related to the diffractive kinematical variables.

8.2 "1 central + 1 forward jet" Topology

The main goal of the cross section measurement of the "1 central + 1 forward jet" topology was the search for physics beyond DGLAP. The selection of diffractive events by means of tagging the outgoing elastic proton gives an unique opportunity to explore the pseudorapidity range of the forward jet to the highest η which are allowed by the experimental setup of the H1 detector.

The cross section for the topology "1 central + 1 forward jet" is measured over the full kinematic range specified as:

$$4 \ GeV^2 < Q^2 < 110 \ GeV^2 \tag{8.9}$$

$$0.05 < y < 0.7 \tag{8.10}$$

$$x_{I\!P} < 0.1 \tag{8.11}$$

$$p^*_{T,1,2} > 3.5 \ GeV \tag{8.12}$$

$$M_{12} > 12 \ GeV \tag{8.13}$$

$$-1 < \eta_1 < 2.5 \tag{8.14}$$

$$1 < \eta_2 < 2.8 \tag{8.15}$$

$$\eta_2 > \eta_1, \tag{8.16}$$

for the differential cross section measured in η_2 the cut on the pseudorapidity of the forward jet has been extended to $-0.6 < \eta_2 < 2.8$. The total experimental cross section for the "1 central + 1 forward jet" topology is

$$\sigma_{1c1f} = 153.4 \pm 11.8 \ (stat) \pm 23.0 \ (syst) \ pb.$$

The measured differential cross sections are compared to the NLO QCD predictions with both DPDFs "H1 2006 fit B" and "H1 2007 Jets" and the three MC models as in Sec. 8.1

8.2.1 Comparison to NLO QCD predictions

The total cross section obtained with the NLO QCD calculations for two DPDF sets is:

$$\sigma_{2c}^{H12006B} = 150.3 \pm 10.4 \ (hadro) \ ^{+72.0}_{-39.2} \ (scale) \ pb.$$
$$\sigma_{2c}^{H12007J} = 133.2 \pm 10.4 \ (hadro) \ ^{+59.1}_{-33.1} \ (scale) \ pb.$$
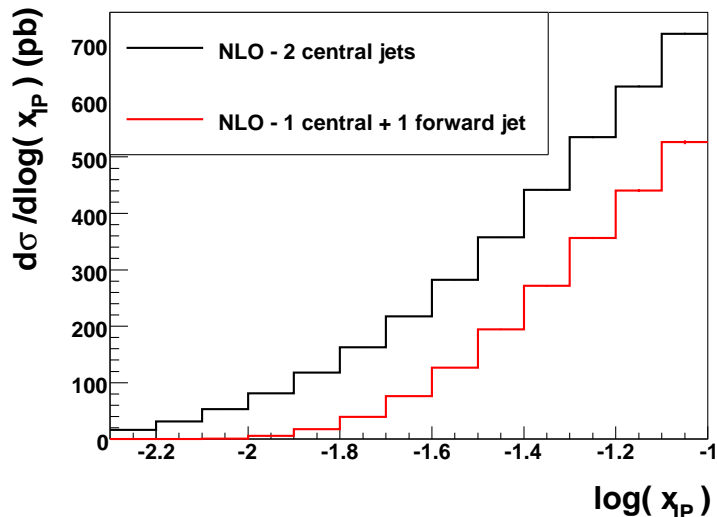
Figure 8.7: Differential cross section in $\log(x_{I\!\!P})$ for the "2 central jets" and "1 central + 1 forward jet" topologies for the DPDF "H1 2006 Fit B" calculated by NLO QCD.

Within the experimental errors, the data are satisfactorily described by NLO QCD calculations based on "H1 2006 Fit B" and "H1 2007 Jets". In accordance with expectations the fit "H1 2007 Jets" gives slightly lower prediction than "H1 2006 Fit B", the "H1 2006 Fit B" provides a slightly better description of the data.

Fig. 8.8 shows the differential cross sections for the mean transverse momenta of the forward and central jet $< p_T^* >$, $|\Delta\eta^*|$, η_2 and y. The measured data are within the errors described by the NLO QCD predictions. In contrary to the "2 central jets" topology, the lowest bin in the y distribution is in a good agreement with the data. The "1 central + 1 forward jet" topology is kinematical correlated to region of phase space with higher $x_{I\!\!P}$ values in comparison with the "2 central jet" topology. Since $x_{I\!\!P} \sim 1/\beta$, the high $x_{I\!\!P}$ values correspond to low values of β, i.e. the amount of events with high β values where the DPDFs are not reliable is significantly smaller. Fig. 8.7 demonstrates the difference of phase space in $x_{I\!\!P}$ for the two jet topologies as obtained by the NLO QCD calculations.

In Fig. 8.9 the differential cross sections measured in $z_{I\!\!P}$, $\log(\beta)$ and $|\Delta\phi^*|$ are presented. The meaning of $log(\beta)$ in diffractive events is the same as $\log(x)$ (where x is the Bjorken scaling variable) in the non-diffractive events and illustrates the length of the gluon ladder which is spanned between the hard process
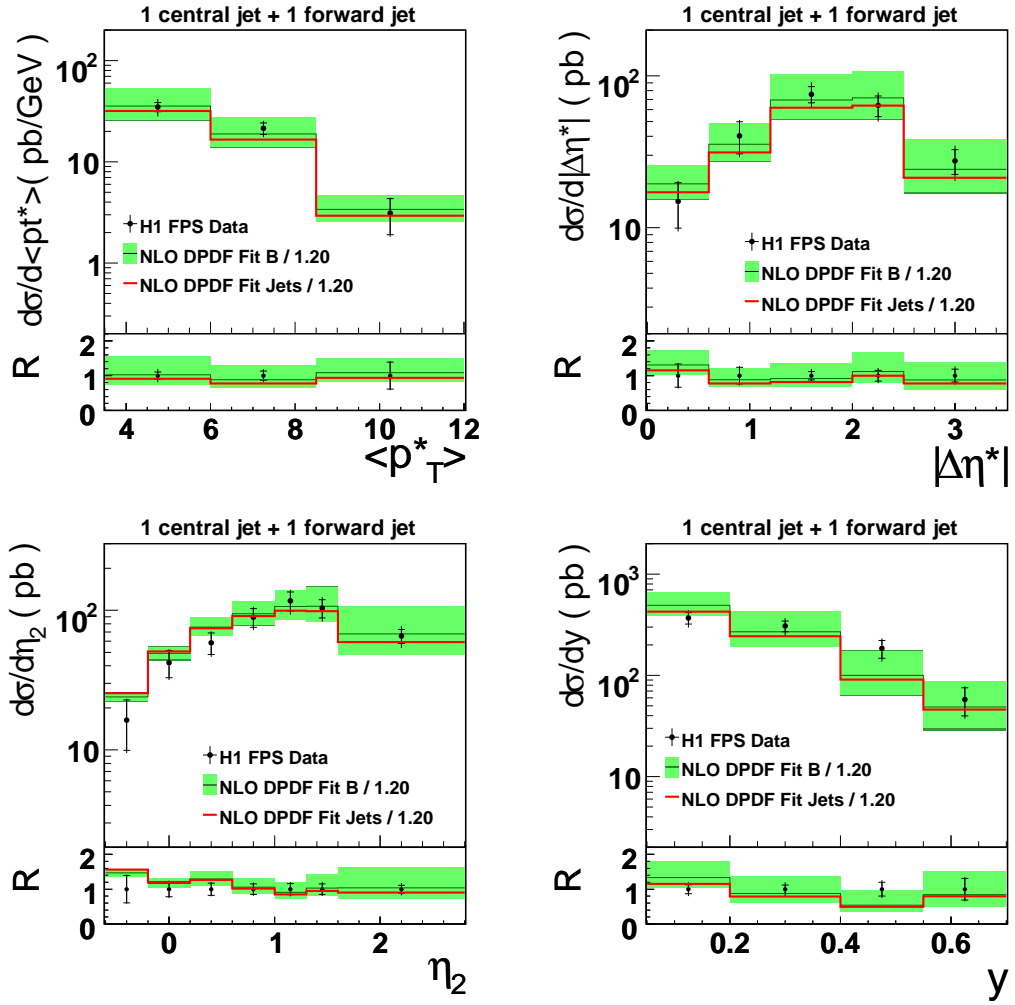
Figure 8.8: Differential cross section in $< p_T^* >$, $|\Delta\eta^*|$, η_2 and y. Data are presented with statistical error (inner bar) and total error (outer bar). The "H1 2006 Fit B" NLO QCD predictions corrected to the level of stable hadrons are presented with scale error (inner band) and combined error (outer band), the calculation based on DPDF "H1 2007 Jets" with applied hadronisation corrections is presented as a line. Total normalisation error of 3.4% is not presented.
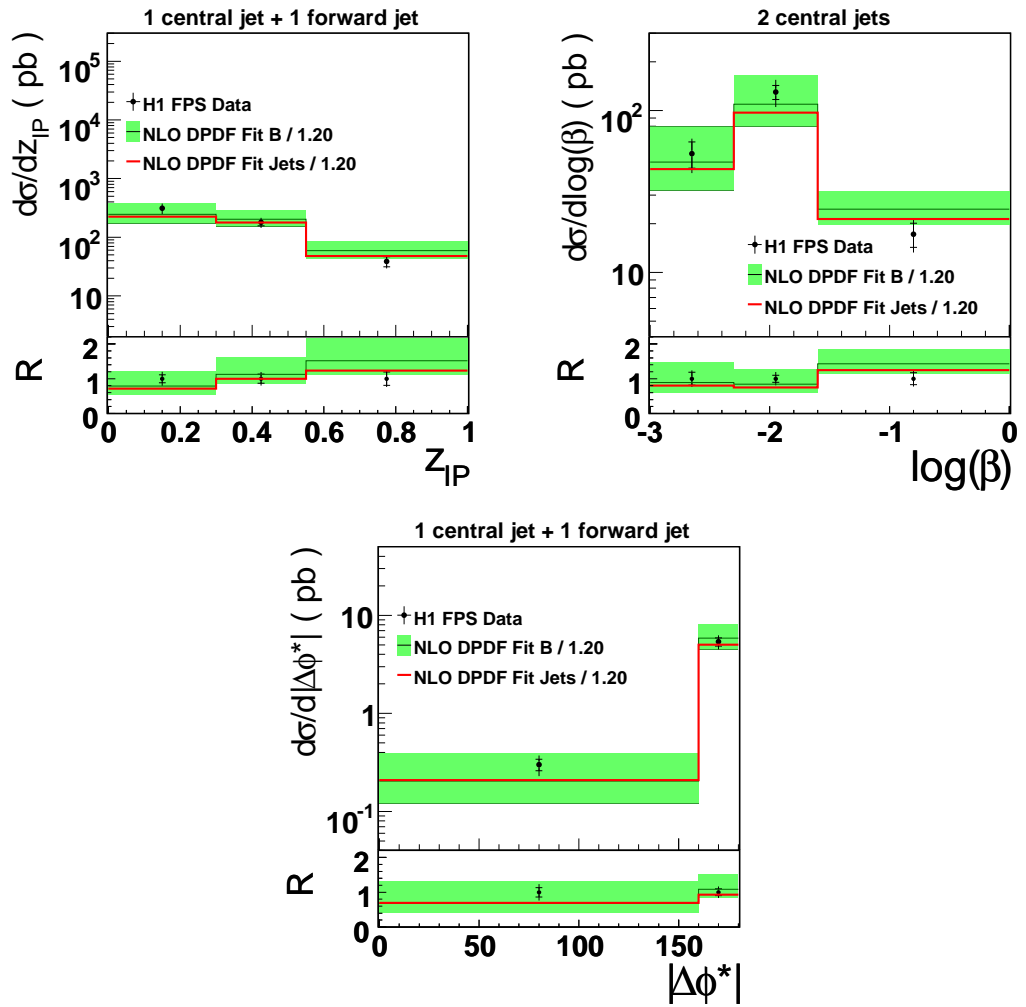
Figure 8.9: Differential cross section in $z_{I\!P}$, $\log(\beta)$ and $|\Delta\phi^*|$. For further description see Fig. 8.8.

and the pomeron in diffractive case and proton in non-diffractive interactions. For the topology of two jets with a large rapidity gap between them, additional gluons can be emitted in the gap in the BFKL picture. These gluon emissions lead to decorrelation of the two jets in the azimuthal angle $|\Delta\phi^*|$ which would result in significantly higher cross section in the range of $|\Delta\phi^*| \ll 180°$ in comparison with the DGLAP predictions. The observed agreement between the measured cross section and the NLO DGLAP QCD mechanisms leads to the conclusion that no BFKL QCD predictions are necessary in order to describe the data.

We can conclude that the differential cross sections in all presented variables are well described by the NLO QCD predictions based on DGLAP evolution equations.

8.2.2 Comparison to MC Models

For comparison to data three different models have been used: `RAPGAP` resolved pomeron model with DPDF "H1 2006 Fit B", `RAPGAP` direct pomeron model and `LEPTO` with the Soft Colour Interaction model [1].

The Fig. 8.10 presents the differential cross sections in mean transverse momentum $< p_T^* >$ of the two jets, $|\Delta\eta^*|$, η_2 and y. The resolved pomeron MC model is able to describe the shape of the differential cross section in $< p_T^* >$ best, the direct pomeron and `SCI` model give a slightly softer slope of the distribution. The direct and resolved pomeron models are off in normalisation. The $|\Delta\eta^*|$ distribution is best described by the `SCI` model. The direct and resolved pomeron models are off in normalisation, but agree in shape. All three models predict a slightly higher cross section for the events with the jets with smallest $|\Delta\eta^*|$.

The resolved pomeron MC describes the data only for the low η_2 values. Moving into the forward region the resolved pomeron MC predictions rise less than the measured cross section. The direct pomeron model is off in normalisation, but agrees in shape within the errors. The shape of the y distribution is best described by the resolved pomeron model, the `SCI` model does not agree in shape. The shape and normalisation of the direct pomeron model is in a worse agreement than the resolved pomeron model. For the single differential cross section in y, neither the shape nor the normalisation description of the data by any of the MC models is satisfactory.

In the Fig. 8.11 the differential cross sections in $z_{I\!\!P}$, $\log(\beta)$ and $|\Delta\phi^*|$ are shown. The shapes of the $z_{I\!\!P}$ and $\log(\beta)$ distributions are described only by the resolved pomeron model, while the direct pomeron and the `SCI` models fail. The direct pomeron model is off in normalisation. The shape of the decorrelation

---

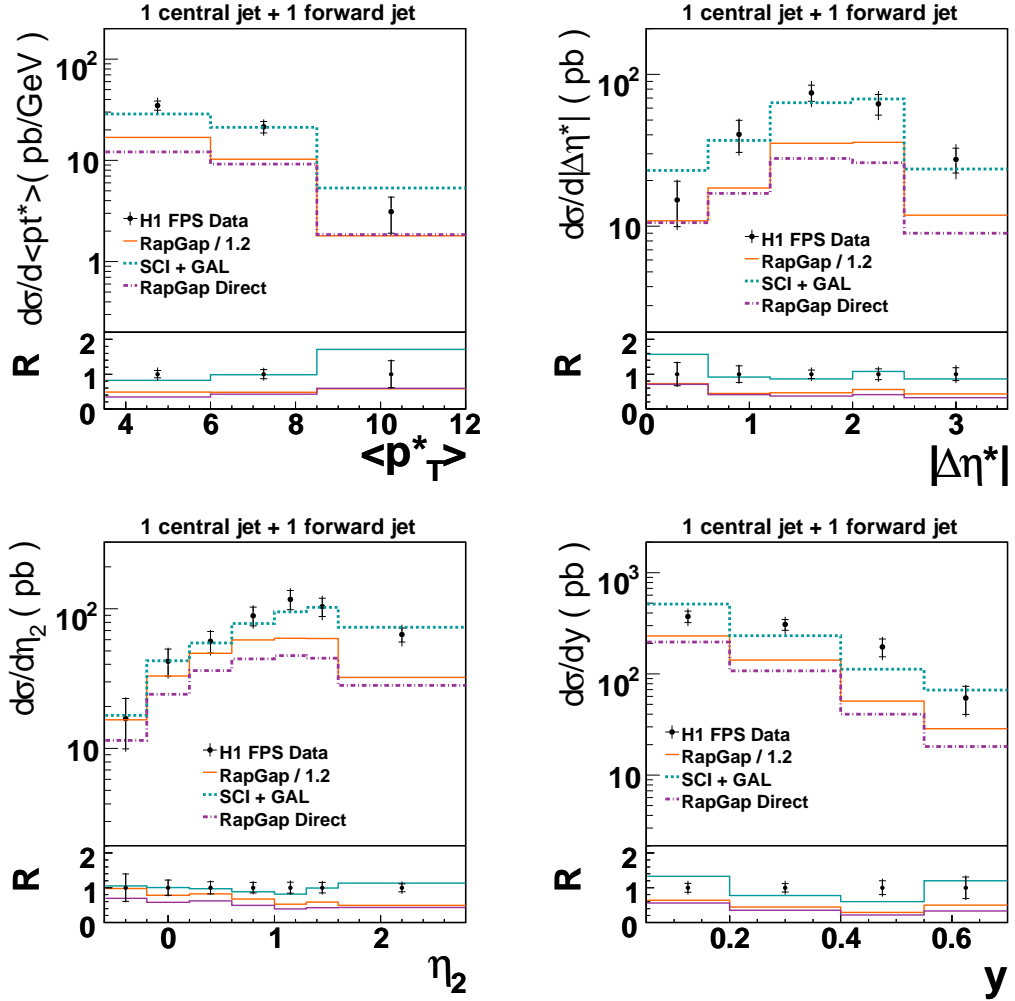[1] the same parameters were used as for the "2 central jets" topology

Figure 8.10: Differential cross section in mean transverse momentum, $|\Delta\eta^*|$, η_2 and y. Data are presented with statistical error (inner bar) and total error (outer bar). The MC resolved and direct pomeron and SCI models are presented as a line. Total normalisation error of 3.4% is not presented.
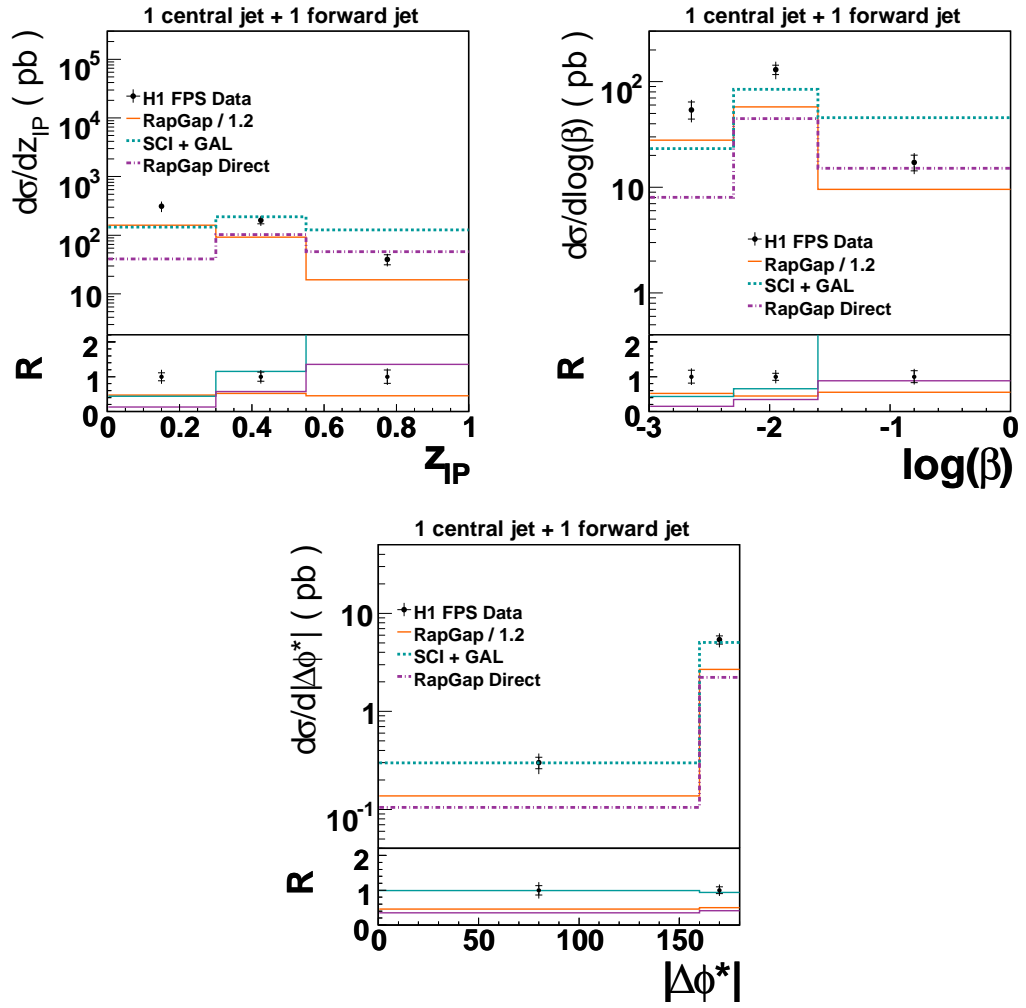
Figure 8.11: Differential cross section in $z_{I\!P}$, $\log(\beta)$ and $|\Delta\phi^*|$. For further description see Fig. 8.10.

$|\Delta\phi^*|$ of the two jets is described well by all three models.

We conclude that the resolved pomeron model in general describes the shapes of the single-differential cross sections satisfactorily, but is off in normalisation. Moving to the backward region, i.e. lower values of η_2, the normalisation discrepancy vanishes.

The direct pomeron model is off in normalisation in comparison to the data and the normalisation discrepancy is bigger than in the resolved pomeron model. The shapes of the diffractive variables are not properly described.

The `SCI` model agrees with the data in normalisation, even though its parameters have been tuned for the "2 central jets" topology. The `SCI` model describes the jet angular distribution (azimuthal as well as polar) very well within the experimental errors, but fails to describe other variables completely.

Chapter 9

Summary

The jet production in diffractive DIS has been investigated in this analysis. The statistics of HERA-II data taking period allows to measure the jets with the method of selecting diffractive events with the tagging of outgoing elastic protons for the first time. This unique measurement extends the available phase space and enables studies of parton evolution beyond the DGLAP formalism.

The measurement of single-differential cross sections at the level of stable hadrons of the "2 central jets" topology extends the phase space in the $x_{I\!P}$ kinematical variable with respect to previous measurement [47] using the LRG method for selecting diffractive events by factor 3. The consistency with this measurement in the phase space of [47] was proved.

The NLO QCD calculations obtained with `nlojet++` program adjusted for diffraction have been performed with two different diffractive fits "H1 2006 Fit B" and "H1 2007 Jets". The prediction of the fit "H1 2007 Jets" which was based also on the jet data analysis gives a slightly better description of the measured cross sections in comparison to the "H1 2006 Fit B".

The measured data have been compared to the resolved and direct pomeron as well as the soft colour interaction MC models. The resolved pomeron model as implemented in the `RAPGAP` MC gives the best shape description, but is constantly off in normalisation. The direct pomeron model as implemented in the `RAPGAP` MC gives the biggest normalisation discrepancy and fails to describe the diffractive variables completely. The parameters of the `SCI` model as implemented in `LEPTO` were tuned to describe the total cross section of the "2 central dijets" topology. The description of the measured differential cross section in $|\Delta\eta^*|$ of the two jets by the `SCI` model is acceptable, however the `SCI` model fails to describe other variables.

The measurement of the dependence of the cross section on the momentum transfer t was measured for the first time for the diffractive dijets in DIS. The value of the slope of this distribution $B_{Data} = -4.93 \pm 0.70$ agrees well within

experimental errors with the prediction of the resolved pomeron model ($B_{\texttt{RAPGAP}} = -5.40 \pm 0.05$).

The measurement of the cross section of the "1 central + 1 forward jet" topology enables the studies of the parton evolution beyond the DGLAP formalism. Taking into account the acceptance of the H1 and FPS detectors the phase space has been optimised for search for non-DGLAP parton evolution by selecting one hard jet going into the direction of the outgoing scattered proton and a second jet produced in the central region. The cross sections have been measured and corrected to the level of stable hadrons and compared to the NLO QCD DGLAP calculations. The QCD predictions describe the measured data very well within the experimental errors. The observed agreement between the measured cross section and the NLO DGLAP QCD predictions leads to the conclusion that no BFKL QCD mechanism are necessary in order to describe the cross sections measured in the "1 central + 1 forward jet" topology.

The resolved pomeron model in general describes the shapes of the single-differential cross sections satisfactorily, but is off in normalisation. In the backward region, i.e. lower values of η_2, the normalisation difference continuously improves. The direct pomeron model is even more off in normalisation than the resolved pomeron model and also shapes of the diffractive variables are not satisfactorily described. The $\texttt{SCI}$ model agrees with the data in normalisation, even though its parameters have been tuned for the "2 central jets" topology. The $\texttt{SCI}$ model describes the jet angular distribution (azimuthal as well as polar) well within the experimental errors, but fails to describe other variables completely.

Appendix A

DIS 2010 and ICHEP 2010 H1Preliminary results

Diffractive Jets at H1

H1 Collaboration

An inclusive jet production in diffractive deep-inelastic scattering is presented. The diffractive selection is based on tagging the leading proton in the Forward Proton Spectrometer. The statistics of HERA II period with integrated luminosity of 156.7 pb^{-1} enables the measurement of jet final states for the first time in

the HERA history. The data cover the range $x_{I\!\!P} < 0.1$ in fractional proton longitudinal momentum loss, $|t| \leq 1.0$ GeV^2 in squared four-momentum transfer at the proton vertex and $4 \leq Q^2 \leq 110$ GeV^2 in photon virtuality. The phase space that is possible to reach with the FPS measurement extends the phase space of the large rapidity gap measurements[1]. The jets have been reconstructed in the hadronic centre-of-mass (HCM) system with the FastJet[2] algorithm.

Two jet topologies in the reaction $ep \to eXp$ are presented in this analysis. The central dijet topology presents a consistent comparison with the large rapidity gap analyse and shows the phase space extension. It provides a possibility to compare the predictions in kinematical region where the diffractive parton density functions haven't been verified before. The topology of one central and one forward jet is motivated by the search for parton dynamics beyond DGLAP evolution equations. Requirement for first hard jet reconstructed in the central region and second hard jet going in the direction of the outgoing proton enhance the possibility of breaking the strong p_T ordering which is required in the DGLAP evolution equations.

The "2 central jets" selection is defined with asymmetric cuts on transverse energy of the jets in the hadronic centre-of-mass system $p^*_{T,1} > 5\ GeV$ and $p^*_{T,2} > 4\ GeV$ and symmetric cuts on pseudorapidity in the H1 laboratory frame $-1 < \eta < 2.5$ with respect to the acceptance of the H1 detector. The non-DGLAP enhancing p^*_T cuts in the "1 central + 1 forward jet" selection require transverse energy of the central jet to be higher than $3.5\ GeV$ and the transverse energy of the forward jet higher than $4.5\ GeV$. The cuts on pseudorapidity η for the central jet is in the range $-1. < \eta_1 < 2.5$, η for the forward jet is in the range $1. < \eta_2 < 2.8$. In order to compare the measured cross sections with the NLO predictions an additional condition for ordering of the jets in η is required, i.e. $\eta_2 > \eta_1$.

The presented cross sections are corrected to the level of stable hadrons and compared to the Monte Carlo generator level predictions and NLO predictions with applied hadronisation corrections. The DGLAP NLO predictions obtained with `nlojet++` program with diffractive parton distribution functions with fit "H1 2006 B" describe the data well within errors, the `RAPGAP` Monte Carlo predictions show discrepancy in the overall normalisation which is significantly larger for the "1 central + 1 forward jet" selection (50%). The consistency with measurement obtained with the independent large rapidity gap selection method is proved within the errors.

---

[1]JHEP 0710:042
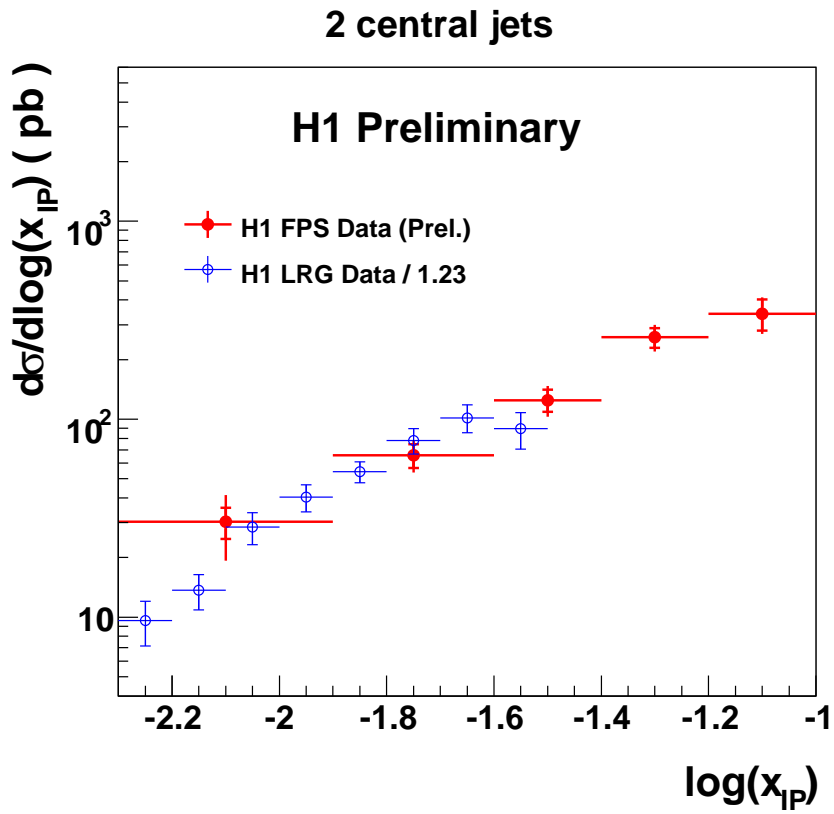[2]Phys. Lett. B641 (2006) [hep-ph/0512210]

Figure A.1: Differential cross section in $log(x_{I\!P})$. The LRG data are scaled down by the factor of 1.23 due to the missing proton dissociation background in the proton tagged data. The good consistency between two independent experimental techniques is shown and also the phase space extension in $x_{I\!P}$ by a factor of 3 is presented.
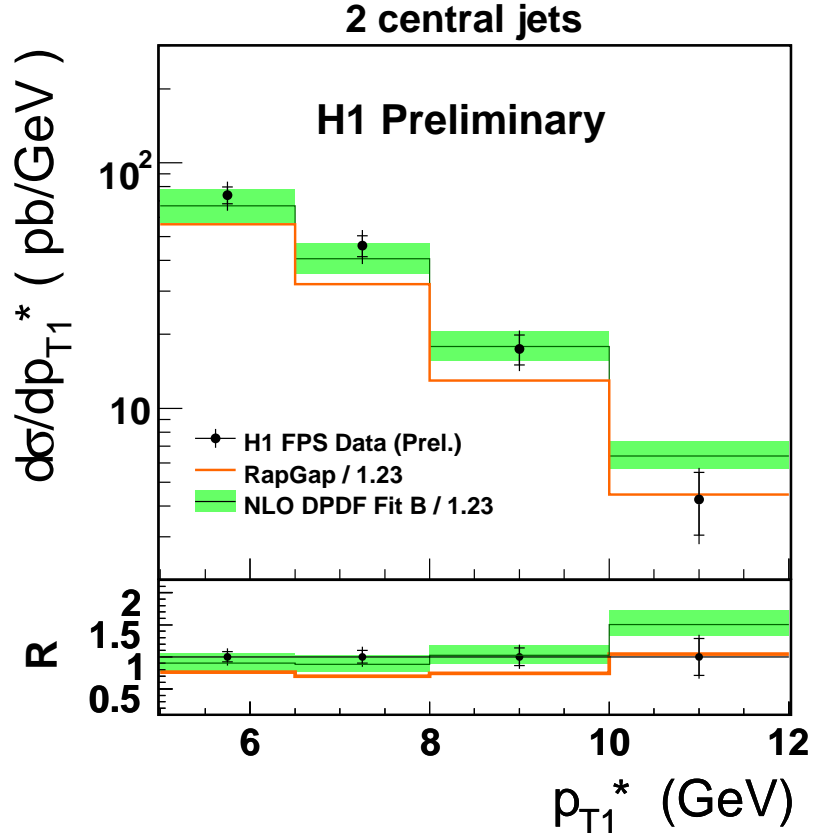
Figure A.2: Figure shows the differential cross section in transverse energy of the hardest jet in hadronic centre-of-mass system. The data are presented with the statistical error in the inner error bar and with the combined statistical and uncorrelated systematical error in the outer bar. The normalisation uncertainty is approximately 5% and it is not displayed. The comparison to Monte Carlo RAPGAP generator generator level cross section is presented as a red line. The NLO H1 2006 DPDF Fit B prediction corrected to the level of stable hadrons is presented in the green bar, the combined scale uncertainty and hadronisation uncertainty is shown. The NLO prediction is in a good agreement with the data within the total error.
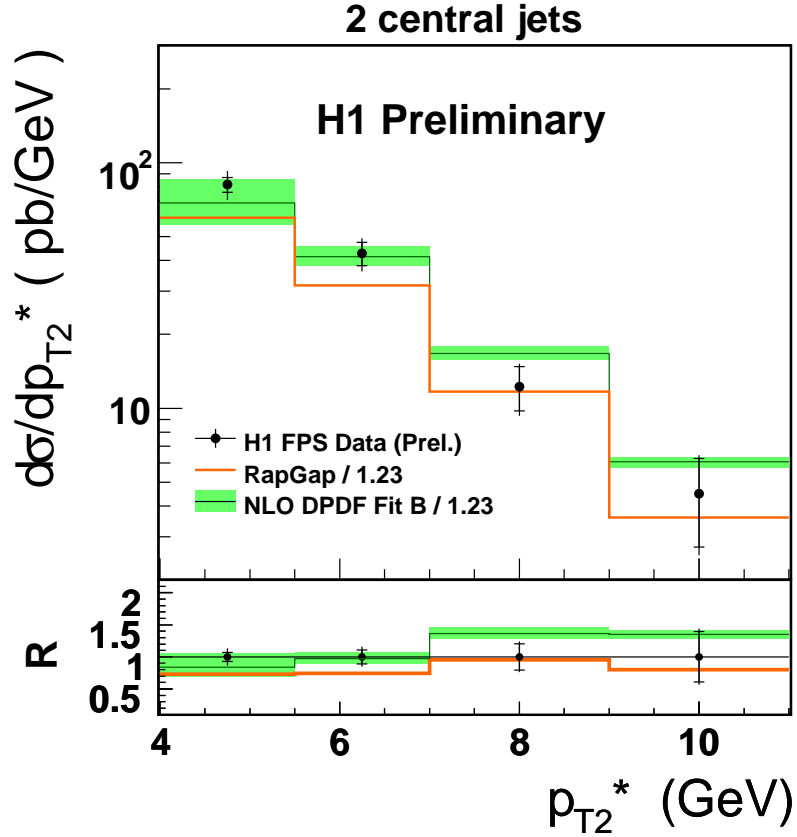
Figure A.3: Figure shows the differential cross section in transverse energy of the second hardest jet in hadronic centre-of-mass system. The data are presented with the statistical error in the inner error bar and with the combined statistical and uncorrelated systematical error in the outer bar. The normalisation uncertainty is approximately 5% and it is not displayed. The comparison to Monte Carlo RAPGAP generator generator level cross section is presented as a red line. The NLO H1 2006 DPDF Fit B prediction corrected to the level of stable hadrons is presented in the green bar, the combined scale uncertainty and hadronisation uncertainty is shown. The NLO prediction agrees with the data within the total error.
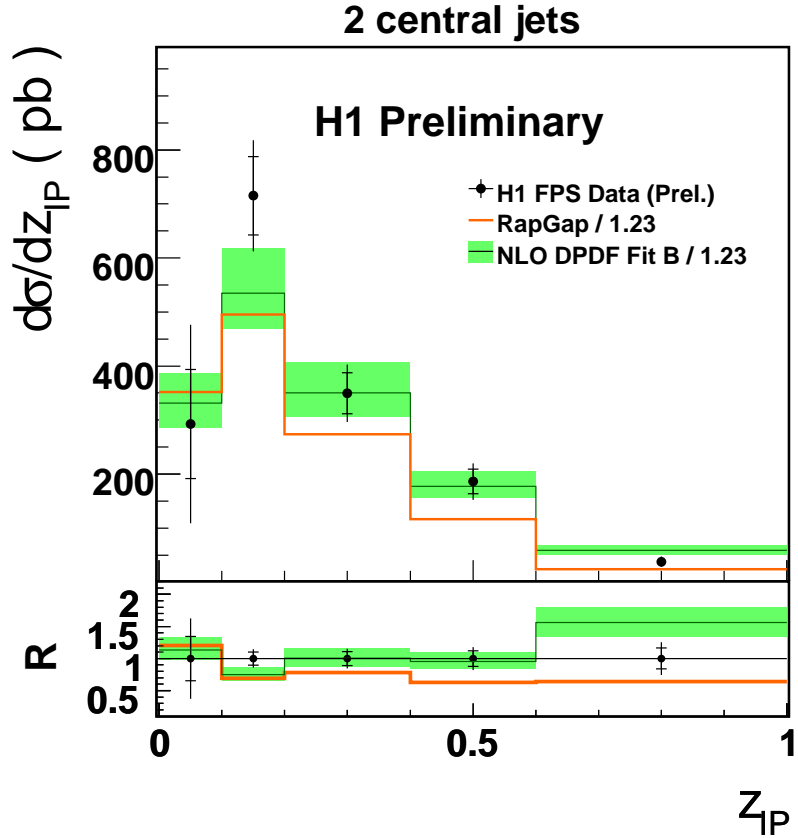
Figure A.4: Figure shows the differential cross section in $z_{I\!P}$. The data are presented with the statistical error in the inner error bar and with the combined statistical and uncorrelated systematical error in the outer bar. The normalisation uncertainty is approximately 5% and it is not displayed. The comparison to Monte Carlo `RAPGAP` generator generator level cross section is presented as a red line. The NLO H1 2006 DPDF Fit B prediction corrected to the level of stable hadrons is presented in the green bar, the combined scale uncertainty and hadronisation uncertainty is shown. The NLO prediction agrees with the data within the total error. In the highest bin the effects of the direct pomeron remnant are expected, discrepancy between NLO predictions and data is assumed to be due to missing pomeron remnant in the NLO prediction.
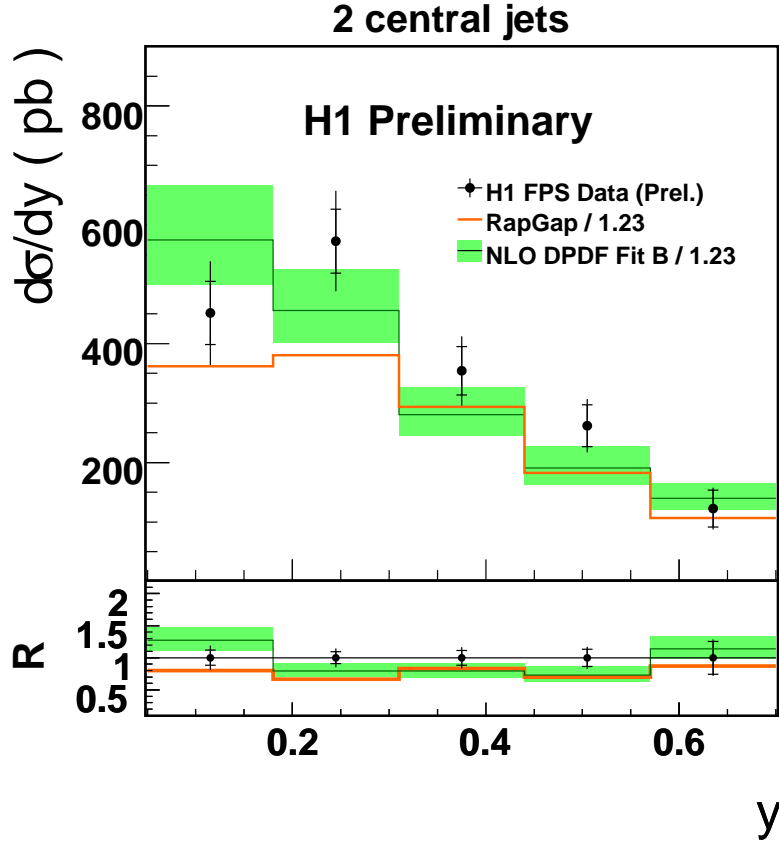
Figure A.5: Figure shows the differential cross section in y. The data are presented with the statistical error in the inner error bar and with the combined statistical and uncorrelated systematical error in the outer bar. The normalisation uncertainty is approximately 5% and it is not displayed. The comparison to Monte Carlo `RAPGAP` generator generator level cross section is presented as a red line. The NLO H1 2006 DPDF Fit B prediction corrected to the level of stable hadrons is presented in the green bar, the combined scale uncertainty and hadronisation uncertainty is shown. The NLO prediction agrees with the data within the total error. The discrepancy observed in the first bin is assumed to be due the missing pomeron remnant in NLO calculations.
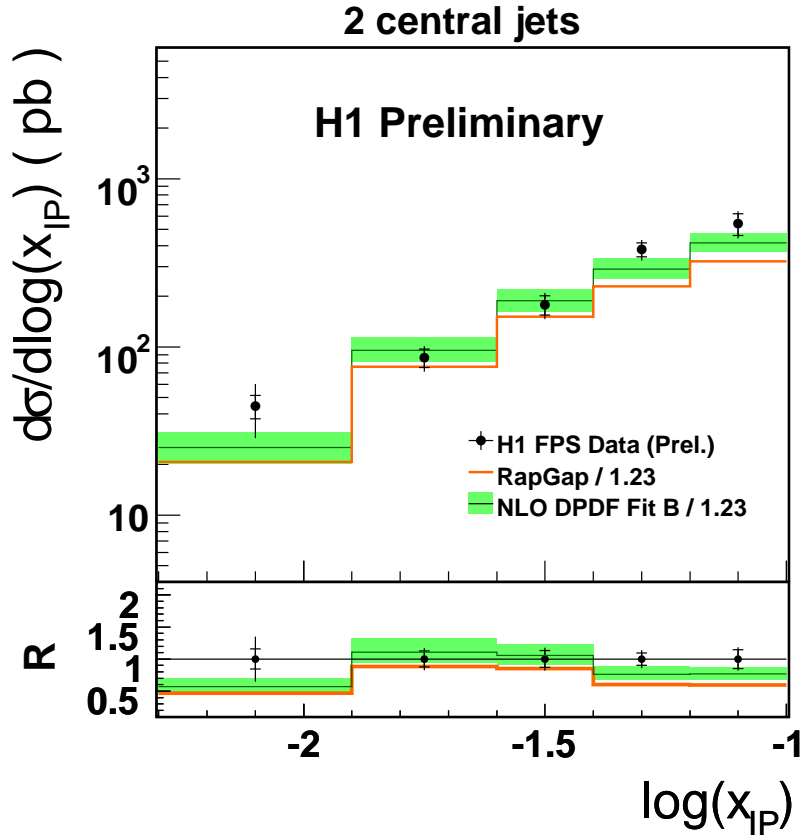
Figure A.6: Figure shows the differential cross section in $log(x_{I\!P})$. The data are presented with the statistical error in the inner error bar and with the combined statistical and uncorrelated systematical error in the outer bar. The normalisation uncertainty is approximately 5% and it is not displayed. The comparison to Monte Carlo RAPGAP generator generator level cross section is presented as a red line. The NLO H1 2006 DPDF Fit B prediction corrected to the level of stable hadrons is presented in the green bar, the combined scale uncertainty and hadronisation uncertainty is shown. The NLO prediction agrees with the data and the assumed Regge factorisation is confirmed within the total error.
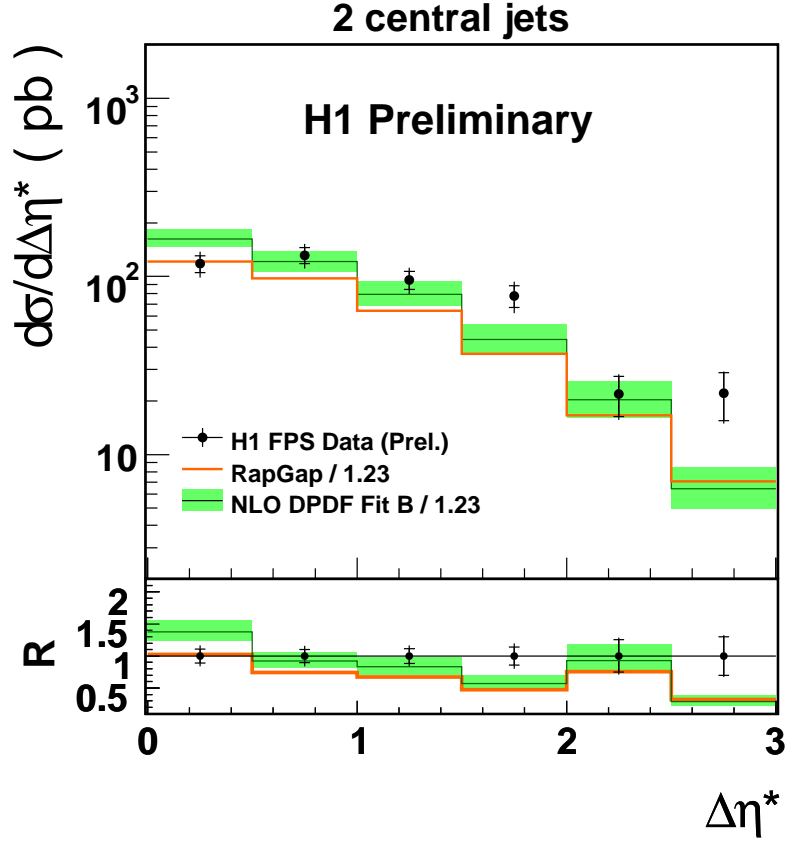
Figure A.7: Figure shows the differential cross section in the absolute value of the difference of η of the two jets in the hadronic centre-of-mass system. The data are presented with the statistical error in the inner error bar and with the combined statistical and uncorrelated systematical error in the outer bar. The normalisation uncertainty is approximately 5% and it is not displayed. The comparison to Monte Carlo `RAPGAP` generator generator level cross section is presented as a red line. The NLO H1 2006 DPDF Fit B prediction corrected to the level of stable hadrons is presented in the green bar, the combined scale uncertainty and hadronisation uncertainty is shown. The NLO prediction agrees with the data within the total error. The topology in the very last bin refers to the configuration of two jets with very large rapidity gap. The discrepancy beyond the total error may hint different parton dynamics than the DGLAP evolution equations provide.
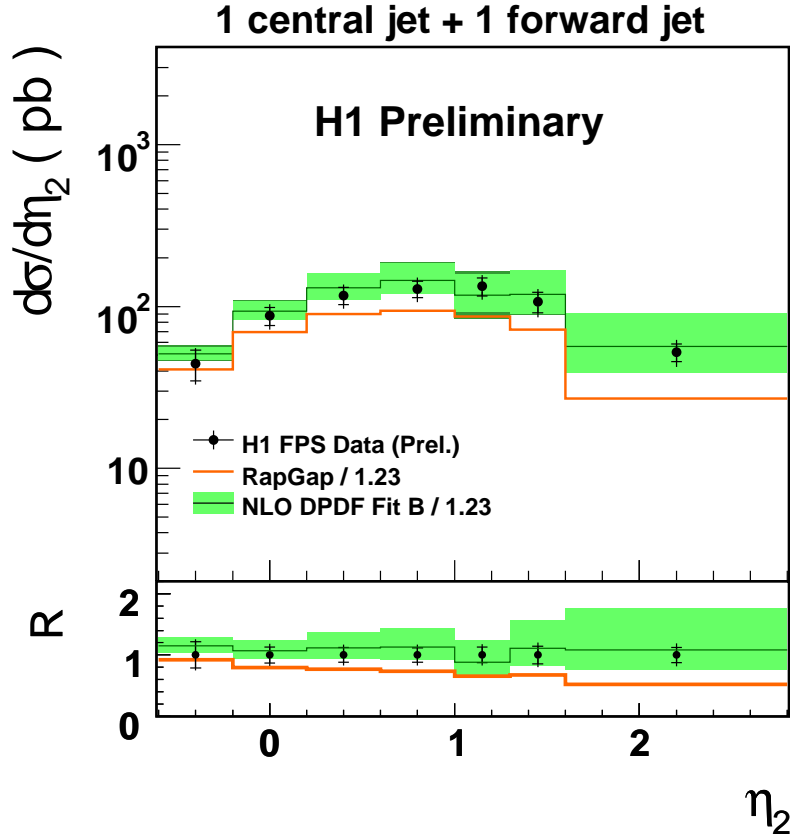
146

Figure A.8: The dijet jet topology presented in this Figure consists of selection of a central jet with pseudorapidity in the H1 laboratory frame in the range of $-1. < \eta < 2.5$ and transverse energy higher than $p_T^* > 3.5\ GeV$ and a forward jet with no pseudorapidity cut and a $p_T^* > 4.5\ GeV$. The additional cut on $\eta_2 > \eta_1$ in order to compare to the NLO predictions is applied. The Figure compares the differential cross section of the pseudorapidity of the forward jet measured in the H1 laboratory frame. The data are presented with the statistical errors (inner bar) combined with systematical errors in quadrature. The NLO predictions are presented with the scale variations error combined with hadronisation corrections uncertainty in quadrature. In the lower part of the Figure the ratio R = Theory/Data is presented. The data points are presented with combined statistical and systematical errors at 1. in order to guide the eye. The NLO predictions are presented with the combined error. The NLO predictions shows a good agreement with the measured cross sections, while the RAPGAP Monte Carlo hadron level predictions show an increasing discrepancy to the factor of 0.5.
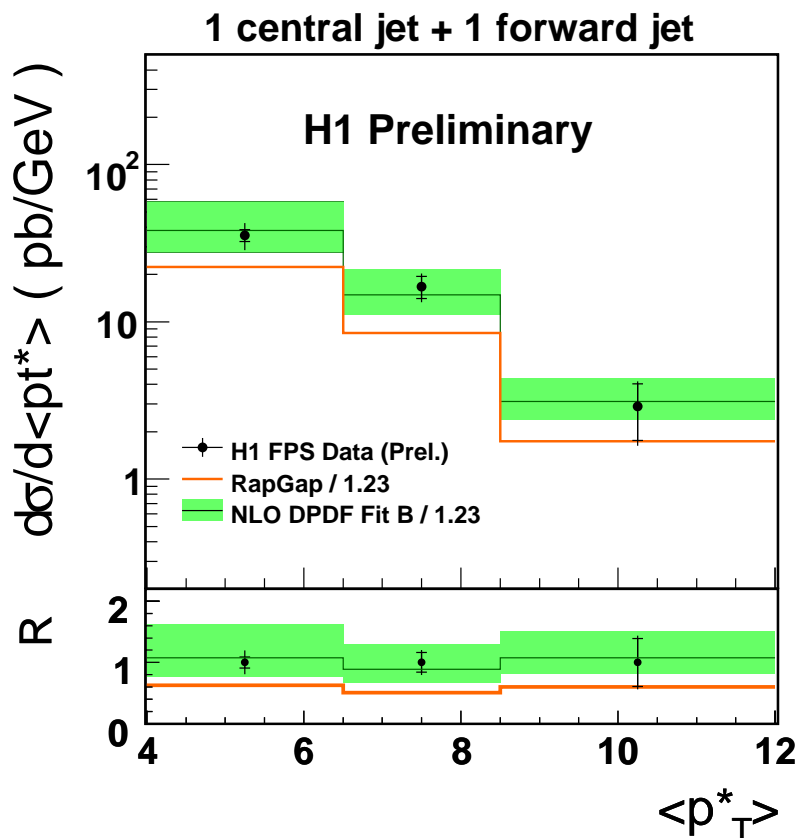
Figure A.9: Figure shows the differential cross section in mean transverse energy of the jet system in hadronic centre-of-mass system. The topology enhances the non DGLAP phase space in requirement of one central jet with $p_T^* > 3.5 \ GeV$ and $-1. < \eta_1 < 2.5$ and one forwardjet with $p_T^* > 4.5 \ GeV$ and $1. < \eta_1 < 2.8$. The additional cut on $\eta_2 > \eta_1$ in order to compare to the NLO predictions is applied. The data are presented with the statistical errors (inner bar) combined with systematical errors in quadrature. The NLO predictions are presented with the scale variations error combined with hadronisation corrections uncertainty in quadrature. In the lower part of the Figure the ratio R = Theory/Data is presented. The data points are presented with combined statistical and systematical errors at 1. in order to guide the eye. The NLO predictions are presented with the combined error. The NLO prediction describes the data very well within the errors while the RAPGAP Monte Carlo predictions show constant normalisation underestimation of 50%.

Figure A.10: Figure shows the differential cross section in $\log(\beta)$, where β is defined as $\beta = \frac{x_{bj}}{x_{I\!P}}$ and represents the length of the gluon ladder in the diffractive resolved pomeron model. The topology enhances the non DGLAP phase space in requirement of one central jet with $p_T^* > 3.5 \; GeV$ and $-1. < \eta_1 < 2.5$ and one forwardjet with $p_T^* > 4.5 \; GeV$ and $1. < \eta_1 < 2.8$. The additional cut on $\eta_2 > \eta_1$ in order to compare to the NLO predictions is applied. The data are presented with the statistical errors (inner bar) combined with systematical errors in quadrature. The NLO predictions are presented with the scale variations error combined with hadronisation corrections uncertainty in quadrature. In the lower part of the Figure the ratio R = Theory/Data is presented. The data points are presented with combined statistical and systematical errors at 1. in order to guide the eye. The NLO predictions are presented with the combined error. The NLO prediction describes the data very well within the errors while the `RAPGAP` Monte Carlo predictions show constant normalisation underestimation of 50%.
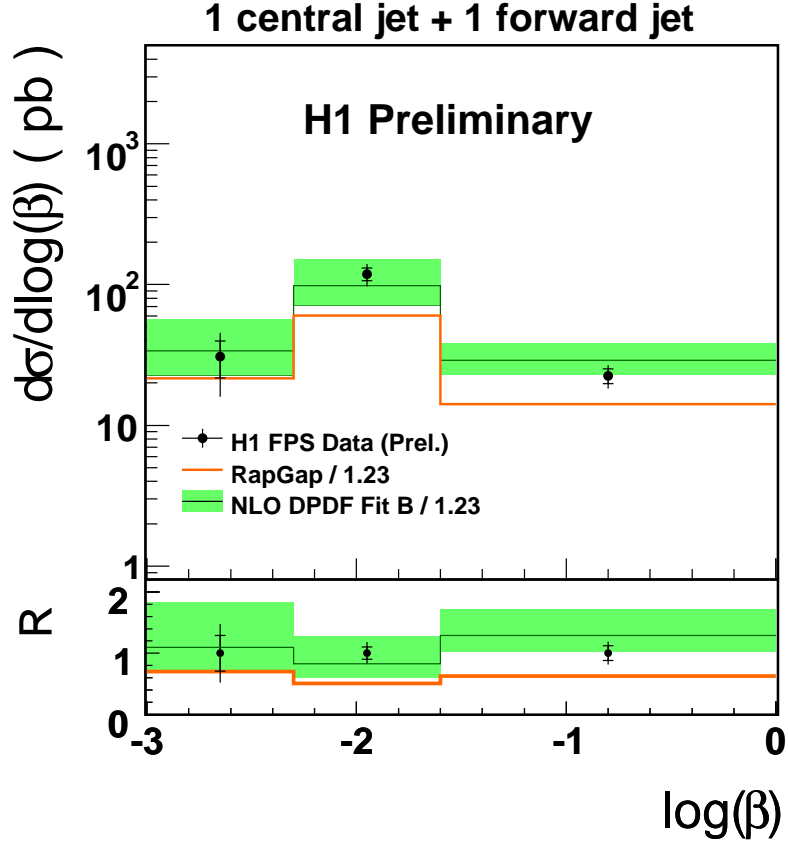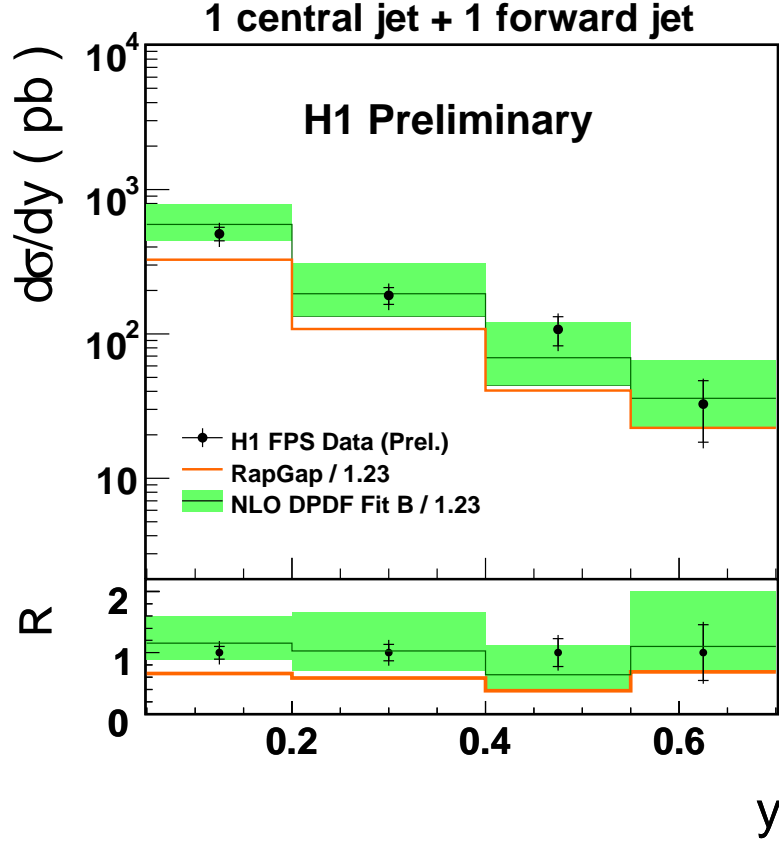
Figure A.11: Figure shows the differential cross section in y. The topology enhances the non DGLAP phase space in requirement of one central jet with $p_T^* > 3.5\ GeV$ and $-1. < \eta_1 < 2.5$ and one forwardjet with $p_T^* > 4.5\ GeV$ and $1. < \eta_1 < 2.8$. The additional cut on $\eta_2 > \eta_1$ in order to compare to the NLO predictions is applied. The data are presented with the statistical errors (inner bar) combined with systematical errors in quadrature. The NLO predictions are presented with the scale variations error combined with hadronisation corrections uncertainty in quadrature. In the lower part of the Figure the ratio R = Theory/Data is presented. The data points are presented with combined statistical and systematical errors at 1. in order to guide the eye. The NLO predictions are presented with the combined error. The NLO prediction describes the data very well within the errors while the `RAPGAP` Monte Carlo predictions show constant normalisation underestimation of 50%.
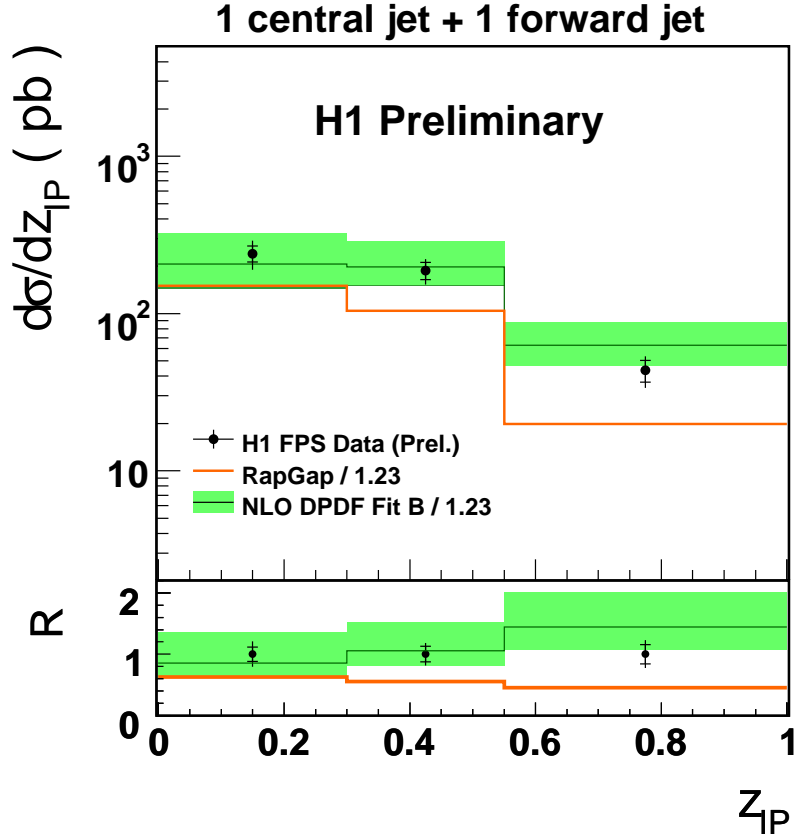
Figure A.12: Figure shows the differential cross section in the observable $z_{I\!P}$ which represents the fraction of mass contained the dijet system compare to the mass of the whole system that was produced in the interaction . The topology enhances the non DGLAP phase space in requirement of one central jet with $p_T^* > 3.5 \; GeV$ and $-1. < \eta_1 < 2.5$ and one forwardjet with $p_T^* > 4.5 \; GeV$ and $1. < \eta_1 < 2.8$. The additional cut on $\eta_2 > \eta_1$ in order to compare to the NLO predictions is applied. The data are presented with the statistical errors (inner bar) combined with systematical errors in quadrature. The NLO predictions are presented with the scale variations error combined with hadronisation corrections uncertainty in quadrature. In the lower part of the Figure the ratio R = Theory/Data is presented. The data points are presented with combined statistical and systematical errors at 1. in order to guide the eye. The NLO predictions are presented with the combined error. The NLO prediction describes the data well within the errors while the RAPGAP Monte Carlo predictions show constant normalisation underestimation of 50%.

H1 Preliminary

$d\sigma/d|\Delta\eta^*|$ (pb)

10^2

10

H1 FPS Data (Prel.)
RapGap / 1.23
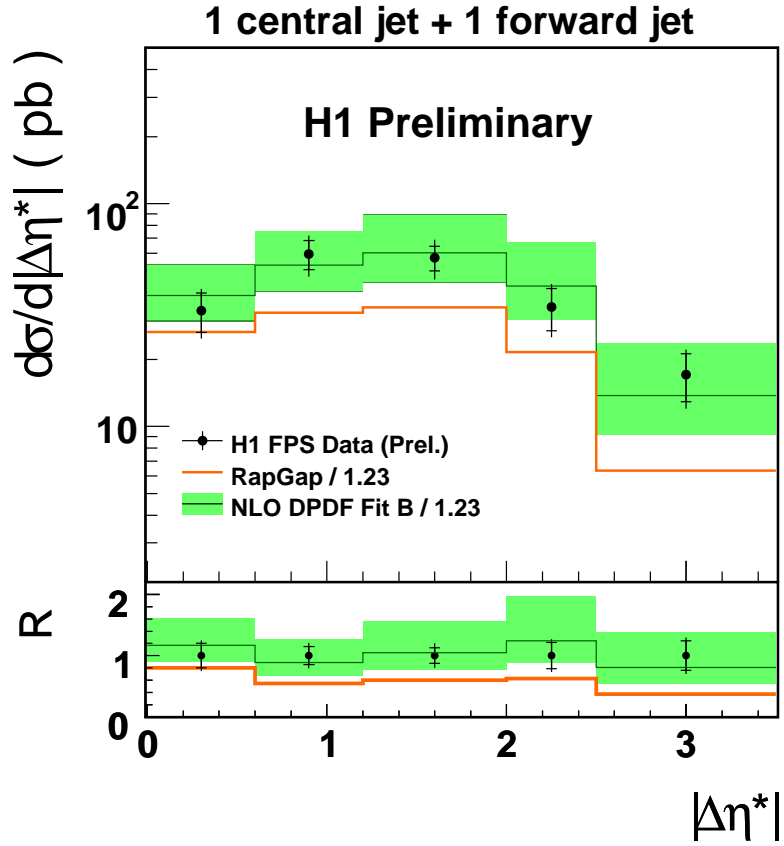NLO DPDF Fit B / 1.23

R

2

1

0

0 1 2 3

$|\Delta\eta^*|$

Figure A.13: Figure shows the differential cross section in the absolute value of the pseudorapidity difference in the HCM system of the two jets. The topology enhances the non DGLAP phase space in requirement of one central jet with $p_T^* > 3.5\ GeV$ and $-1. < \eta_1 < 2.5$ and one forwardjet with $p_T^* > 4.5\ GeV$ and $1. < \eta_1 < 2.8$. The additional cut on $\eta_2 > \eta_1$ in order to compare to the NLO predictions is applied. The data are presented with the statistical errors (inner bar) combined with systematical errors in quadrature. The NLO predictions are presented with the scale variations error combined with hadronisation corrections uncertainty in quadrature. In the lower part of the Figure the ratio R = Theory/Data is presented. The data points are presented with combined statistical and systematical errors at 1. in order to guide the eye. The NLO predictions are presented with the combined error. The NLO prediction describes the data very well within the errors while the RAPGAP Monte Carlo predictions show constant normalisation underestimation of 50% except for the first bin. This corresponds to the fact that RAPGAP Monte Carlo describes the topology of two jets with small rapidity gap in between better than topology with a big jet η separation.
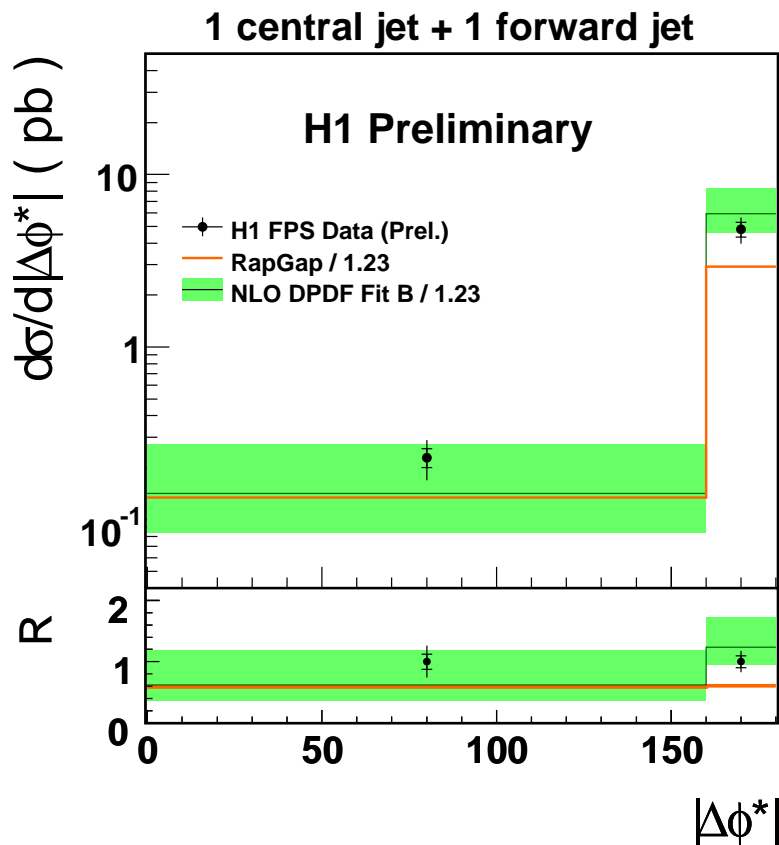
Figure A.14: Figure shows the differential cross section in the absolute value of the ϕ difference in the HCM system of the two jets. The topology enhances the non DGLAP phase space in requirement of one central jet with $p_T^* > 3.5\ GeV$ and $-1. < \eta_1 < 2.5$ and one forwardjet with $p_T^* > 4.5\ GeV$ and $1. < \eta_1 < 2.8$. The additional cut on $\eta_2 > \eta_1$ in order to compare to the NLO predictions is applied. The data are presented with the statistical errors (inner bar) combined with systematical errors in quadrature. The NLO predictions are presented with the scale variations error combined with hadronisation corrections uncertainty in quadrature. In the lower part of the Figure the ratio R = Theory/Data is presented. The data points are presented with combined statistical and systematical errors at 1. in order to guide the eye. The NLO predictions are presented with the combined error. The NLO prediction describes the data very well within the errors while the RAPGAP Monte Carlo predictions show constant normalisation underestimation of 50%. In general, the two jet production is observed to be back-to-back, the decorrelation represented by difference in the ϕ angles significantly smaller than $180°$ is suppressed by factor of 100.

Bibliography

[1] D. J. Gross, and F. Wilczek, Phys. Rev. Lett. **30** 1343-1346 (1973).

[2] H. D. Politzer, Phys. Rev. Lett. **30** 1346-1349 (1973).

[3] R. Hofstadter, Ann. Rev. Nucl. Part. Sci. **7** 231-316 (1957).

[4] M. Breidenbach *et al.*, Phys. Rev. Lett. **23** 935-939 (1969).

[5] S. Eidelman *et al.*, Phys. Lett. **B592** 1 (2004).

[6] V. N. Gribov and L. N. Lipatov, Sov. J. Nucl. Phys. **15** 438-450 (1972).

[7] Y. L. Dokshitzer, Sov. Phys. JETP **46** 641-653 (1977).

[8] G. Altarelli, and G. Parisi, Nucl. Phys. **B126** 298 (1977).

[9] E. A. Kuraev, L. N. Lipatov and V. S. Fadin, Sov. Phys. JETP **45** 199-204 (1977).

[10] I. I. Balitsky and L. N. Lipatov, Sov. J. Nucl. Phys. **28** 822-829 (1978)

[11] F.D. Aaron *et al.*, Journal of High Energy Physics **2010** 1-63 (2010).

[12] T. Regge, Nuovo Cim. **14** 951 (1959).

[13] T. Regge, Nuovo Cim. **18** 947-956 (1960).

[14] A. Donnachie and P. V. Landshoff, Phys. Lett. **B296** 227-232 (1992).

[15] P. Van Esch *et al.*, Nucl. Instrum. Meth. A 446 (2000) 409 [hep-ex/0001046].

[16] C. Adloff *et al.*, Z. Phys. C**75** (1997) 607 [hep-ex/9902019].

[17] A. Aktas *et al.*, Eur. Phys. J. C **48** (2006) 749 [hep-ex/0606003].

[18] F.D. Aaron *et al.*, Submitted to EPJC, arXiv:1010.1476 [hep-ex].

[19] A. Aktas *et al.*, Eur. Phys. J. **C48** 715-748 (2006).

[20] S. Donnachie, G. Dosch, O. Nachtmann, and P. Landshoff, Camb. Monogr. Part. Phys. Nucl. Phys. Cosmol. **19** 1-347 (2002).

[21] J. C. Collins, Phys. Rev. **D57** 3051-3056 (1998). Erratum-ibid. D **61** (2000) 019902.

[22] J. D. Bjorken and E. A. Paschos, Phys. Rev. **185** 1975-1982 (1969).

[23] R. P. Feynman, Phys. Rev. Lett.**23** 1415-1417 (1969).

[24] G. Ingelman and P. E. Schlein, Phys. Lett. **B152** 256 (1985)

[25] A. Donnachie and P. V. Landshoff, Phys. Lett. **B191** 309 (1987).

[26] J. Bartels, C. Ewerz, H. Lotter, M. Wuesthoff, M. Diehl, *Quark-Antiquark Jets in DIS Diffractive Dissociation*, hep-ph/9609239.

[27] A. Edin, G. Ingelman, J. Rathsman, Phys.Lett. **B366** 371 (1996), Z.Phys. **C75** 57 (1997)

[28] B. Andersson, G. Gustafson, G. Ingelman, T. Sjstrand, Phys. Rep. **97** 31 (1983)

[29] C. Adloff *et al.*, Z. Phys. **C76** 613-629 (1997).

[30] C. Adloff *et al.*, Eur. Phys. J. **C20** 29-49 (2001).

[31] C. Adloff *et al.*, Phys. Lett. **B520** 191-203 (2001).

[32] M. Derrick *et al.*, Z. Phys. **C68** 569-584 (1995).

[33] S. Chekanov *et al.*, Nucl. Phys. **B713** 3-80 (2005).

[34] S. Chekanov *et al.*, Nucl. Phys. **B672** 3-35 (2003).

[35] S. Chekanov *et al.*, Eur. Phys. J. **C38** 43-67 (2004).

[36] I. Abt *et al.*, Nucl. Instrum. Meth.**A386** 310-347 (1997).

[37] I. Abt *et al.*, Nucl. Instrum. Meth.**A386** 348-396 (1997).

[38] A. B. Meyer. A New Object-Oriented Physics Analysis Framework for the H1 Experiment, Published in Budapest 2001, High Energy Physics, hep2001/276

[39] T. Ahmed *et al.*, Nuclear Physics B **429** 477 (1994).

[40] A. Levy, Low-x physics at HERA, Tel Aviv University, Israel.

[41] G. F. Chew, S. C. Frautschi, Phys. Rev. Lett. **8** (1962)41.

[42] A. Donnachie, P. V. Landshoff, Phys. Lett. **B 296** (1992)227.

[43] G. Ingelman, P. Schlein, Phys. Lett. **B 152** 256(1985).

[44] H. Jung, Future Diffraction at HERA, Proc. of the LISHEP workshop on diff. physics, Rio de Janeiro, Brasil, Feb 16 - 20, 1998.

[45] J. Owens, Phys. Rev. D **30** (1984) 943.

[46] A. Buras and K. Gaemers, Nucl. Phys. B **132** (1978) 249.

[47] A. Aktas *et al.*, JHEP **0710** (2007) 042 [arXiv:0708.3217 [hep-ex]].

[48] H. Oberlack, H. Wellish, J. Kubenka and P. Schlacht, Hadronic Calibration of the H1 LAr Calorimeter using Software Weighting Techniques, H1 internal note, H1-0294-346.

[49] B. Andrieu *et al.*, The H1 liquid argon calorimeter system, Nucl. Instrum. Meth., A **336** 460-498 (1993)

[50] H. Jung, Comp. Phys. Comm. **86** 147 (1995).

[51] T. Sjostrand, Comp. Phys. Comm. **82** 74 (1994).

[52] L. Lonnblad, Comp. Phys. Comm. **71** 15 (1992).

[53] B. Kniehl, H. Kohrs, and G. Kramer, Z. Phys. C **65** 657 (1995).

[54] J. Pumplin *et al.*, JHEP **07** 012 (2002).

[55] G. A. Schuler and T. Sjostrand, Z. Phys. **C68** (1995) 607.

[56] R. Brun, R. Hagelberg, M. Hansroul and J. C. Lassalle, CERN-DD-78-2-REV.

[57] G. Ingelman, A. Edin and J. Rathsman, DESY-96-057, 1996, hep-ph/9605286 (unpublished).

[58] A. Kwiatkowski, H.-J. Moehring, and H. Spiesberger, Comput. Phys. Commun **69** (1992) 155; and `HERACLES` 4.5.2 unpublished

[59] J. Rathsman., A Generalised Area Law for Hadronic String Reinteractions, Phys. Lett., B **452** 364-371 (1999)

[60] Z. Nagy, Z. Trocsanyi, Phys. Rev. Lett. **87** (2001) 082001.

156

[61] S. Catani and M. H. Seymour, Nucl. Phys. B**485**, 291 (1997) [Erratum-ibid. B **510**, 503 (1998)] [arXiv:hep-ph/9605323].

[62] R. Brun, R. Hagelberg, M. Hansroul and J. C. Lassalle, CERN-DD-78-2-REV.

[63] S. Osman, D. Salek, The Low Pt HFS and Jet Energy Calibration, H1-IN-631(02/2009).

[64] S. D. Ellis, and D. E. Soper, Phys. Rev. D**48** 3160-3166 (1993).

[65] M. Cacciari, G.P. Salam and G. Soyez, Phys. Lett. B **641** (2006) [hep-ph/0512210].